FINAL PERFORMANCE REPORT

Contract Title: **Multi-Channel and Multi-Dimensional Sensors Parametric Statistics Estimation**

Contract Number: FA9550-08-1-0412
Period of Performance: 1 July 2008 to 30 November 2010

Principal Investigator: S. Lawrence Marple Jr,
School of Electrical Engineering and Computer Science
Oregon State University
Corvallis, OR 97331

Objectives of Research

Parametric estimation, when expressed in the form of autoregressive models or linear prediction analysis or lattice filters or minimum variance distortion-less response adaptive filters, has been a major foundation for enhanced signal processing performance. Examples include high resolution spectral analysis, linear prediction coding for bit rate reduction, and enhanced detection statistic performance for space-time adaptive processing (STAP) using parametric forms of the inverse covariance matrix. The mathematical matrix structures of most parametric estimators cited above are typically exploitable, leading to fast computational algorithms that reduce the computational burden by typically one to two orders of magnitude, making the parametric algorithms computationally competitive with more traditional non-parametric spectrum and filter applications. Parametric algorithms developed to date are one-dimensional (1-D), one-dimensional multi-channel (1-D MC) [one dimension is usually time], and two-dimensional (2-D). Currently published two-dimensional fast algorithms are only efficient along one dimension because the other dimension is usually assumed to be fixed (a legacy of the development of published 2-D fast algorithms that are based on adaptations of the 1-D MC fast algorithm matrix structures). The objective of this research was to further exploit structure that exists to lead to even faster 2-D parametric estimation computational algorithms.

Four graduate students were supported to varying degrees by this AFOSR contract to investigate along four particular algorithm lines of parametric statistical estimation. A summary of this research is provided in the next section, and unpublished results are attached as appendices.

Executive Summary of Research

The first line of investigatory research sponsored by this contract was a study of the minimum variance (MV) spectral estimator, a robust high-resolution frequency domain analysis tool for short data records. The traditional formulation of the minimum variance spectral

Report Documentation Page

Form Approved
OMB No. 0704-0188

1. REPORT DATE	2. REPORT TYPE	3. DATES COVERED
02 JUL 2009		

4. TITLE AND SUBTITLE	5a. CONTRACT NUMBER
Multi-Channel and Multi-Dimensional Sensors Parametric Statistics Estimation	5b. GRANT NUMBER
	5c. PROGRAM ELEMENT NUMBER
6. AUTHOR(S)	5d. PROJECT NUMBER
Lawrence Marple	5e. TASK NUMBER
	5f. WORK UNIT NUMBER
7. PERFORMING ORGANIZATION NAME(S) AND ADDRESS(ES)	8. PERFORMING ORGANIZATION REPORT NUMBER
Oregon State University,Corvallis,OR,97331-8507	
9. SPONSORING/MONITORING AGENCY NAME(S) AND ADDRESS(ES)	10. SPONSOR/MONITOR'S ACRONYM(S)
	11. SPONSOR/MONITOR'S REPORT NUMBER(S)

12. DISTRIBUTION/AVAILABILITY STATEMENT

Approved for public release; distribution unlimited.

13. SUPPLEMENTARY NOTES

14. ABSTRACT

Parametric estimation, when expressed in the form of AR models, linear prediction analysis, lattice filters or minimum variance adaptive filters, has been a major foundation for enhanced signal processing performance. Examples include high resolution spectral analysis, linear prediction coding for bit rate reduction, and enhanced detection statistic performance for space-time adaptive processing (STAP) using parametric forms of the inverse covariance matrix. The mathematical matrix structures of most parametric estimators are typically exploitable, leading to fast computational algorithms that reduce the computational burden by typically one to two orders of magnitude, making the parametric algorithms competitive with more traditional non-parametric spectrum and filter applications. Parametric algorithms developed to date are 1-D single channel, 1-D multi-channel [one dimension is usually time], and 2-D. Currently published 2-D fast algorithms are only efficient along one dimension because the other dimension is assumed fixed. This project will use further exploitable structure to lead to even faster 1-D and 2-D parametric estimation computations.

15. SUBJECT TERMS

16. SECURITY CLASSIFICATION OF:			17. LIMITATION OF ABSTRACT	18. NUMBER OF PAGES	19a. NAME OF RESPONSIBLE PERSON
a. REPORT	b. ABSTRACT	c. THIS PAGE			
unclassified	**unclassified**	**unclassified**		**172**	

estimation (MVSE) depends on the inverse of a Toeplitz autocorrelation matrix, for which a fast computational algorithm exists that exploits this structure. This research investigation extended the MVSE approach to two data-only formulations linked to the covariance and modified covariance cases of least-squares linear prediction (LP), which require inversion of near-to-Toeplitz data product matrices. The results of the research proved that the near-to-Toeplitz matrix inverses in the two new fast algorithms have special representations as sums of products of triangular Toeplitz matrices composed of the LP parameters of the least-squares-based formulations. From these, it was shown how to develop fast solutions of two least-squares-based minimum variance spectral estimators (LS-based MVSEs). These new MVSEs provide additional resolution improvement over the traditional autocorrelation-based MVSE.

The research results were published by Lin Wei (for her PhD theses) and S. Lawrence Marple Jr. in the journal *Signal Processing* under the title "Fast Algorithms for Least Squares Based Minimum Variance Spectral Estimator" (vol. 88, pp. 2181-2192, September 2008).

The second line of investigatory research sponsored by this contract was three-dimensional (3-D) study in which the three dimensions are time (delay), frequency (Doppler shift), and cycle frequency (cyclostationary signal process). Separating and locating each digital communication signal in a dense signal environment are often impossible using traditional two-parameter frequency-difference-of-arrival and time-difference-of-arrival (FDOA/TDOA) joint estimation 2-D tools. By adding a third parameter for the joint estimation, we have shown as part of our research how to achieve separation and localization not possible with just a 2-D scheme. We introduce the novelty of a new 3-D signal processing tool, the *alpha cross ambiguity function*, to exploit the joint three-parameter estimation problem. Specifically, we consider the problem of jointly estimating TDOA, FDOA, and the cyclic frequency *alpha* for spectrally, temporally and spatially interfering signals arriving at two spatially separated receivers. Even when they work, conventional methods for estimating TDOA and/or FDOA produce biased estimates when multiple emitters are located spatially close to each other and share the same regions of the spectrum at the same time. In this research, a new three-dimensional joint estimation method for TDOA, FDOA, and cyclic frequency parameters, called the alpha cross ambiguity function has been proposed, and an analysis to exploit the signal modulations with cyclostationary properties has been demonstrated. The *alpha*-CAF parameter estimation algorithm, as we term it, is introduced along with an analysis of its performance compared to conventional one-dimensional and two-dimensional estimators. The results are captured in Appendix **A**, abstracted from David Ohm's PhD thesis with advisor S. Lawrence Marple, Jr.

The third line of investigatory research sponsored by this contract was a study to show how the two-dimensional parametric algorithms can be applied to sharpen the details of buried mines detected by ground penetration radar. The two dimensions considered were localized time and localized frequency. Time–frequency analysis techniques are used for buried plastic landmine detection with a forward-looking ground penetration radar (GPR) system. Several

time–frequency distributions are considered to characterize and interpret the scattering phenomena of both targets and clutter. An ambiguity function based detector is also presented, which employs principal component analysis and feature selection for data dimensionality reduction and linear discrimination analysis for signal classification. Experimental results based on the SRI (Stanford Research Institute)-provided experimentally measured forward-looking GPR data were processing, and shown to provide a significant detection performance improvement over the conventional detection schemes. The results were presented by Master's degree candidate Matthew Fleming, advisor S. Lawrence Marple, Jr., and published at the August 2009 NATO Advanced Study Institute (AS) on Unexploded Ordnance Detection and Mitigation at Il Ciocco, Italy. Appendix **B** contains the poster from this workshop.

The fourth line of investigatory research sponsored by this contract was a study to develop computational superfast MVSE 1-D and 2-D algorithms, in pick up another order of magnitude reduction in computations. The minimum variance spectral estimator (sometimes referenced as the Capon spectral estimator, or the minimum variance distortion-less response estimator) is a high resolution spectral estimator used extensively in practice as an alternative to the classical squared-magnitude Fourier estimator. In its original form without special algorithms, it requires order p^3 computations, in which p is the minimum variance filter size. The current implementation used in practice employs a fast algorithm developed by Musicus, requiring order p^2 computations. This research has provided discoveries of additional exploitable structure to bring the computational order down to $p \log_2 p$, creating a superfast algorithm.

The standard expression for the one-dimensional minimum variance spectral estimator (1-D MVSE) is

$$(1) \qquad P_{MV}(f) = \frac{T}{\boldsymbol{e}^H(f)\boldsymbol{R}^{-1}\boldsymbol{e}(f)}$$

in which T is the sampling interval, $\boldsymbol{e}(f) = [1 \exp(j2\pi fT) \cdots \exp(j2\pi fpT)]^T$ is the frequency vector, and $\boldsymbol{R}$ is the $(p+1)\times(p+1)$ correlation matrix, often formed using estimated correlations produced from a limited data sample record. This takes order p^3 computations to evaluate. Because the inverse correlation matrix can be expressed in terms of the sum of products of triangular Toeplitz matrices formed from the autoregressive (AR) parameters $a_p[k]$ [1], Musicus [*IEEE Trans. Sig. Proc.*, October 1985] discovered a mathematically equivalent restructuring of the MVSE as

$$(2) \qquad P_{MV}(f) = \frac{T}{\sum_{k=-p}^{p} \Psi_{MV}[k] \exp(-j2\pi fkT)}$$

in which the $\Psi_{MV}[k]$ coefficients are calculated as a linearly weighted correlation of AR parameters

$$(3) \qquad \Psi_{MV}[k] = \frac{1}{\rho_p} \sum_{i=0}^{p-k} \left(p+1-k-2i \right) a_p[k+i] a_p^*[k]$$

for $-p \le k \le p$. Algorithms exist (for example, Yule-Walker and Burg algorithms) that generate estimates of AR parameters from data records, most requiring order p^2 computations, which is also that required to compute the coefficients of Eq. (3). An FFT is then used to compute the denominator of Eq. (2). We have discovered additional structure that can further reduce the computations by instead evaluating the MVSE as

$$(4) \qquad P_{MV}(f) = \frac{T}{(p+1)A(f)A^*(f) - B(f)A^*(f) - A(f)B^*(f)}$$

in which FFTs are used to evaluate the following transforms that use the AR parameters

$$(5) \qquad A(f) = T \sum_{n=0}^{p} a_p[n] \exp(-j2\pi fnT)$$

$$(6) \qquad B(f) = T \sum_{n=0}^{p} n a_p[n] \exp(-j2\pi fnT)$$

By eliminating the correlation of the AR parameters used in Eq. (3), the computational count is reduced further to $p \log_2 p$. Note that one transform is the derivative of the other,

$$(7) \; B(f) = \frac{j}{2\pi T} \frac{\partial A(f)}{\partial f}$$

providing another possible interpretation of the 1-D MVSE denominator function and another possibility for computational reduction. The 2-D MVSE has also been evaluated for similar reductions in computations.

The results of this research, by PhD candidate Majid Adeli and advisor S. Lawrence Marple, Jr., may be found in the conference proceedings for the 44th Asilomar Conference on Signals, Systems, and Computers, November 2010, in a paper entitled “Super-Fast Algorithm for Minimum Variance (Capon) Spectral Estimation”.

APPENDIX A

KINEMATIC AND CYCLOSTATIONARY PARAMETER ESTIMATION FOR CO-CHANNEL EMITTER LOCATION APPLICATIONS

PhD Candidate: David Ohm
Advisor: S. Lawrence Marple, Jr.

School of Electrical Engineering and Computer Science
Oregon State University
Corvallis, OR

Research Report

AFOSR Award FA9550-08-1-0412

June 2009

TABLE OF CONTENTS

TABLE OF CONTENTS (Continued)

LIST OF FIGURES

LIST OF FIGURES (Continued)

LIST OF FIGURES (Continued)

LIST OF FIGURES (Continued)

LIST OF FIGURES (Continued)

LIST OF FIGURES (Continued)

LIST OF FIGURES (Continued)

LIST OF TABLES

LIST OF APPENDIX FIGURES

Chapter 1 – INTRODUCTION

1.1 Background and Motivation

The problem of locating a signal source, or an emitter, has many civilian and military applications, such as communication regulations enforcement, military reconnaissance, and search-and-rescue operations. Many of the most widely used emitter location methods rely on the accurate and robust estimation of the differential time-delay, or *time-difference-of-arrival* (TDOA), between signal replicas arriving at two spatially separated receivers. Often, at least one of the receivers is located on a moving platform such as an airplane, resulting in relative motion between the emitter and one or more of the receivers. This relative motion results in a differential Doppler shift, or *frequency-difference-of-arrival* (FDOA), that can be measured and exploited along with TDOA measurements to locate an emitter.

Many of the conventional methods for estimating TDOA are based on coherence and time-delay estimation techniques that were developed within the sonar and radar research communities [1]. One of the most popular TDOA estimation algorithms is called the *generalized cross correlation* (GCC) method. The GCC method has many variations and can be a robust TDOA estimation technique in many applications. However, it performs poorly against multiple signals that overlap within the same frequency band, and it is unable to produce separate unbiased estimates when multiple emitters are located spatially close to each other, resulting in unresolvable TDOA estimates. [1, 9, 10].

A popular conventional method for *jointly* estimating both TDOA and FDOA, called *cross ambiguity function* (CAF) processing, was introduced in the 1980's [4], and has

been widely used for emitter location and radar processing applications [5]. Although the CAF method can jointly estimate both TDOA and FDOA, later in this thesis it is demonstrated that it performs poorly against spectrally overlapping signals, and it is unable to produce separate unbiased TDOA and FDOA estimates when multiple emitters are located spatially close (often less than a 1–2 kilometers) to each other. In many cases the spatial proximity at which the GCC and CAF methods fail is still too large to ignore for emitter location applications. The limitations of the GCC and CAF methods motivate the need for new jointly estimated TDOA and FDOA estimation algorithms that can produce unbiased kinematic parameter estimates from spectrally overlapping signals regardless of their source location.

Traditionally, when spatially close emitters overlap spectrally and temporally, accurate TDOA and FDOA estimation is difficult, and precise emitter location is often not possible. However, by exploiting a signal parameter of bauded signals called cyclic frequency a *signal-of-interest* (SOI) can be separated from a *signal(s)-not-of-interest* (SNOI) that is within the receiver's field of view. This can be critical, for example, in a search-and-rescue application where the timely location of a lost individual depends on the capability of an algorithm to separate the individual's radio signal from other received signals using the same region of the *radio frequency* (RF) spectrum. This problem is made even more difficult when the actual locations of the SNOI emitters are unknown and approximately in the same area as the SOI emitter. Figure 1.1 illustrates the scenario of a lost hiker using a radio or handset to call for help while another emitter sharing the same frequency-band is located within a range of 1–2 kilometers. At this range conventional methods may fail to produce accurate TDOA and FDOA estimates from the hiker's signal due to the interfering emitter. As depicted in the figure, in this thesis a new *alpha cross ambiguity function* called alpha*CAF* is introduced that will produce accurate TDOA and FDOA estimates for a bauded SOI regardless of the

interfering emitter's location.

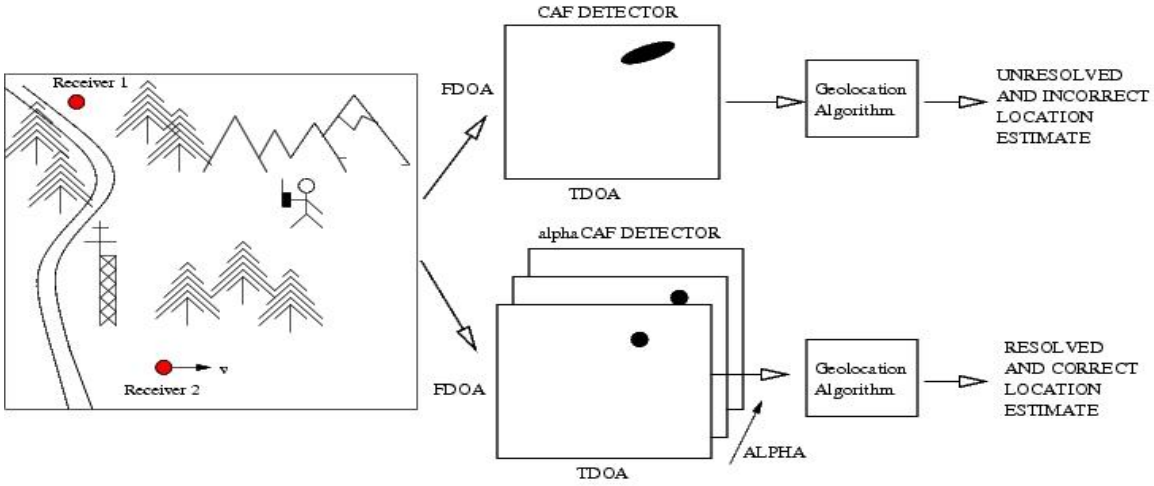

Figure 1.1: Illustration of a lost hiker using a radio within 1–2 kilometers of a co-channel emitter. Using conventional methods the TDOA and FDOA parameters needed for geolocation of the hiker's radio emitter cannot be determined. However, the new *alpha*CAF method introduced in this thesis can be used to distinguish (separate) the emitters and to determine usable geolocation solutions.

When a SNOI occupies the same spectral band as the SOI, it is referred to as *co-channel interference* (CCI). CCI presents a significant challenge and can severely limit the capability of conventional methods to correctly estimate TDOA and FDOA for the SOI. When both a SOI and a SNOI are present, methods for mitigating the SNOI interference must be used in order to achieve reliable estimation results. If the SOI exhibits a property called *cyclostationarity*, then it is possible to separate that signal from the interfering signal by using cyclostationary processing techniques.

Cyclostationarity is exhibited by man-made signals that employ periodic generation methods such as modulation, channel coding, etc. [13]. There have been several techniques introduced in the literature for exploiting cyclostationarity in order to estimate TDOA only [9, 12]. However, all of these methods assume that the received signals are

not Doppler shifted, or that the Doppler shift is a known quantity that can be compensated. As mentioned earlier, the conventional CAF method can jointly estimate both TDOA and FDOA [4, 6, 8]. However, the CAF method fails to provide separate unbiased estimates when CCI is present and the SOI and SNOI emitters are spatially close. For this reason, a the new joint estimation method, called the *alpha*CAF method, is introduced in this thesis. The *alpha*CAF method exploits cyclostationarity to overcome the limitations of the conventional estimators. In general, through the exploitation of a parameter called *cyclic frequency* (represented by the symbol α) it is demonstrated in this thesis that it is possible to produce unbiased joint TDOA and FDOA estimates for emitter location applications even when CCI causes conventional methods to fail. Not only can *alpha*CAF be used as a new joint TDOA and FDOA estimator, similar to the conventional CAF, it is actually a three-dimensional cross correlation function of the three parameters: delay, Doppler shift, and cyclic frequency. However, in most practical applications one parameter will be fixed and the other two jointly estimated. For emitter location applications the kinematic-dependent parameters are of most interest, so cyclic frequency can be fixed and TDOA and FDOA jointly estimated.

Once TDOA and FDOA estimates are produced for a specific SOI, they can be used to estimate the emitter's position using a *geolocation* algorithm. It is not the goal of this thesis to introduce any new geolocation algorithms. However, a common geolocation method will be discussed in order to highlight how TDOA and FDOA measurements are used in emitter location applications for the ultimate goal of producing emitter location estimates on the earth's surface.

1.2 Thesis Organization

Chapter 2 presents a review of the most common conventional methods for TDOA and FDOA estimation used in emitter location applications. Section 2.1 introduces several common signal models used for developing TDOA and FDOA estimation algorithms. The signal models are introduced together with a discussion about their underlying assumptions and limitations. After the discussion on signal models, Section 2.2 introduces the GCC method of time delay estimation. The GCC method was developed for sonar signal processing applications several decades ago and has been proved to be a robust and powerful tool for estimating TDOA [2, 3]. However, with the increasing use of the radio spectrum for modern communications, the GCC method is not always reliable when used in complex signal environments. In section 2.2.1 Several variations of the GCC method are discussed, and GCC processing results are presented using simulated data.

Following the discussion about the GCC method, Section 2.3 introduces the CAF method for jointly estimating TDOA and FDOA. In addition to the necessary mathematical background, practical issues for using the CAF method are introduced along with simulated application examples. The CAF method has great utility in making the TDOA and FDOA measurements needed in common geolocation algorithms. However, it will be shown that it fails to produce reliable measurements in a CCI environment when multiple emitters are located spatially close together. Although several computationally efficient methods for computing the CAF have been introduced in the literature [4, 6, 8], CAF processing can still require large computational resources, making it unattractive for some applications. This fact is discussed and used to motivate the method introduced in Section 2.4.

Section 2.4 introduces the *hybrid* TDOA and FDOA estimation method, which uses

the GCC concept, together with coherence processing techniques, to arrive at an algorithm for iteratively generating both TDOA and FDOA measurements. This is done without the computational burden associated with computing the CAF.

The overview and background of the conventional methods presented in Chapter 2 demonstrates the limitations of these methods for estimating TDOA and FDOA in a modern signal environment. Chapter 3 introduces cyclostationary processing, along with its use for separating a SOI from interference by exploiting periodic phenomena found in many man-made signals. Several features of cyclostationary processing are explained and demonstrated. In section 3.3, methods for using cyclostationary processing techniques to estimate TDOA are introduced and demonstrated.

Chapter 4 introduces the new *alpha*CAF algorithm for jointly estimating TDOA, FDOA and cyclic frequency. The algorithm is derived using multiple approaches, including a heuristic approach and a *maximum likelihood* (ML) approach, and demonstrated using simulated signals. The advantages of the new *alpha*CAF method over the conventional methods are illustrated by means of simulated examples.

Chapter 5 introduces two simulated test environments used to test the performance of the algorithms presented in this thesis. Section 5.2 presents a qualitative assessment demonstrating the *alpha*CAF method's capability to produce separate unbiased TDOA and FDOA estimates when the conventional CAF cannot. Section 5.3 continues this analysis with a quantitative assessment of *alpha*CAF method's capability to produce separate unbiased TDOA and FDOA estimates.

Chapter 6 presents a detailed assessment of the parametric tradeoffs when using the *alpha*CAF method. The capability of the *alpha*CAF method to resolve individual signal parameters is demonstrated, along with the probabilistic performance of the algorithm as an estimator and detector. Use of the algorithm with multiple mixed-modulation types is also illustrated.

Chapter 7 demonstrates how TDOA and FDOA measurements are used for geolocation. In Section 7.1 a historical review of emitter location methods is introduced. Section 7.2 gives an introduction to a conventional geolocation method by providing the details of the Newton-Raphson algorithm. The importance of the *error ellipse* is also discussed. A geolocation example is given to demonstrate the advantages of the *alpha*CAF method over the conventional CAF method for precision geolocation applications.

Chapter 8 concludes this dissertation with a review of the performance results achieved by the new algorithm compared to the conventional methods. Section 8.2 discusses suggested areas for further research.

1.3 Summary of Contributions

The research presented in this thesis introduces a new three-dimensional correlation function, called the *alpha cross ambiguity function*, or *alpha*CAF. The *alpha*CAF is capable of *jointly* estimating TDOA, FDOA and cyclic frequency (α) parameters from signal replicas arriving at two spatially separated receivers. TDOA and FDOA are the kinematic parameters needed to locate an emitter using common geolocation techniques. Multiple signal interference and spatial proximity between emitters can cause conventional methods, such as the CAF method, to produce unresolvable biased estimates. In contrast the *alpha*CAF method can separate signals according to their unique baud rates and produce resolved TDOA and FDOA estimates. Although several conventional one-dimensional and two-dimensional cross correlation functions have been previously developed to separate signals based on their kinematic parameters [1, 4, 9], all of these conventional methods fail when multiple signals overlap temporally and spectrally, and the signal emitters are located spatially close. For example, the CAF method can jointly estimate TDOA and FDOA. However, for a random signal the CAF resolution spacing

will have a nominal width in the TDOA dimension that is proportional to $1/B_s$, where B_s is the nominal width of the received signal power spectrum [4]. Likewise, the peak width in the FDOA dimension will be proportional to $1/(NT_s)$, which is the data record length. If two co-channel emitters are located such that their true TDOA and FDOA parameters do not map to well separated resolution cells then the CAF method may produce biased TDOA and FDOA estimates. These biased kinematic parameter estimates will in turn prevent the geolocation algorithm from producing precise emitter location estimates.

The *alpha*CAF method is the first practical three-dimensional cross correlation function for estimating TDOA, FDOA and cyclic frequency. Even though the *alpha*CAF method is a three-dimensional estimator, throughout this thesis it is viewed in a two-dimensional sub-version for purposes of illustrating performance and for solving a specific emitter location problem. In many practical applications the cyclic frequency for a SOI may be known. In that case, it can be fixed within the *alpha*CAF computations, resulting in a two-dimensional estimator for TDOA and FDOA. Likewise, if one of the kinematic parameters is known, the *alpha*CAF can be used to jointly estimate the other along with cyclic frequency. In cases where nothing is known, it can jointly estimate both kinematic parameters and cyclic frequency. This makes the *alpha*CAF a powerful tool for emitter location applications such as search-and-rescue, where there may be very little information about a SOI that exists within an interference signal environment.

In this thesis, six research subtopics are addressed for the development of the *alpha*CAF method: 1) Signal models are developed for use in algorithm development. 2) Conventional TDOA and FDOA parameter estimation techniques are introduced, along with simulated examples related to real applications. 3) Modern signals are simulated using realistic collection geometries for processing with the algorithms presented. 4) The use of cyclostationary processing techniques for separating CCI signal parameters

are presented 5) A qualitative and quantitative analysis of both the conventional CAF and the new *alpha*CAF parameter estimators is given 6) A geolocation algorithm is introduced to demonstrate how TDOA and FDOA parameters are used in practice, and to demonstrate how the *alpha*CAF enables precise geolocation results. These subtopics bring together the topics of kinematic parameter estimation and emitter location in a manner not found in existing literature.

In this thesis the new *alpha*CAF algorithm for jointly estimating TDOA, FDOA and cyclic frequency is derived heuristically and using *maximum likelihood* techniques. Throughout the thesis, results from experiments are presented that strongly support the claim that the *alpha*CAF method generates unbiased estimates when CCI causes conventional methods to generate biased ones. In addition to the introduction of a new three-dimensional joint estimation algorithm, detailed experimental testing results are presented to support all claims made about both the conventional CAF method and the new *alpha*CAF method. The experiments include testing the algorithms in both narrow-band and wide-band interference environments, and against multiple signal modulation types. Since an analytic approach to proving that the *alpha*CAF is an unbiased estimator has so far proved to be mathematically intractable, Monte Carlo testing has been performed in order to get a statistical measure of how the conventional CAF and *alpha*CAF methods compare to the published *Cramer Rao lower bound* (CRLB) in [4]. In addition, the *alpha*CAF method has been tested to determine its ability to separate signals with only slightly different symbol rates. The combination of resolution, modulation, symbol rate, and statistical testing presented in this thesis provides a perspective into cyclostationary processing that cannot be found in previously published literature. These efforts along with the robust solution to a real emitter location problem provided by the *alpha*CAF method constitute a serious contribution to the field of emitter location.

Chapter 2 – CONVENTIONAL TDOA AND FDOA ESTIMATION METHODS

2.1 Signal Models

In order to properly setup the problem of estimating TDOA and FDOA for a SOI, it is necessary to form a mathematical signal model that will adequately represent the signal collection and will lead to tractable solutions. There have been several models already presented in the literature [2, 4]. The most basic model is used to describe a SOI collected in an *additive white Gaussian noise* (AWGN) environment by two spatially separated receivers with no relative motion between them and the emitter. This model is expressed as

$$x(t) = s(t) + n_x(t) \tag{2.1}$$

$$y(t) = s(t - D) + n_y(t) \tag{2.2}$$

where $s(t)$ represents the SOI and $n_x(t)$ and $n_y(t)$ are zero-mean Gaussian noise terms. In this model, the parameter of interest is D — i.e., the TDOA. Although this model is mathematically simple, it is not always useful in real-world applications. For instance, it does not take into account any amplitude or phase mismatch at the receivers, and it assumes complete coherence between receivers. Also, the model does not allow for any relative motion between the receivers and the emitter, discounting any Doppler shift or time-varying Doppler shift that will result.

A narrow-band model that does take into account amplitude and phase mismatches

and Doppler shift due to relative motion is expressed as

$$x(t) = s(t) + n_x(t) \tag{2.3}$$

$$y(t) = A_r s(t - D)\exp(j2\pi f_d t) + n_y(t) \tag{2.4}$$

where A_r is a complex constant that represents the amplitude and phase mismatch of received signal y relative to received signal x. The added exponential term in (2.4) represents the differential Doppler shift due to relative motion between the receivers and the emitter. Again, D is the TDOA parameter of interest. This model has been widely used in the literature for deriving TDOA and FDOA estimation algorithms [4].

There are several other models in the literature that represent successively more complicated scenarios. However, relatively basic models are typically used in actual theoretical development in order to realize closed-form solutions. A more general signal model, and one that is similar to the model used in Section 4.2 for new algorithm development, is

$$x(t) = s(t) + \sum_{i=1}^{p} s_i(t) + n_x(t) \tag{2.5}$$

$$y(t) = A_r s(t - D)\exp(j2\pi f_d t) + \sum_{i=1}^{p} s_i(t - D_i)\exp(j2\pi f_{d_i} t) + n_y(t) \tag{2.6}$$

where again $s(t)$ represents the SOI, $n_x(t)$ and $n_y(t)$ are zero-mean Gaussian noise terms, D is the TDOA, and the $s_i(t)$ term in both channels represents one or multiple SNOI, possibly from co-channel emitters. This model also takes into account amplitude and phase mismatch, Doppler shift, and the possibility that each SNOI can have a unique delay and Doppler shift. The value of this model is that it accommodates the fact that a SNOI can contribute unwanted correlations between receivers that can corrupt the TDOA and FDOA estimates for the SOI. Although this model is more descriptive of

real-world scenarios, it is mathematically complicated for theoretical work. Later in this thesis some simplifying assumptions are made to the model in order to facilitate theoretical progress.

2.2 Generalized Cross Correlation Method

There are two general methods for estimating the TDOA of a signal. The first method requires subtracting the *time-of-arrival* (TOA) estimates from two receivers to produce a relative measurement — i.e., the TDOA. The second method requires a cross correlation between the signal collected at one receiver with the signal collected at another receiver. The first method is only useful if there is an accurate timing reference between the transmitter and the receiver. The second method is more generally applicable and is the foundation of many of the most useful methods for estimating TDOA. One of these methods is called the *generalized cross correlation* (GCC) method of time delay estimation [2]. The GCC method was originally introduced as a method for estimating TDOA for a SOI in the absence of relative motion between receivers and the emitter. However, the GCC method can be used to produce a TDOA vs. time representation when the change in TDOA is small compared to the receiver sample rate. The GCC method concept can also be used in a modified algorithm, introduced in Section 2.4, that can iteratively estimate both TDOA and FDOA for a SOI.

The GCC method is best understood by using the signal model in (2.3) and (2.4), with $f_d = 0$ (no Doppler shift). The signal model then becomes

$$x(t) = s(t) + n_x(t) \tag{2.7}$$

$$y(t) = A_r s(t - D) + n_y(t) \tag{2.8}$$

where $s(t)$ represents the SOI, D is the TDOA, and $n_x(t)$ and $n_y(t)$ are zero-mean Gaussian noise terms. This model assumes there are no spectral components from a SNOI within the SOI frequency band, and there is no Doppler shift on the signals. However, this model does accommodate amplitude and phase mismatches between the receivers.

The autocorrelation and cross correlation functions computed using (2.7) and (2.8) become

$$R_x(\tau) = R_s(\tau) + R_{n_x}(\tau) \tag{2.9}$$

$$R_y(\tau) = |A_r|^2 R_s(\tau) + R_{n_y}(\tau) \tag{2.10}$$

$$R_{yx}(\tau) = A_r R_s(\tau - D) + R_{n_y n_x}(\tau) \tag{2.11}$$

where the signal and noise signals are assumed to be uncorrelated, and therefore their cross correlations are zero. In (2.11), D is the differential time delay, or the TDOA to be estimated. The auto spectral density and cross-spectral density functions are computed by taking the Fourier transform of (2.9)–(2.11), giving

$$S_x(f) = S_s(f) + S_{n_x}(f) \tag{2.12}$$

$$S_y(f) = |A_r|^2 S_s(f) + S_{n_y}(f) \tag{2.13}$$

$$S_{yx}(f) = A_r S_s(f) \exp(-j2\pi f D) + S_{n_y n_x}(f)\ . \tag{2.14}$$

The GCC method can be derived [1] using the cross-spectral density function in (2.14). Notice that the right side of (2.11) will be maximum when $\tau = D$, which is the TDOA of the SOI between the two receivers. If the *signal-to-noise-ratio* (SNR) is assumed to be sufficiently high, then the noise terms in (2.11) and (2.14) can be ignored. Taking the ratio of the cross-spectral density (2.14) with the auto-spectral density (2.12),

and noting that the SOI only occupies a finite bandwidth around the carrier frequency f_0, gives

$$\frac{S_{yx}(f)}{S_x(f)} = A_r \exp(j2\pi f D) \quad \text{for} \quad f_0 - \frac{B_s}{2} \leq f \leq f_0 + \frac{B_s}{2} \tag{2.15}$$

where B_s is the spectral bandwidth of the SOI. Taking the inverse Fourier transform of this ratio

$$\hat{R}_{yx}(\tau) = \int_{f_0 - B_s/2}^{f_0 + B_s/2} \frac{S_{yx}(f)}{S_x(f)} \exp(j2\pi f t)\, df \tag{2.16}$$

gives the weighted cross correlation estimate, which can be further expressed as

$$\hat{R}_{yx}(\tau) = \frac{A_r \sin(\pi B_s(\tau - D))}{\pi(\tau - D)} \exp(j2\pi f_0(\tau - D)) \,. \tag{2.17}$$

Notice that the real part of (2.17) is a sinc function multiplied by a sinusoid, which will peak at $\tau = D$. Equation (2.16) can be rewritten into a new form as

$$\hat{R}_{yx}(\tau) = \int_{f_0 - B_s/2}^{f_0 + B_s/2} \psi(f) S_{yx}(f) \exp(j2\pi f t)\, df \tag{2.18}$$

where $\psi(f)$ is now a weighting function equal to $1/S_x(f)$. Different weighting functions can be used that result in an expression similar to (2.17) where the correlation function peaks at $\tau = D$. For example, notice that using a weighting function of $\psi = 1$ reduces equation (2.18) to a simple cross correlation estimate. Given prior knowledge of the noise characteristics of the received signals it is possible to choose a weighting function that can help in reducing specific noise problems [2]. Several common weighting functions are listed in Table 2.1. The respective advantages and disadvantages of the various weighting functions have been thoroughly presented in [2, 3] and will not be repeated here.

Name	**Weighting Function**
Cross Correlation	1
ROTH	$\frac{1}{S_x(f)}$
SCOT	$\frac{1}{\sqrt{S_x(f)S_y(f)}}$
PHAT	$\frac{1}{S_{xy}(f)}$

Table 2.1: Common weighting functions for the GCC method.

An expression for the variance of the TDOA estimate computed using the GCC method was introduced in [3], to be

$$E(\hat{D} - D)^2 = \frac{3}{4\pi^2}\frac{1}{T}\frac{1}{B_s^3}\frac{1}{\gamma} \; . \tag{2.19}$$

Equation (2.19) relates the estimation variance to the observation time T, receiver effective-SNR $1/\gamma$, and the signal bandwidth B_s. The effective-SNR is defined in [2] to be

$$\frac{1}{\gamma} = \frac{1}{2}\left[\frac{1}{\gamma_1} + \frac{1}{\gamma_2} + \frac{1}{\gamma_1\gamma_2}\right] \tag{2.20}$$

where γ_1 and γ_2 are the individual SNR's at the first and second receivers respectively. According to (2.19), the TDOA estimate accuracy improves — i.e., estimate variance decreases, with increased signal bandwidth, greater effective SNR and longer observation time.

Figure 2.1 shows a block diagram for the process of computing the GCC output. There are several techniques presented in the literature for computing the GCC output [2]. However, most of them require some prior knowledge about the noise environment. When no prior knowledge about the noise environment exists, the best weighting function to use (and the one used for the examples in this section) is computed by

$$\psi(f) = 1/\sqrt{S_x(f)S_y(f)}\ , \tag{2.21}$$

and is commonly called the *smoothed coherence transform*, or SCOT method (See Table 2.1).

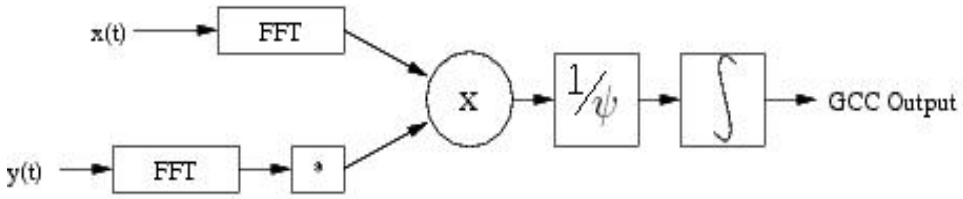

Figure 2.1: GCC block diagram.

2.2.1 GCC Examples

In this section several examples are presented using the GCC method to estimate TDOA for a SOI. For each example, and the examples that follow in later sections, a program was developed in Matlab that simulates collection geometries with independent positions and velocities for both the receivers and the emitters. The simulated signals for both the SOI and the SNOI are rectangular windowed *binary phase shift keyed* (BPSK) signals that have been downconverted to an *intermediate frequency* (IF). Appendix B

describes these simulated signals in more detail. The signal parameters used to simulate these signals are listed in Table 2.2.

SOI Parameters	**SNOI Parameters**
$f_{IF} = \frac{63}{256} fs$	$f_{IF} = \frac{56}{256} f_s$
$R_{sym} = \frac{16}{256} fs$	$R_{sym} = \frac{26}{256} f_s$
$f_s = 1e^6$ Hz	$f_s = 1e^6$ Hz
SNR = Adjustable	SNR = Adjustable
FDOA $= -850.0Hz$ *	FDOA $= -845.0Hz$ *
TDOA $= 70.0\mu s$ *	TDOA $= 63.3\mu s$ *
* At center of collection time	

Table 2.2: SOI and SNOI signal parameters used for simulating signals used in examples.

For all simulations the SOI emitter was assumed to be located at the origin of the Cartesian coordinate system, or *flat-earth* model, shown in Figure 2.2. The use of a flat-earth model simplifies the processing by assuming that the emitter and collectors exist on or above a plane. Obviously, real-world systems involve curves in three-dimensional space with spherical geometry, rather than planar geometry. However, a flat-earth model is sufficient for evaluating the performance capabilities of the algorithms presented in this thesis. In Figure 2.2, receiver 1 is a stationary ground-based receiver that is 5 km away from the SOI emitter. Receiver 2 is an airborne receiver with a projected ground distance of 30 km from the SOI emitter. The airborne receiver is flying directly toward

the SOI emitter with an altitude of approximately 24,000 feet and a speed of 150 meters per second.

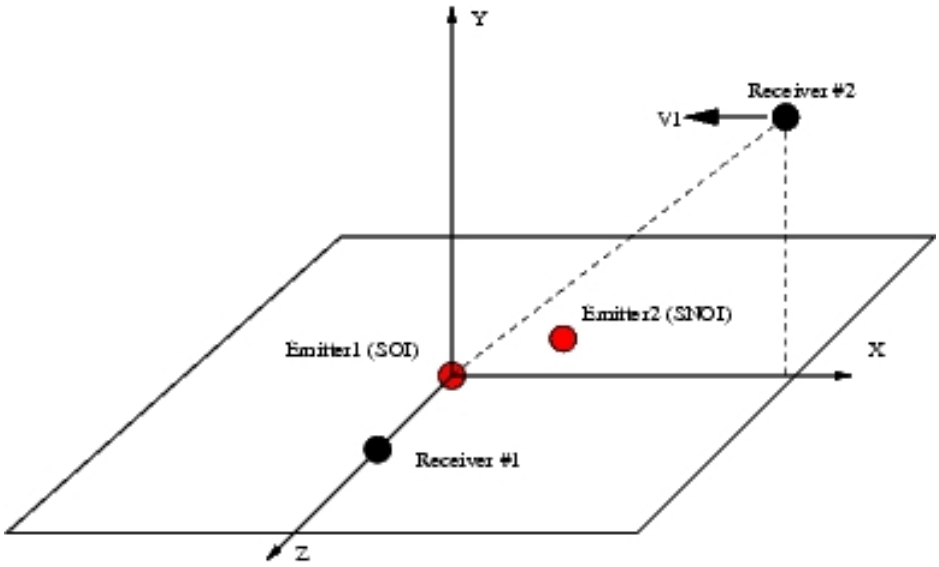

Figure 2.2: Collection geometry for simulated examples.

Notice that in Figure 2.2 the Y-axis represents altitude above the earth with the X-axis and Z-axis making up the ground plane. Both the ground receiver and the airborne receiver are labeled along with the location of the SOI emitter and the SNOI emitter. Figure 2.2 represents an instantaneous moment-in-time snapshot of the collection geometry. Since the receivers and/or emitters are moving at their respective velocities, the geometry changes with each passing instant of time. This is precisely why the TDOAs and FDOAs are coupled (see Appendix A) in real-world emitter-collector scenarios. In all of the examples presented in this thesis, both receiver sample rates are the same.

Figure 2.3 displays a plot of the GCC output when only the SOI and AWGN noise are present at the receivers, and there is no Doppler shift — i.e., both receivers are stationary. Also, the SNR at both receivers is simulated to be 20 dB. This represents a high SNR scenario. Obviously, one might expect a different SNR at each receiver since one receiver is much further away from the SOI emitter than the other. However, for

convenience it is assumed that due to antenna and system gains they are equal before sampling. Recall from Table 2.2 that the predicted TDOA for the SOI based on the collection geometry is 70.0 microseconds. The TDOA measured from the peak in the GCC output plot in Figure 2.3 is also 70.0 microseconds. Note that the sample spacing between TDOA samples is $1/f_s = 1.0$ microseconds since there is no zero padding on the *inverse fast Fourier transform* (IFFT) used to compute the cross correlation estimates. Smaller sample spacings can be achieved by zero padding prior to the GCC output transform, or by using interpolation on the output.

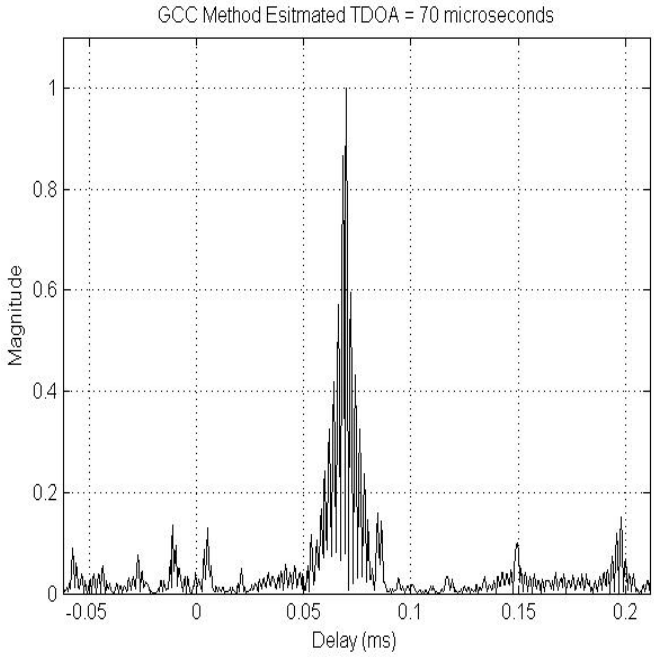

Figure 2.3: GCC SCOT method output for the BPSK SOI listed in Table 2.2 and collected by two spatially separated stationary receivers. The data record length was 2048 samples and SNR = 20 dB at both receivers. Both receiver sample rate were 1 MHz.

The plot in Figure 2.4 shows the GCC output when the SNR at both receivers is simulated to be -10 dB. This represents a low SNR scenario, and it is clear from the plot that a TDOA measurement cannot be made. Remember, that according to (2.19) the

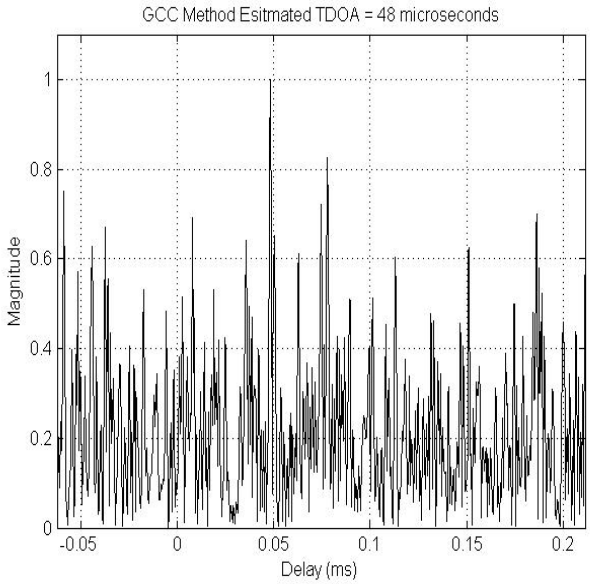

Figure 2.4: GCC SCOT method output for the BPSK SOI listed in Table 2.2 and collected by two spatially separated stationary receivers. The data record length was 2048 samples and SNR = -10 dB at both receivers. Both receiver sample rate were 1 MHz.

GCC method's ability to produce an accurate estimate when the effective-SNR is low is determined by the signal bandwidth and the observation time. Of course, since the signal bandwidth is fixed, the only option is to use a longer observation time, possibly with averaging. However, this is not always an option in real applications due to time-varying effects, etc.

Significant Doppler shift can also be a problem when using the GCC method. Figure 2.5 shows the GCC output for a high SNR scenario where the received signal at the airborne collector has a 850 Hz Doppler shift due to relative motion between the receiver and the SOI emitter. It is easy to see from the plot that a TDOA measurement cannot be made from the GCC output due to loss of coherence. This demonstrates a weakness of the GCC method for use in emitter location applications. As the Doppler shift on the SOI becomes higher, the GCC processing becomes less coherent over the collection

duration until no correlation between signal replicas at the two receivers is possible. Unless additional processing can be used to make the received signals coherent, the GCC method is not suited for use when there is an expected large Doppler shift on the SOI.

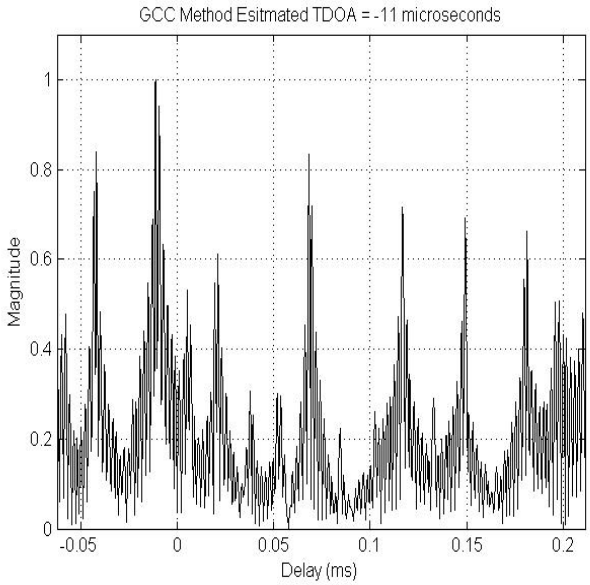

Figure 2.5: GCC SCOT algorithm output for the BPSK SOI listed in Table 2.2 and collected by two spatially separated receivers. The signal at the second receiver has a Doppler shift of -850 Hz due to motion of the receiver. The data record length was 2048 samples and the SNR = 20 dB at both receivers. Both receiver sample rate were 1 MHz.

It was mentioned in the introduction that *co-channel interference*, or CCI, can have a deleterious effect on conventional TDOA and FDOA estimation methods. To demonstrate this fact, Figures 2.6 and 2.7 show two GCC output plots from a case where the SOI is corrupted by a SNOI. Since the SNOI completely overlaps the SOI spectrally, this represents a wide-band interference environment. The SNOI emitter is also approximately only 1 km away from the SOI emitter. The plot in Figure 2.6 shows the results when the SOI and the SNOI have the same SNR of 20 dB at both receivers. This makes the *signal-to-interference-ratio* (SIR) equal to 0 dB. The largest peak in the GCC

output can be measured at a TDOA of 63 microseconds. This is the predicted TDOA for the SNOI. The TDOA for the SOI is more difficult to measure. Although there is a peak at 70 microseconds, due to the other peaks in the vicinity having almost the same magnitude it is not possible to confidently make a measurement.

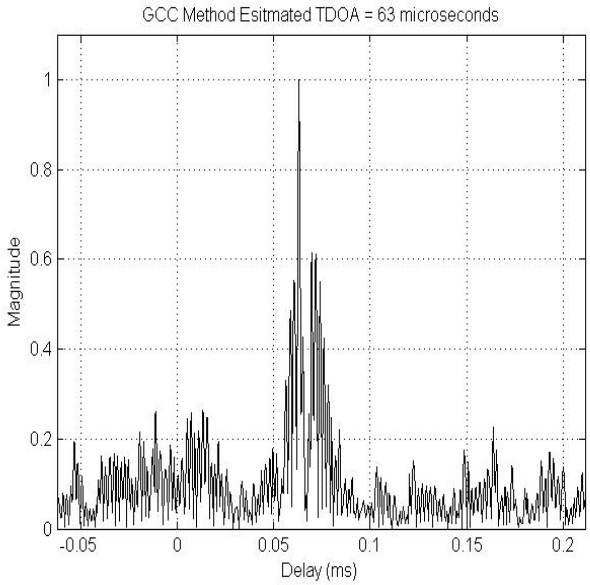

Figure 2.6: GCC SCOT output for the BPSK SOI and BPSK SNOI listed in Table 2.2 and collected by two spatially separated stationary receivers. The data record length was 2048 samples and the SNR = 20 dB at both receivers. Both receiver sample rate were 1 MHz. The distance between the SOI and SNOI emitters is 1 km.

The plot in Figure 2.7 shows the same example but with a 0.5 km distance between the SOI and SNOI emitters. A single peak is produced that does not correspond to the predicted SOI TDOA, but instead to the predicted SNOI TDOA. This can be considered a biased estimate of the SOI TDOA. This demonstrates that the GCC method can fail to produce accurate, or unbiased TDOA estimates when certain CCI conditions occur.

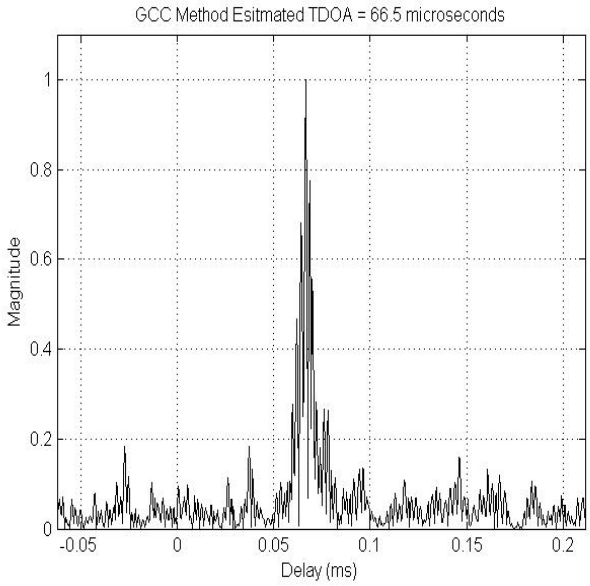

Figure 2.7: GCC SCOT output for the BPSK SOI and BPSK SNOI listed in Table 2.2 and collected by two spatially separated stationary receivers. The data record length was 2048 samples and the SNR = 20 dB at both receivers. Both receiver sample rate were 1 MHz. The distance between the SOI and SNOI emitters is 0.5 km.

2.2.2 GCC TDOA vs. Time Representation

The GCC method can be used to form a TDOA vs. time representation that is useful for looking at signals with intermittent on/off durations or signals with slowly changing TDOA. Figures 2.8 and 2.9 show a TDOA vs. time representations computed using the GCC SCOT method. For these examples, different SOI parameters than those listed in Table 2.2 have been used for convenience, and a long duration data record has been used in order to demonstrate the changing TDOA due to the airborne platform moving toward and then away from the SOI emitter location. Using the TDOA vs. Time representation, the TDOA corresponding to the SOI can be tracked over the entire collection duration. This is a special application that could also be applied to a slowly moving emitter.

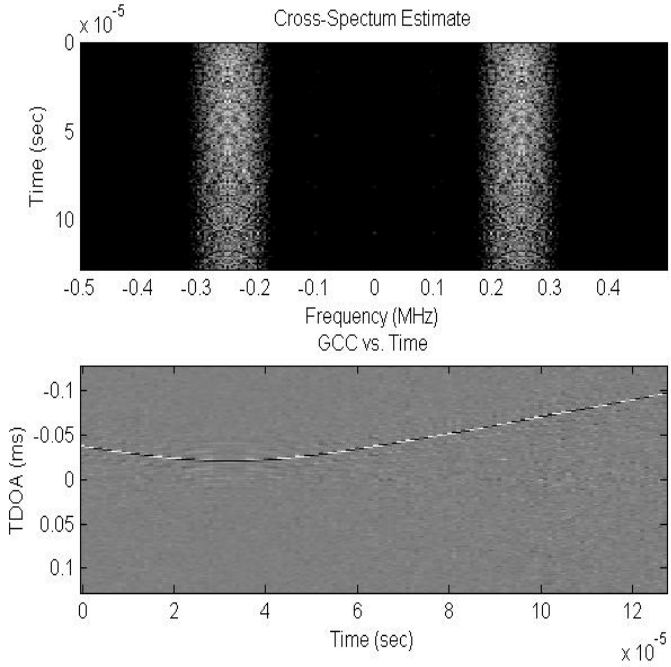

Figure 2.8: GCC vs. time for BPSK SOI showing time-varying TDOA estimates. SOI used a 250 kHz center frequency and 100 kHz symbol rate. The data record length was 65,536 samples and the receiver sample rate was 1 MHz. Receiver 1 was stationary while receiver 2 was moving with a velocity of 30 km/s.

Figure 2.9 demonstrates a scenario where both a SOI and a SNOI are present. Again,

the SNOI parameters are different than those listed in Table 2.2. In this example the SNOI originates from an emitter that is a large distance away from the SOI emitter so that both the SOI and the SNOI have distinct TDOAs during most of the collection even though they overlap spectrally. Although the TDOA vs. time representation provides a useful tool for some applications, it still suffers from the limitations of the GCC method in regards to CCI and closely located emitters.

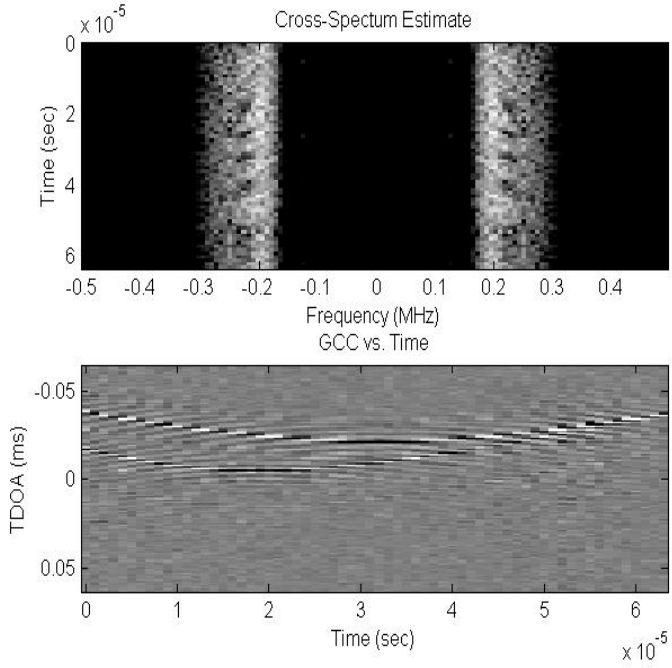

Figure 2.9: GCC vs. time for BPSK SOI and BPSK SNOI showing time-varying TDOA estimates. SOI used a 250 kHz center frequency and 100 kHz symbol rate. The SNOI used a 200 kHz center frequency and 50 kHz symbol rate. The data record length was 65,536 samples and the receiver sample rate was 1 MHz. Receiver 1 was stationary while receiver 2 was moving with a velocity of 30 km/s. The SNOI emitter was also moving at 10 km/s

2.3 Cross Ambiguity Function Method

Cross ambiguity function, or CAF, processing is a method for jointly estimating TDOA and FDOA. Unlike the GCC method, it can be used when the SOI experiences a large Doppler shift, and it can separate a SOI from a SNOI in the FDOA dimension as well as the TDOA dimension if the differences in the TDOA and FDOA estimates are resolvable. Before getting into the details of the CAF method, it is useful to further understand the concepts behind FDOA and how it relates to TDOA.

The time-dependent propagation delay from an emitter to a receiver can be expressed as

$$D(t) = \frac{R(t)}{c} \tag{2.22}$$

where $R(t)$ is the time-dependent range, or distance, from the emitter to the receiver, and c is the speed of light. The range can be expanded into a Taylor series as

$$R(t) = R_0 + \frac{dR}{dt}t + \frac{1}{2}\frac{d^2R}{dt^2}t^2 + \dots \ . \tag{2.23}$$

If the observation interval is short, and the velocity of the receiver is relatively constant over the observation interval, then the following approximation can be made

$$R(t) \approx R_0 + \frac{dR}{dt}t = R_0 + v_r t \tag{2.24}$$

where v_r is the magnitude of the receiver's radial velocity in the direction of the emitter. Using the approximation in (2.24) with (2.22), a received signal $s_r(t)$ can be modeled as

$$s_r(t) = s\left(t - D(t)\right) \approx s\left((1 - v_r/c)t - R_0/c\right) \tag{2.25}$$

where

$$R_0 = \sqrt{(x - x_e)^2 + (y - y_e)^2 + (z - z_e)^2} \tag{2.26}$$

is the range to the emitter, with the receiver coordinates (x, y, z) and the emitter coordinates (x_e, y_e, z_e). Letting $D = R_0/c$ be the time independent propagation delay, assuming that $v_r << c$, and taking the general model of the emitted signal to be

$$s(t) = A(t) \exp\left(j(2\pi f_c t + \phi(t))\right) \tag{2.27}$$

the received signal in (2.25) can be expressed as

$$s_r(t) = A(t - D) \exp(j\phi(t - D)) \exp\left(j2\pi f_c t\right) \exp\left(-j2\pi f_d t\right) \exp\left(-j2\pi f_c D\right) \tag{2.28}$$

where f_c is the carrier frequency, $f_d = f_c v_r/c$ is a Doppler shift, and $A(t-D)\exp(j\phi(t-D))$ is a complex amplitude term. It is easy to see that (2.28) has a carrier frequency term, a constant phase term, and a Doppler shift term, in addition to the received signal complex amplitude. The goal of the CAF processing method is to estimate the propagation delay, D, and the Doppler shift, f_d. Therefore, the CAF should be expected to take the form of a two-dimensional correlation function over parameters TDOA and FDOA.

It is reasonable at this point to ask how TDOA is related to FDOA. In Appendix A, this relationship is derived to be

$$FDOA = \frac{f}{c}(v_{r1} - v_{r2}) = (f_c)\frac{d(TDOA)}{dt} \tag{2.29}$$

where v_{r1} and v_{r2} are the velocities of the two separated receivers in the direction of the emitter. In general, (2.29) says that a changing TDOA over the observation period gives

rise to a differential Doppler shift, or FDOA. This is why it is important to consider the collection geometry when simulating signals to use for testing algorithms. The TDOA and FDOA are coupled kinematic parameters, so one cannot independently simulate them without considering the coupling effects through the collection geometry.

In the case of two receivers, CAF processing can be considered as a method similar to finding the inner product between two vector spaces. In a two-dimensional vector space, the inner product of two vectors will be maximum when the angle between the vectors is zero. Following the same reasoning, the output of some yet-to-be-defined process will be maximum when the two received signals correlate in time and frequency. If our received signal model is

$$x(t) = s(t) + n_x(t) \tag{2.30}$$

$$y(t) = A_r s(t - D)\exp(j2\pi f_d t) + n_y(t) \tag{2.31}$$

then the signal at one receiver can be incrementally delayed and time-shifted until the output of the inner product between (2.30) and (2.31) is maximized. This concept can be mathematically expressed by

$$A(\tau, f) = \int_0^T x(t)y^*(t + \tau)\exp(-j2\pi f t)\, dt \tag{2.32}$$

which is the expression for the conventional *cross ambiguity function*, or CAF. Notice that when $f = 0$, (2.32) reduces to a simple cross correlation function estimate. Taking the magnitude of both sides of (2.32) results in

$$|A(\tau, f)| = \left| \int_0^T x(t)y^*(t + \tau)\exp(-j2\pi f t)\, dt \right| , \tag{2.33}$$

which is the conventional complex CAF magnitude [4].

In order to gain further insight, it is useful to substitute the received signals into (2.32) and expand the terms from (2.28) for the received signal y. Ignoring the carrier frequency term and the constant phase term, this yields

$$A(\tau, f) = \int_0^T s_x(t) \left[A_r^* \exp(-j2\pi(f - f_d)t) \exp(j2\pi f_d \tau))\right] \, dt \tag{2.34}$$

where f_d is the Doppler shift parameter and D is the time-delay parameter to be estimated, and

$$A_r = A(t - D + \tau) \exp(j\phi(t - D + \tau)) \tag{2.35}$$

is the received signal complex amplitude. Note that the propagation delay is only included in the received signal y. The received signal x can be replaced with the emitted signal model in (2.27) without loss of generality. Clearly, the output of (2.34) is maximum when $f = f_d$ and $\tau = D$.

The accuracy of the TDOA and FDOA estimates can be summarized with the following equations relating the standard deviation to the system parameters [4]:

$$\sigma_{TDOA} \approx \frac{0.55}{B_s} \frac{1}{\sqrt{B_n T \gamma}} \tag{2.36}$$

$$\sigma_{FDOA} \approx \frac{0.55}{T} \frac{1}{\sqrt{B_n T \gamma}} \tag{2.37}$$

where B_s is the signal RF bandwidth, B_n is the noise bandwidth of the receiver, T is the total observation time, and γ is the effective-SNR defined in (2.20). These equations also represent the CRLB on TDOA and FDOA estimation using the conventional CAF [4].

Looking closer at (2.36) and (2.37) it is possible to predict that given a fixed SNR at the receivers, a narrow bandwidth signal requires a long observation time in order to

achieve a good TDOA estimate. This in turn results in a very good FDOA estimate. However, long observation times may cause the CAF peak to smear if TDOA and FDOA are not relatively constant over the observation time. It is worth emphasizing that for a given input SNR and input bandwidth, the observation time, T, determines the accuracy with which both TDOA and FDOA can be measured for a SOI.

In the discrete, sampled time case, the CAF is defined by substituting $t = nT_s$ and $f = \frac{kf_s}{N}$ into (2.32). This yields the expression

$$A(\tau, k) = \sum_{n=0}^{N-1} x(n)y^*(n + D) \exp\left(-j2\pi\frac{kn}{N}\right) \tag{2.38}$$

where T_s is the sample period, $f_s = 1/T_s$ is the sampling frequency, n represents individual sample numbers, N is the total number of samples, and k represents the frequency bin index, in which the actual frequency shift in Hz is k/NT_s). The magnitude of (2.38) will likewise peak when D (in integer sample units) and k/NT_s are closest in sample units to the TDOA and FDOA, respectively. For a random signal with no hidden periodicities, the peak will have a nominal width in the TDOA dimension that is proportional to $1/B_s$, where B_s is the nominal width of the signal power spectrum [4]. Likewise, the peak width in the FDOA direction will be proportional to $1/(NT_s)$. This is why the conventional methods produce biased estimates when emitters are too close together. For example, if two emitters transmit signals with the same bandwidth of 100 kHz, then their corresponding TDOAs will need to be at least $1/B_s = 10$ microseconds apart in order to get separate unique peaks from the CAF output. Note that the actual TDOA will depend on the collection geometry. Likewise, if the collection length is 100 milliseconds long then the FDOAs must differ by more than $1/T = 10$ Hz.

As an example, the left plot in Figure 2.10 shows a detection surface, called a CAF surface, generated by computing the CAF magnitude over a defined range of TDOA and

FDOA values. The SOI parameters are listed in Table 2.2 and the collection geometry is the same as it was for the GCC examples (See Figure 2.2). The SNR at both receivers was fixed at 20 dB and the receiver sample rate was 1 MHz. For the computation 2048 samples were used, giving a collection duration of $2048 \times T_s = 2048$ microseconds. The right plot in Figure 2.10 is a top view of the CAF detection surface, providing an alternative representation that can be instructive. It is easy to see that the CAF surface contains a peak at coordinates corresponding to the estimated TDOA and FDOA values. From this peak the TDOA is measured to be 69.0 microseconds. For comparison the predicted TDOA value is 70.0 microseconds. The measured FDOA is -846 Hz and the predicted FDOA is -850 Hz. Note that no interpolation has been used on the output to get more precise measurements. Of course, higher resolution FDOA estimates are possible with longer data record.

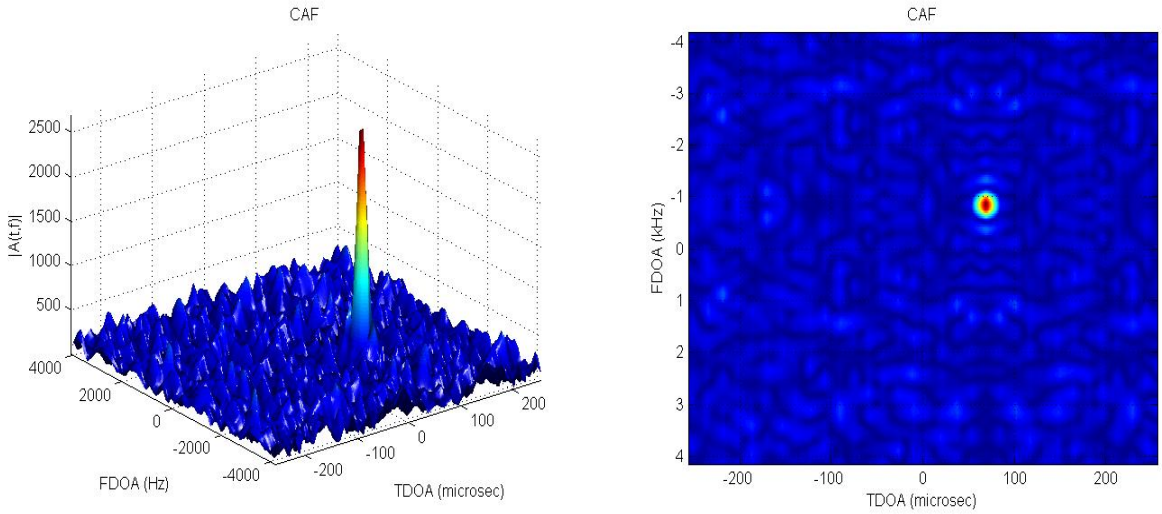

Figure 2.10: CAF surface for BPSK SOI collected at two spatially separated receivers with an SNR = 20 dB at both receivers. The data record length was 2048 samples and the receiver sample rates were 1 MHz. The peak location in the surface corresponds to the TDOA and FDOA estimates. (Left). Top view of CAF surface on the left (Right).

Figure 2.11 shows cross-section plots through the peak in the CAF surface from Figure

(2.10) in both the TDOA and FDOA dimensions. From these cross-section plots it is easy to measure the peak locations at the estimated TDOA and FDOA values. Figures 2.12 and 2.13 are similar to Figures 2.10 and 2.11, but the SNR at the receivers was -5 dB.

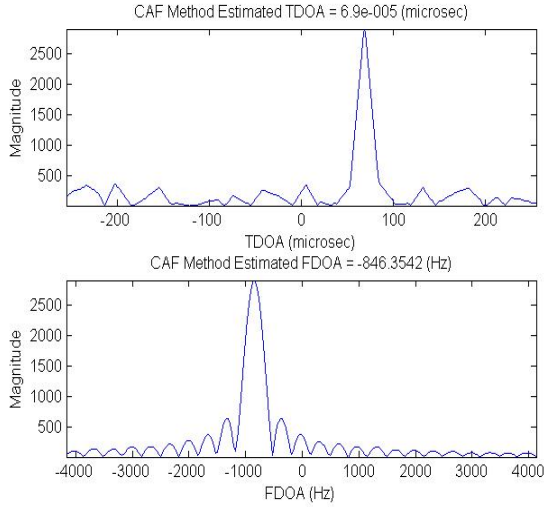

Figure 2.11: Cross-section plots through Figure 2.10 CAF surface in both the TDOA and FDOA dimensions showing a TDOA peak at 69 microseconds and an FDOA peak at -846 Hz.

In some applications it is necessary to estimate TDOA and FDOA in real-time, or near-real-time. However, CAF processing using direct computation of (2.38) is very computationally intensive, and unless reduced data segments are used, it is often not practical for most real-time applications. Also, direct computation of (2.38) estimates TDOA for the range $-NT_s$ to NT_s and FDOA for the range $-\frac{f_s}{2}$ to $\frac{f_s}{2}$. Searching this entire range requires $2N^2$ calculations, which becomes a difficult task for long data records — i.e., large N. There are several published algorithms for computing the CAF surface that provide some increased efficiency [4, 5]. Generally, these algorithms use a *coarse* search over a decimated version of the entire data record followed by a *fine* computation with interpolation over a reduced TDOA/FDOA evaluation range with the

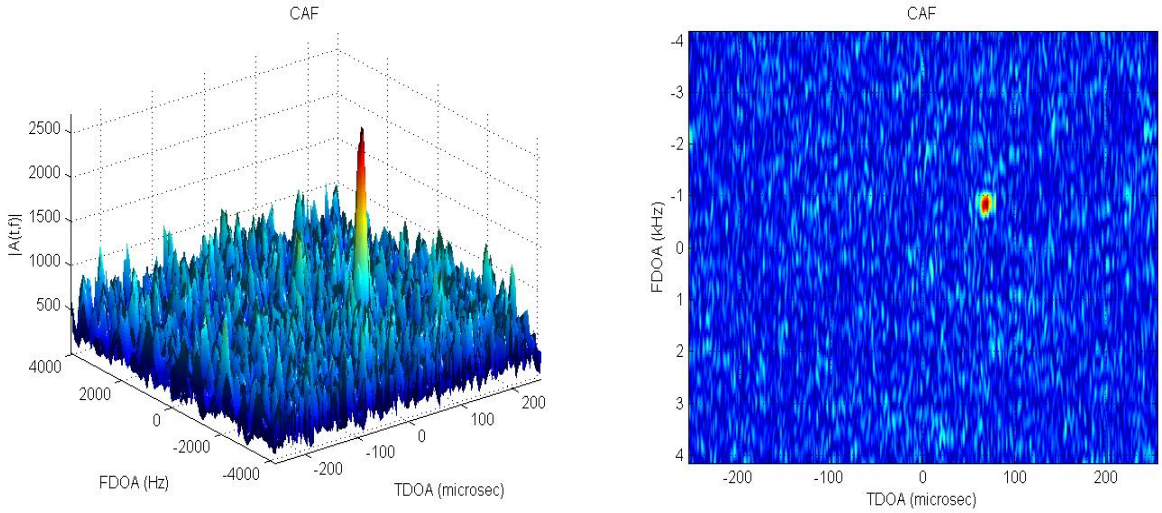

Figure 2.12: CAF surface for BPSK SOI collected at two spatially separated receivers with an SNR = 20 dB at both receivers. The data record length was 2048 samples and the receiver sample rates were 1 MHz. The peak location in the surface corresponds to the TDOA and FDOA estimates. (Left). Top view of CAF surface on the left (Right).

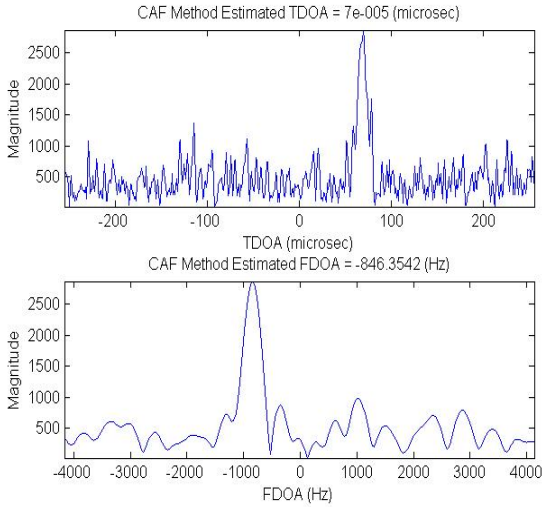

Figure 2.13: Cross-section plots through Figure 2.12 CAF surface in both the TDOA and FDOA dimensions showing a TDOA peak at 69 microseconds and an FDOA peak at -846 Hz.

entire data set. The coarse search can be skipped if there is fairly good prior knowledge of the actual TDOA and FDOA for the SOI. Details on how to compute the CAF surface

using various more high computational efficiency algorithms can be found in several excellent papers [4, 6, 7, 8] and will not be included here.

2.3.1 CAF Examples

In this section several examples of computed CAF surfaces using simulated data are demonstrated. Each example attempts to represent a realistic collection scenario. However, two assumptions are made: 1) The simulated signals are corrupted with zero-mean Gaussian noise. 2) The interference signal is simulated as a co-channel signal, or SNOI, that overlaps temporally and spectrally with the SOI. The SNOI has the same modulation as the SOI, but a different symbol rate and carrier frequency.

Figure 2.14 shows a CAF surface generated using data from a simulated collection that includes both a SOI and a SNOI. The SNOI is from a co-channel emitter that is approximately 1 km away from the SOI emitter. The SIR at both receivers is 0 dB. The collection geometry is the same as that used for the GCC examples in Chapter 2 and is illustrated in Figure 2.2. The SOI and SNOI parameters are listed in Table 2.2. Notice that the SNOI completely overlaps the SOI spectrally, making this an example of wide-band CCI. The SNOI is also spatially close to the SOI. Both a 3-D view of the CAF surface and a top-down 2-D view of the surface are displayed. Figure 2.15 displays the cross-section plots through the CAF surface peak in both the TDOA and FDOA dimensions.

It is easy to see in Figure 2.14 that, similar to the GCC method, the TDOA for both the SOI and the SNOI is not completely resolvable and difficult to measure. However, unlike the GCC method the CAF method worked with a Doppler shifted signal. The peak corresponding to the SOI is distorted due to the interference of the SNOI and it is not at the same TDOA and FDOA locations measured when only the SOI was present.

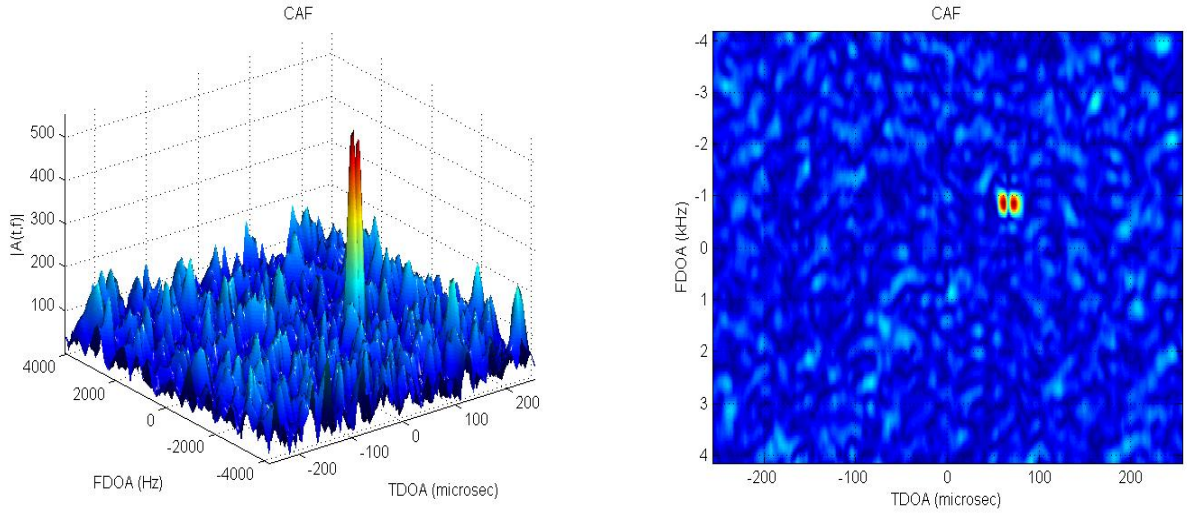

Figure 2.14: CAF surface computed from BPSK SOI and BPSK SNOI collected at two spatially separated receivers with an SIR = 0 dB. The signals were emitted from locations that are 1 km apart. The data record length was 2048 samples and the receiver sample rates were 1 MHz. (Left). Top view of CAF surface on the left (Right).

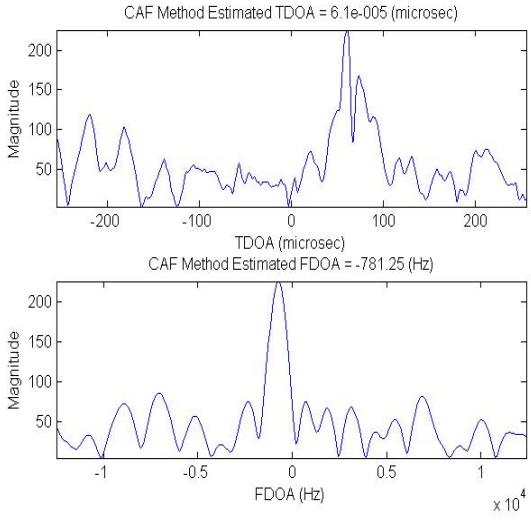

Figure 2.15: Cross-section plots through Figure 2.14 CAF surface in both the TDOA and FDOA dimensions.

In fact, the SOI TDOA is measured to be 65 microseconds and the FDOA to be -850 Hz. This demonstrates the effects from the SOI and SNOI overlapping spectrally, and originating from emitters that are located spatially close together. Figures 2.16 and 2.17

demonstrate the same scenario, but with a SIR of -10 dB at the receivers.

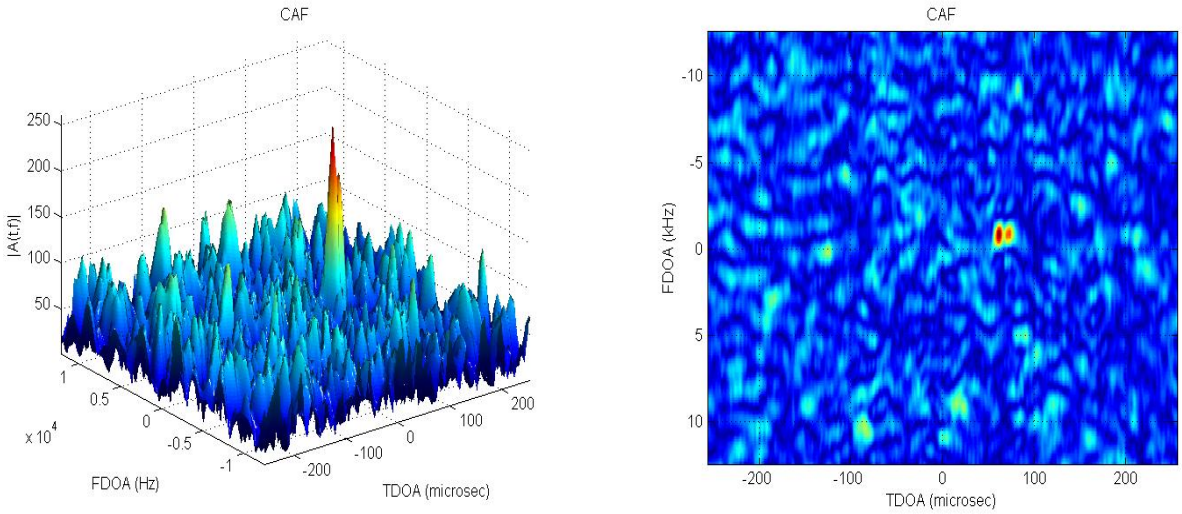

Figure 2.16: CAF surface computed from BPSK SOI and BPSK SNOI collected at two spatially separated receivers with an SIR = -10 dB. The signals were emitted from locations that are 1 km apart. The data record length was 2048 samples and the receiver sample rates were 1 MHz (Left). Top view of CAF surface on the left (Right).

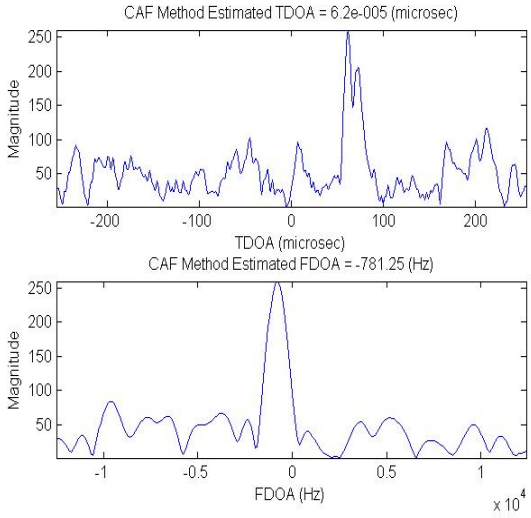

Figure 2.17: Cross-section plots through Figure 2.16 CAF surface in both the TDOA and FDOA dimension.

Because of the SNOI emitter location and the spectral overlapping, there is not a unique peak in the CAF surface corresponding to the SOI. The TDOA measured is biased toward

the actual SNOI TDOA. This problem would become even more severe for emitters less than 1 km apart.

For another example, Figures 2.18 and 2.19 demonstrate the CAF surface computed with the SOI emitter and the SNOI emitter only 0.5 km apart. The SIR was simulated to be 0 dB. This represents a more severe case of CCI where the TDOA for the SOI and the TDOA for the SNOI are too close to resolve in the CAF surface. Since the signals are spectrally overlapping, prefiltering cannot be used before the CAF computation in order to separate the signals. In this case, only FDOA can be unique. However, with the center frequencies only differing by a small amount, the difference in Doppler shift will also be small. Therefore, separating the signals based on their FDOAs is not practical. The TDOA and FDOA measurements from Figure 2.19 correlate with the predicted SNOI TDOA and FDOA. This can be viewed as a biased estimate of the SOI kinematic parameters, and it would result in an incorrect geolocation estimate for the SOI emitter in a real application.

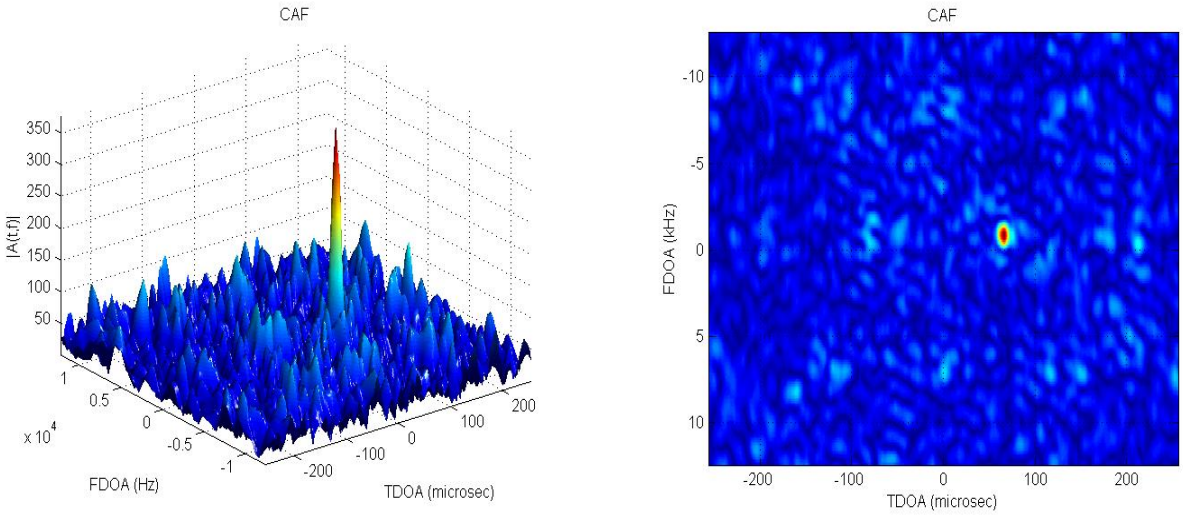

Figure 2.18: CAF surface from BPSK SOI and BPSK SNOI collected at two spatially separated receivers with an SIR = -10 dB. The signals were emitted from locations that are 0.5 km apart. The data record length was 2048 samples and the receiver sample rates were 1 MHz (Left). Top view of CAF surface on the left (Right).

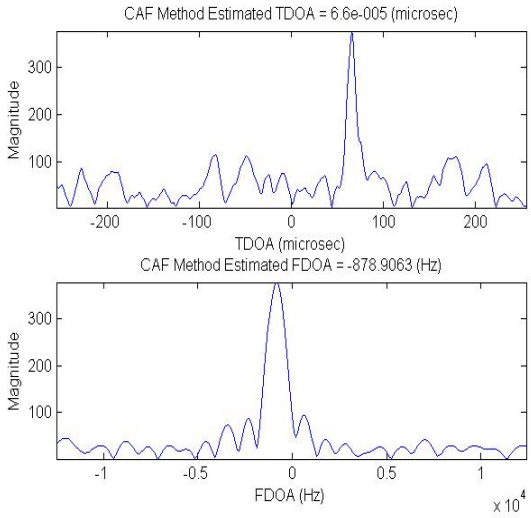

Figure 2.19: Cross-section plots through the Figure 2.18 CAF surface in both the TDOA and FDOA dimensions.

As the examples in this section have demonstrated, in scenarios where the SOI is in a CCI environment the CAF method may not perform to the level needed to get reliable, unbiased estimates. To overcome the limitations of the CAF method it is necessary to exploit additional signal properties that enable the co-channel signals to be separated. Cyclostationarity has been shown to be useful for separating bauded signals, and for estimating TDOA for a SOI that is corrupted by CCI [9, 10]. In Chapter 4 it will be demonstrated that it can also be exploited to *jointly* estimate both TDOA and FDOA for a SOI in a CCI environment. However, it is informative to first look at another conventional estimation method that is based on the GCC concept, and which can be used to iteratively estimate both TDOA and FDOA.

2.4 Hybrid Method

When CCI is not an issue the GCC method has proved to be useful for TDOA estimation, and it can be computed efficiently using the *fast Fourier transform* (FFT)

[1]. It was demonstrated in the examples in Section 2.2.2 that it can also be used to compute a TDOA vs. time representation that is useful for detecting intermittent signals or tracking a slowly changing TDOA over long durations. In contrast, the CAF method can jointly estimate both TDOA and FDOA, making it useful for applications where there is relative motion between an emitter and one or more of the receivers. The CAF method outputs a two-dimensional TDOA vs. FDOA surface, called a CAF surface. The CAF surface can be used for signal detection [4]. After detection, the peak locations in the CAF surface correspond to the TDOA and FDOA measurements. As mentioned earlier, the CAF method can be computationally complex, requiring a lot of computational resources. Therefore, in some applications it may be useful to compromise the capabilities of the CAF and use a simpler technique that can iteratively compute both TDOA and FDOA estimates. This section will introduce one such method that is based around the GCC concept.

The GCC method can be modified into a *hybrid* method to create a two-dimensional detection surface similar in some aspects to the CAF surface. Although the *hybrid* method is not a true joint estimator like the CAF method, it requires less computational resources, making it practical for applications where the CAF may be too computationally demanding.

Similar to the GCC SCOT method in Section 2.2, the *hybrid* method uses a normalized cross spectrum, sometimes called the coherence function, given by

$$C_{yx}(f) = \frac{S_{xy}(f)}{\sqrt{S_x(f)S_y(f)}} \, . \tag{2.39}$$

For the *hybrid* method, (2.39) is computed over $n = 0, 1, \ldots, N-1$ samples of the received signal. This computation is repeated as a window, N samples in length, slides over the data until M frames of N samples have been transformed, each frame represent-

ing the normalized cross spectrum for a given time window. Similar to the periodogram method of spectral estimation, each frame overlaps the previous frame in time by 50–75 percent. This process forms a two-dimensional array of normalized cross spectrum samples. The rows of the array will be made up of the frequency samples of the cross spectrum with each sample in a given column representing a frequency sample for a given time within the collection period. Now, instead of taking the IFFT of each row to get the TDOA vs. time output described in section 2.2.2, a sub-band of l samples at the beginning of each row is selected, with $l << N$. The zero-padded IFFT of this sub-band is computed giving a cross correlation sequence estimate for the sub-band bandwidth. This sub-band processing is repeated using overlapping sub bands across each row of the cross spectrum array. After time-averaging all of the sub-band cross correlation estimates for each row, the result is a time-averaged cross correlation estimate for several sub-band bandwidths. This process has transformed the normalized cross spectrum array into a frequency vs. lag array. Since a peak in the cross correlation sequences represents a TDOA measurement, the magnitude of the frequency vs. lag array can be called the RF vs. TDOA surface without loss of generality. Figure 2.20 displays a simple diagram depicting the computation of the RF vs. TDOA surface. Like the CAF surface, this surface is also useful for signal detection.

When computing the RF vs. TDOA surface, both the transform length and the sub-band bandwidth can be selected. One of the advantages of the RF vs. TDOA surface over the TDOA vs. time surface is the ability to estimate a signal's bandwidth in addition to its time-delay. Obviously, the resolution of this measurement will depend on the selected sub-band size and the time-window duration of each frame. Once the TDOA for a signal is measured, the cross correlation sequence sample index corresponding to the detected TDOA peak can be used to extract a sample from each frame, giving a time-series of cross correlation sequence samples. Each sample in the time-series will be spaced in

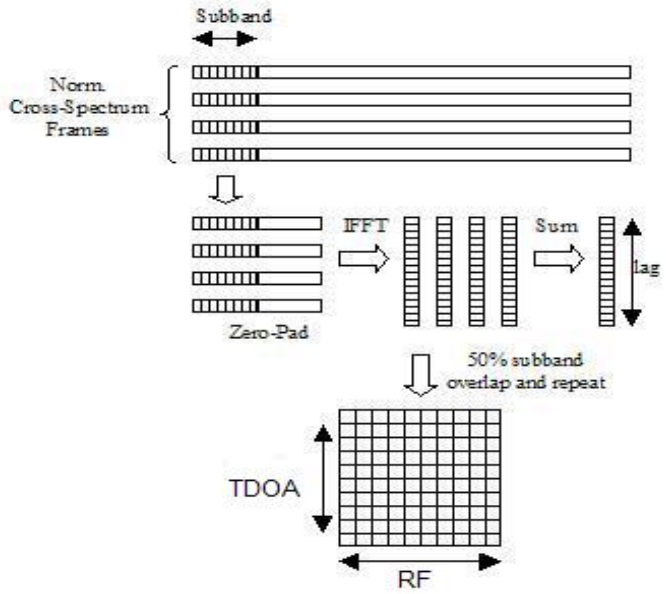

Figure 2.20: Diagram outlining the RF vs. TDOA computation using the *hybrid* method.

time based to the frame size and overlap used to create the initial cross spectrum array. Time overlapping when computing the normalized cross correlation frames will decrease the time between samples in the time-series, effectively increasing the sample rate. It is important to note that the sample spacing must be able to support the largest differential Doppler frequency expected by the collection geometry. Taking the zero-padded Fourier transform of the time-series will result in a peak that corresponds to the FDOA of the received signal. Figure 2.21 shows a simple depiction of the time-series extraction and processing.

The advantage of the modified GCC method, or *hybrid* method, is that it maintains the computational simplicity of the conventional GCC method, and therefore can be used to estimate FDOA while avoiding the computational complexity of the CAF method. Also, large bandwidths can be processed efficiently and no prior knowledge about the received signal is necessary in order to get TDOA and FDOA measurements. However, the method does require relatively high effective-SNR since the received data is broken

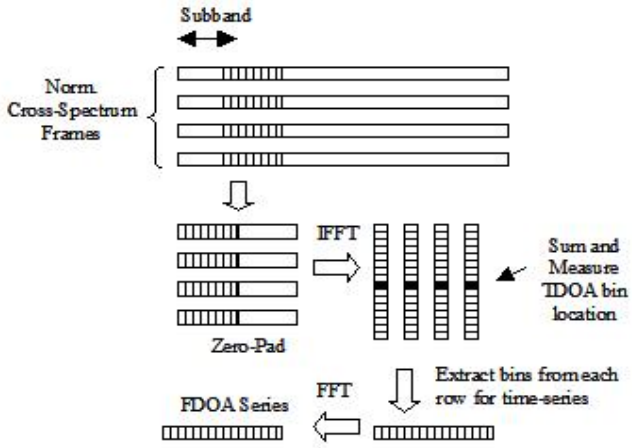

Figure 2.21: Diagram outlining the FDOA estimation processing using the *hybrid* method.

up into shorter segments, and spectrally overlapping signals will reduce the detection surface SNR by a factor equal to $(1/2)^{N_E-1}$, where N_E is the number of spectrally overlapping signals. Also, the examples in the next section will show that the *hybrid* method also produces biased estimates under severe CCI conditions. In the next section, processing examples using the *hybrid* method are presented.

2.4.1 Hybrid Method Examples

In the following examples the same SOI and SNOI generated for the CAF examples in Section 2.3.1 are used. Figure 2.22 displays plots of the normalized cross spectrum computed for two cases: 1) only the SOI is present in the received signal and 2) both the SOI and a SNOI are present. Notice that in the second case the SNOI represents CCI since there is spectral overlapping with the SOI.

The RF vs. TDOA surface was computed for the SOI only scenario by following the processing steps described in the last section. Both a 3-D view and a top view are displayed in Figure 2.23. It is easy to see from the surface plot that the SOI is at a

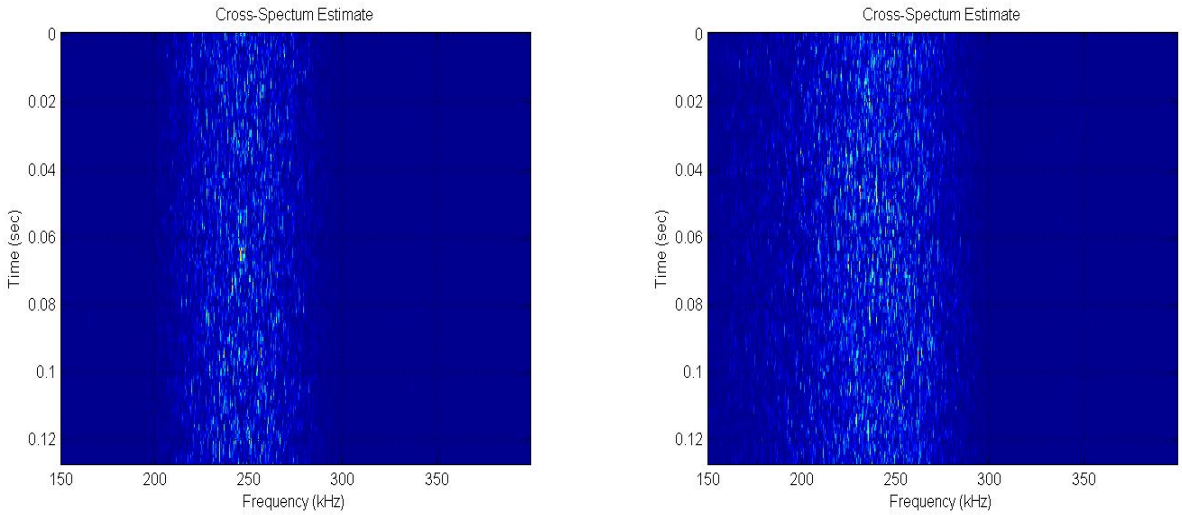

Figure 2.22: Cross spectrum magnitude vs. time representation for SOI used in *hybrid* method examples (Left). Cross spectrum vs. time representation for combined SOI and SNOI used in this section's *hybrid* method examples (Right).

center frequency of 246 kHz with a bandwidth of approximately 65 kHz. Figure 2.24 displays cross-section plots in the RF and TDOA dimensions and of the extracted time-series and corresponding FDOA estimate. In this example, the *hybrid* method estimates the TDOA of the SOI to be 64 microseconds and the FDOA to be -849.4 Hz. The true values for TDOA and FDOA are listed in Table 2.2 to be 70 microseconds and -850 Hz respectively.

For the next example, both the SOI and an SNOI are present at the receivers. Again, the RF vs. TDOA surfaces are computed, and TDOA and FDOA estimated for the SOI. The *hybrid* method is unable to estimate the SOI TDOA/FDOA parameters and is able only to estimate the SNOI TDOA/FDOA parameters. This makes sense given the fact that the SNOI has a wider bandwidth than the SOI and relatively small segments are used for each transformation in the *hybrid* method algorithm. This example demonstrates that the *hybrid* method suffers from the same limitations as the GCC and CAF methods.

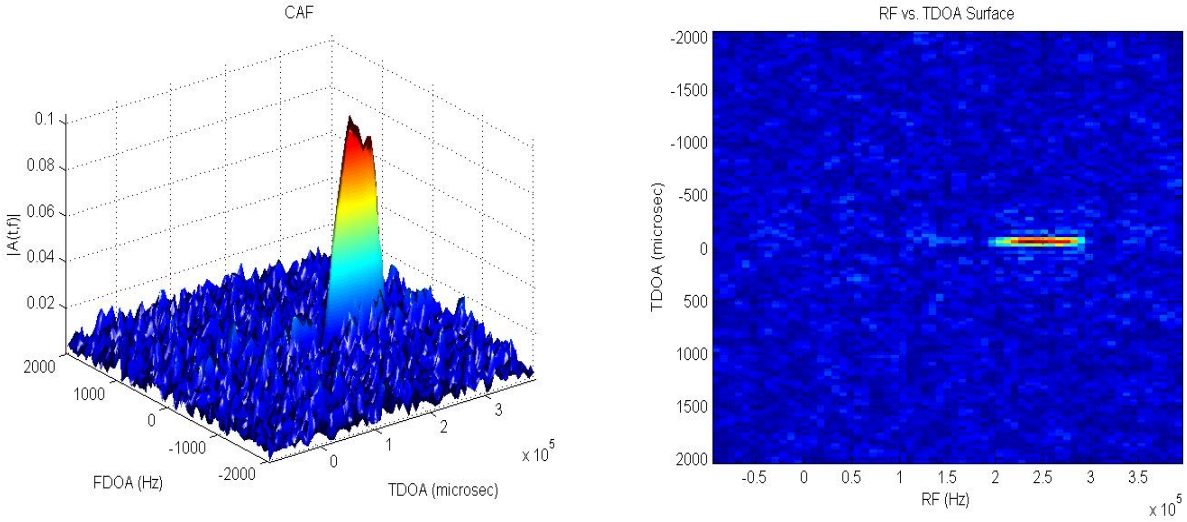

Figure 2.23: RF vs. TDOA surface compute using *hybrid* method from BPSK SOI collected at two spatially separated receivers with an SNR = 20 dB at both receivers. The data record length was 32,768 samples and the receiver samples rates were 1 MHz (Left). Top view of detection surface on the left (Right).

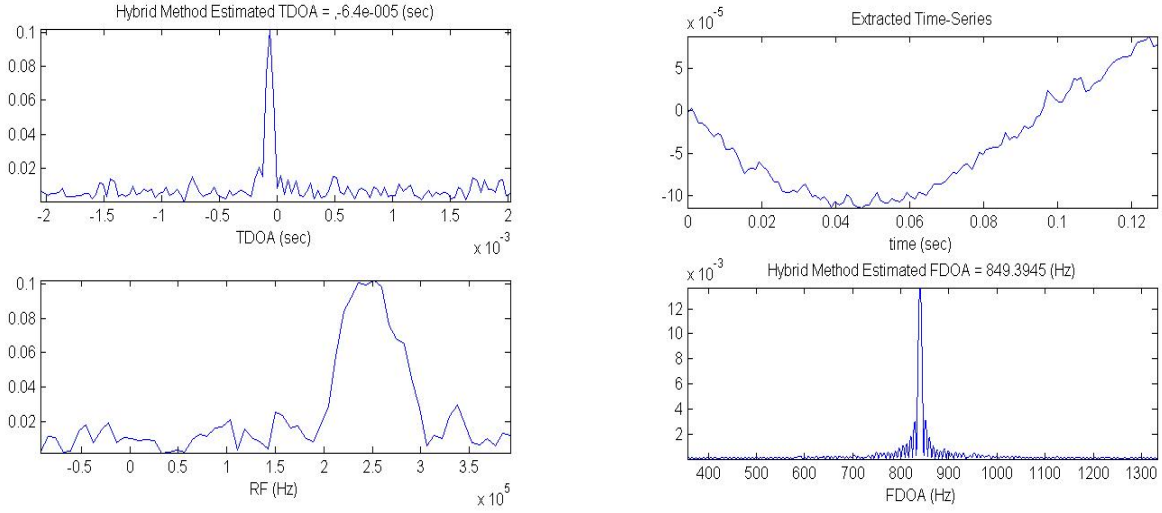

Figure 2.24: Cross-section plots through RF vs. TDOA surface in Figure 2.23 in both the RF and TDOA dimensions (Left). Extracted time-series and FDOA estimate (Right).

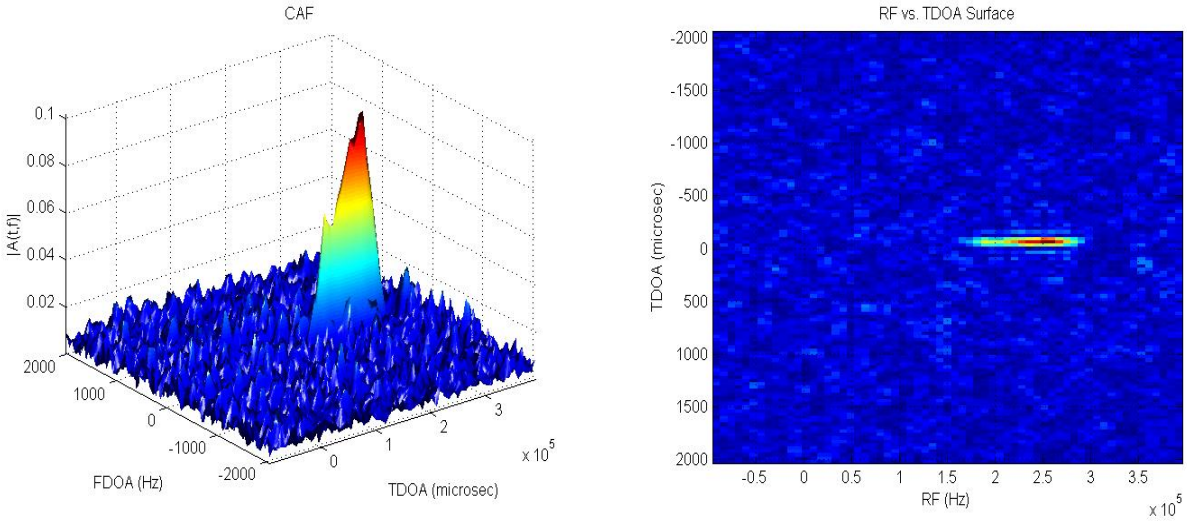

Figure 2.25: RF vs. TDOA surface compute using *hybrid* method from BPSK SOI and BPSK SNOI collected at two spatially separated receivers with an SIR = 0 dB at both receivers. The data record length was 32,768 samples and the receiver samples rates were 1 MHz (Left). Top view of detection surface on the left (Right)

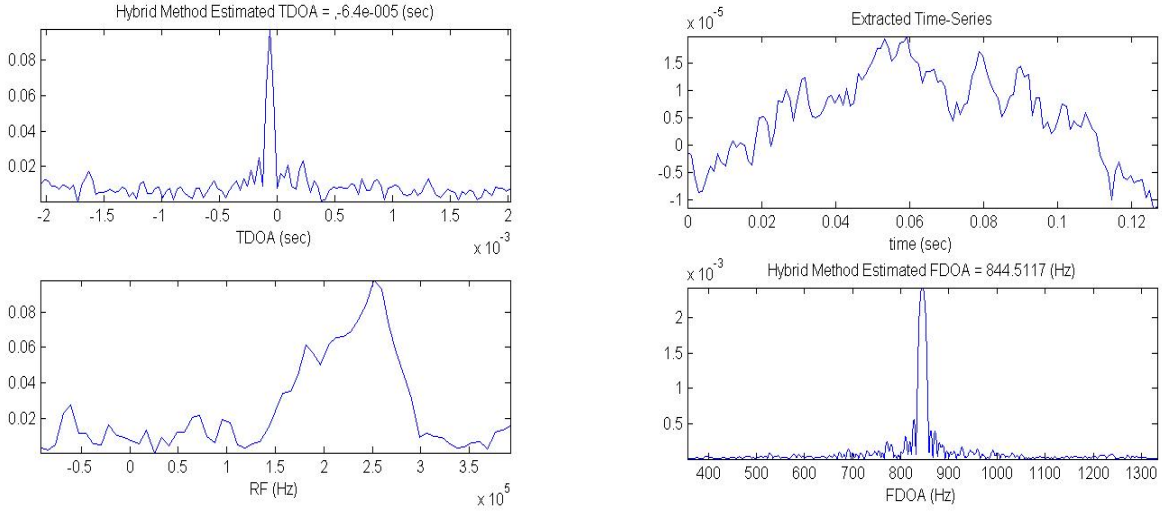

Figure 2.26: Cross-section plots through RF vs. TDOA surface in Figure 2.25 in both the RF and TDOA dimensions (Left). Extracted time-series and FDOA estimate (Right).

Chapter 3 – CYCLOSTATIONARY THEORY AND PROCESSING

3.1 Co-Channel Interference

Co-channel interference, or CCI, is interference between two or more radio transmissions that share the same frequency band. One of the main causes of CCI is overcrowding of the radio spectrum from multiple emitters using the same spectrum bandwidth at the same time.

In today's wireless communications systems, CCI impairs system capacity and link quality. For example, in *code-division multiple access* (CDMA) systems, all users or base stations are operating in the same frequency band, making CCI an inherent problem, often called *multiple access interference* (MAI). A multi-path channel can also introduce CCI in many modern digital communications systems [18]. For satellite systems, the asynchronism between transmitters can cause CCI [21]. Usually, designers try hard to suppress CCI in order to reduce the transmit power required to meet a specified signal-to-noise ratio, enabling more channels to be transmitted with lower power. In general, reducing CCI in communications systems leads to capacity increases. Hence, the design of interference-resistant receivers is important for multiuser communication systems. In terrestrial cellular systems, site planning and the use of antenna arrays at the base stations can be used to mitigate CCI. However, for airborne applications the receiver is usually subject to unavoidable CCI due to its high altitude and wide field of view. The number of signals within the airborne antenna footprint can be large, making it very difficult to make measurements for any one SOI. In the previous chapters it was demonstrated that the conventional methods for TDOA and FDOA estimation can fail,

or be unreliable when certain CCI conditions occur. This necessitates the use of new TDOA and FDOA estimation algorithms that are more robust to the effects of CCI.

3.2 Cyclostationary Signals

In this section, a signal property called *cyclostationarity* is introduced in both the time and frequency domains. In general, cyclostationary signals have periodically time-varying second order statistics. In other words, they have a periodic autocorrelation. This differs from the often assumed *stationary* signal, which has second order statistics that are constant with time. Many man-made digital communication signals are *cyclostationary* due to generation by some periodic process, such as modulation of a sinusoidal carrier, encoding, framing of data, etc [13].

Autocorrelation can be understood as a measure of how similar a signal is with a time-shifted version of itself. For a power signal $x(t)$ the definition of the autocorrelation of $x(t)$ (with the ergodic and stationary assumption) can be expressed in both the continous time and discrete sampled time by

$$R_x(\tau) = \lim_{T\to\infty} \frac{1}{T} \int_{-T/2}^{T/2} x(t)x^*(t-\tau)\,dt \tag{3.1}$$

$$R_x(l) = \lim_{N\to\infty} \frac{1}{N} \sum_{n=-N/2}^{N/2} x(n)x^*(n-l)\ . \tag{3.2}$$

The exact value of the autocorrelation will depend on the particular signal $x(t)$. However, as T becomes longer (3.1) will tend toward the value of the probabilistic definition

$$R_x(\tau) = E\left[x(t)x^*(t-\tau)\right]\ , \tag{3.3}$$

and to the equivalent infinite time-averaged definition [13]

$$R_x(\tau) = \lim_{T\to\infty} \frac{1}{T} \int_{-T/2}^{T/2} x\left(t + \frac{\tau}{2}\right) x^*\left(t - \frac{\tau}{2}\right)\, dt\ . \tag{3.4}$$

In order to be clear throughout this thesis, the infinite time-averaged (just called time-averaged from this point forward) definition will be used. It will be noted when probabilistic definitions are used.

The time-averaged mean of a signal is given by

$$\mu_x(t) = \lim_{T\to\infty} \frac{1}{T} \int_{-T/2}^{T/2} x(t)\, dt\ . \tag{3.5}$$

Of course, in practical applications only a finite sequence from the SOI is available. So, the calculated mean and autocorrelation will only be *estimates* of the true mean and true autocorrelation. However, if a sufficiently long sequence is available, then results can be obtained that closely approximate the true values.

As mentioned earlier, a stationary, or *wide-sense stationary* signal is one in which the mean value and autocorrelation are invariant with time. In contrast, a *wide-sense cyclostationary* signal has a stationary autocorrelation sequence that further has the property that the mean and the autocorrelation sequence are periodic with time. This can be expressed using the probabilistic properties as

$$\mu_x(t) = E\left[x(t)\right] = E\left[x(t + mT_0)\right] \tag{3.6}$$

$$R_x(\tau) = E\left[x(t)x^*(t-\tau)\right] = E\left[x(t + mT_0)x^*(t + mT_0 - \tau)\right] \tag{3.7}$$

where m is an integer and T_0 is some fundamental period of time. For digital communication signals T_0 is related to a carrier, chip, or symbol frequency [9, 13]. It is

worth noting that if the autocorrelation has more than one non-harmonically related fundamental period, then the signal is said to be *polycyclostationary* [13].

The exploitation of these periodicities is called *cyclostationary processing*. The theoretical framework behind cyclostationary processing was mostly developed by Gardner and his colleagues [9, 10, 11, 12, 13]. In order to build the mathematical foundation needed for Chapter 4, some cyclostationary processing techniques will be introduced in the next section.

3.3 Processing Cyclostationary Signals

A cyclostationary signal of order n will have additive sine wave components that give spectral lines after some nth order polynomial transformation (which are nonlinear operations) [12, 13]. For example, $x(t)$ is cyclostationary with cyclic frequency α if the Fourier transform of some delay product

$$y(t) = x(t)x(t - mT_0) \tag{3.8}$$

produces a spectral line at frequency $\alpha = 1/T_0$. This is an example of a second order transformation, $n = 2$, and just another way of saying that the autocorrelation is periodic in time with period T_0.

First order cyclostationarity is defined as the mean of a signal having periodicity with some period T_0. Since the mean is periodic, it can be represented using a Fourier series as

$$\mu_x = \sum_{r=-\infty}^{\infty} \mu_r \exp\left(\frac{j2\pi rt}{T_0}\right) \tag{3.9}$$

where

$$\mu_r = \frac{1}{T_0} \int_{-T_0/2}^{T_0/2} \mu_x \exp\left(\frac{-j2\pi rt}{T_0}\right) dt \ . \tag{3.10}$$

The expression in (3.10) is called the *time-averaged cyclic mean.*

As mentioned above, second order cyclostationarity is similarly defined as having an autocorrelation function that is periodic with some period T_0. This can be mathematically expressed by

$$R_x(\tau) = R_x(\tau + mT_0) \ . \tag{3.11}$$

Like the periodic mean, the periodic autocorrelation can also be expressed using a Fourier series by

$$R_x(\tau) = \sum_{r=-\infty}^{\infty} R_x^{\alpha}(\tau) \exp\left(\frac{j2\pi rt}{T_0}\right) \tag{3.12}$$

where the summation can be over all values of α and $R_x^{\alpha}(\tau)$ is defined to be

$$R_x^{\alpha}(\tau) = \lim_{T\to\infty} \frac{1}{T_0} \int_{-T_0/2}^{T_0/2} R_x(\tau) \exp(-j2\pi r\alpha t)\, dt \ . \tag{3.13}$$

Note that $R_x^{\alpha}(\tau)$ will be zero unless α is related to a fundamental periodicity of the autocorrelation — i.e., $\alpha = 1/T_0$. For example, if the symbol rate of a signal is $1/T_0$, then $R_x^{\alpha}(\tau)$ will be nonzero at values $\alpha = mT_0$, where m is an integer. Equation (3.13) is called the *time-averaged cyclic autocorrelation function.* The related frequency domain version is called the *spectral correlation density* (SCD) and is defined as the Fourier transform of the time-averaged cyclic autocorrelation function, or

$$S_x^{\alpha}(f) = \int_{-\infty}^{\infty} R_x^{\alpha}(\tau) \exp(-j2\pi f^{'}\tau)\, d\tau \ . \tag{3.14}$$

Transforming the autocorrelation function product into a symmetric delay product yields

$$y(t) = x\left(t + \frac{\tau}{2}\right) x^*\left(t - \frac{\tau}{2}\right) \tag{3.15}$$

which, can then be used to form the following time-averaged cyclic autocorrelation func-

tion that is commonly used in cyclostationary processing [13]

$$R_x^\alpha(\tau) = \lim_{T\to\infty} \frac{1}{T} \int_{-T/2}^{T/2} x\left(t+\frac{\tau}{2}\right) x^*\left(t-\frac{\tau}{2}\right) \exp(-j2\pi\alpha t)\, dt\ . \tag{3.16}$$

Likewise, the cyclic cross correlation function can be expressed as

$$R_{xy}^\alpha(\tau) = \lim_{T\to\infty} \frac{1}{T} \int_{-T/2}^{T/2} x\left(t+\frac{\tau}{2}\right) y^*\left(t-\frac{\tau}{2}\right) \exp(-j2\pi\alpha t)\, dt\ . \tag{3.17}$$

A useful interpretation of (3.17) is to view it as the common cross correlation of two functions $x(t)$ and $y(t)$ shifted up and down by a frequency $\alpha/2$. In other words, it is the correlation in the time domain between two functions separated in frequency by α. For digitally modulated signals, the cyclic frequencies are usually related to the baud rate and the carrier frequency. Spread spectrum signals may have additional cyclic frequencies present, such as a chip rate in direct sequence spread spectrum, or the hopping frequency in frequency hopping spread spectrum. For example, a rectangular pulse BPSK signal with a baud rate of $1/T_0$ and carrier frequency f_c has cyclic frequencies $\alpha = \pm 2f_c + m/T_0$ and $\alpha = m/T_0$ for integers m [11].

The discrete version of the time-averaged cyclic cross correlation function can be found in [9] to be

$$R_{xy}^\alpha(kT_s) = \lim_{N\to\infty} \frac{1}{2N+1} \sum_{n=-N}^{N} x(nT_s + kT_s) y^*(nT_s) \exp(-j2\pi\alpha(n+k/2)T_s)\ . \tag{3.18}$$

As mentioned earlier, the Fourier transform of the cyclic correlation function is the *spectral correlation density* (SCD). In continuous time the SCD has the form

$$S_x^\alpha(f) = \int_{-\infty}^{\infty} R_x^\alpha(\tau) \exp(-j2\pi f\tau)\, d\tau\ . \tag{3.19}$$

Notice that the SCD reduces to the conventional *power spectral density* (PSD) when $\alpha = 0$. The SCD at frequency f_0 and cyclic frequency α is merely the correlation of two values of the signal in the frequency domain separated in frequency by α and centered at frequency f_0. Likewise, the SCD computed from the cyclic cross correlation becomes

$$S_{xy}^{\alpha}(f) = \int_{-\infty}^{\infty} R_{xy}^{\alpha}(\tau) \exp(-j2\pi f\tau)\, d\tau \ . \tag{3.20}$$

The cyclic correlation function and the spectral correlation density are Fourier transform pairs for cyclostationary signals, analogous to the correlation and power spectral density pairs for stationary signals. An important feature of the second order cyclostationary statistics is that they contain the phase information about the original signal. This fact is important when using the *alpha*CAF algorithm in the next chapter for estimating TDOA and FDOA.

To illustrate some properties of cyclostationary signals, Figures 3.1 and 3.2 show plots of the complex SCD magnitude for some common simulated signals including a BPSK signal similar to the one used for the SOI in chapters of this thesis. Since finite sequences of the signals were used, resulting in a truncated time-averaged approach, some estimation artifacts are apparent in the SCD plots.

Figure 3.1 shows the SCD computed for a sine wave with a frequency $f_c = 100$ kHz. It is easy to see that when $\alpha = 0$ the normal power spectral density of a sine wave, which consists of two impulses at $\pm f_c$, is produced. The other two peaks correspond to correlations after frequency shifting the sine functions until the impulses originally at $\pm f_0$ are again lined up. This requires a frequency shift of $2f_c$. This is a trivial example of the carrier frequency related correlation that appears with many cyclostationary signals.

Another example of a SCD plot is shown in Figure 3.2. The signal used was a rectangular pulse BPSK waveform, modulated with pseudo-random data, a symbol rate

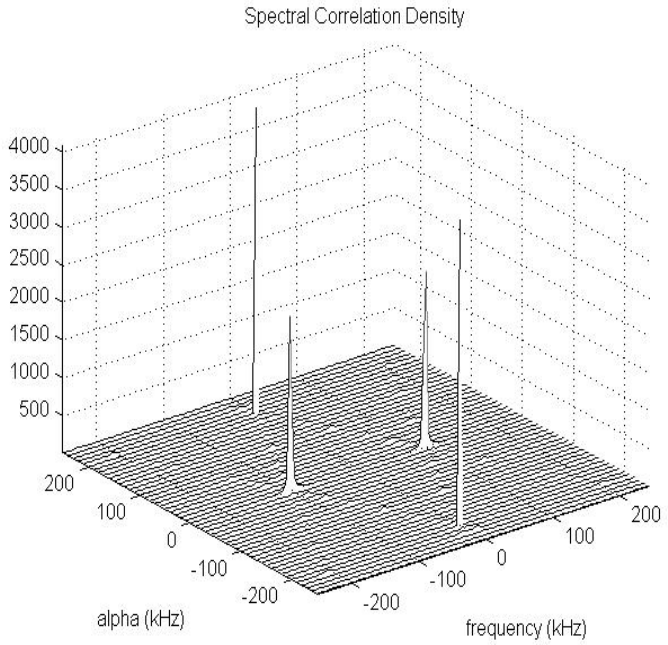

Figure 3.1: SCD computed for a sine wave with frequency 100 kHz.

of 10 kHz, and a carrier frequency of 100 kHz. Again, when $\alpha = 0$, the spectrum in the frequency dimension is equivalent to the stationary BPSK power spectral density. For $\alpha \neq 0$ the plot represents the cross-spectral density of the signal with a frequency shifted version of itself. Correlations exist at frequency shifts that are equal to integer multiples of the symbol rate, $\pm m1/T_0$. As expected, the largest correlation exists when the shift is equal to twice the carrier frequency. Examples of the SCD magnitude for several other communications signals can be found in [11]. It should be clear by now that the SCD can be used for signal modulation type identification due to the ability to form unique signatures for different signal types and pulse shapes.

Similar to the GCC method in Chapter 2, the normalized cross spectral density using the cyclic versions of the autocorrelation and cross correlation functions can be formed. For example, the normalized cyclic cross spectral density can be expressed as

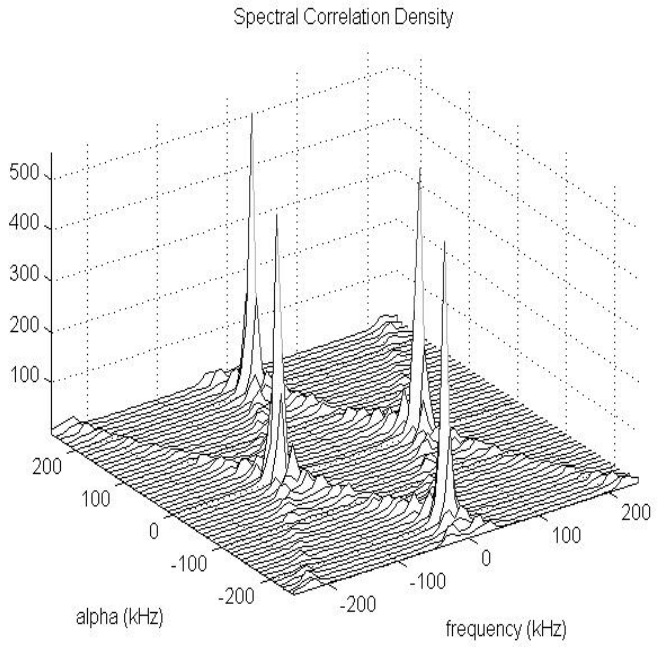

Figure 3.2: SCD computed for a BPSK signal with center frequency of 100 kHz and symbol rate of 10 kHz.

$$C_{xy}^{\alpha}(f) = \frac{S_{xy}^{\alpha}(f)}{\sqrt{S_x^{\alpha}(f) S_y^{\alpha}(f)}} \,. \tag{3.21}$$

This is often called the *spectral cross coherence function* [12]. Several methods in the literature that exploit cyclostationarity for TDOA estimation are based around use of the spectral cross-coherence function [9, 10]. In the next section one of these methods will be introduced, and examples presented on how it is used to obtain TDOA measurements.

3.4 Exploiting Cyclostationarity for TDOA Estimation

Estimating the TDOA for a man-made signal is one of the many applications for cyclostationary processing, and several good papers in the literature deal with this topic

[9, 10, 12]. Key to the capability to develop TDOA estimation algorithms using cyclostationary techniques is the fact that the cyclic correlation functions retain phase information about the signals. Therefore, it is possible to exploit phase differences between signals received at two locations. The signal selectivity that can be achieved by exploiting cyclostationarity results in algorithms with greater tolerance to additive noise and interfering signals that overlap temporally, spectrally, and spatially.

Most all of the successful cyclostationary TDOA estimation algorithms are based around computation of the *frequency-smoothed spectral correlation density* [9]. The frequency-smoothed SCD can be computed using

$$\hat{S}^{\alpha}_{x_{\Delta f}} = \frac{1}{M} \sum_{v=-(M-1)/2}^{(M-1)/2} \frac{1}{\Delta t} \bar{X}_{\Delta t}\left(t, f + \frac{\alpha}{2} + vF_s\right) \bar{X}^{*}_{\Delta t}\left(t, f - \frac{\alpha}{2} + vF_s\right) \tag{3.22}$$

where

$$\bar{X}_{\Delta t}(t, f) = \sum_{k=0}^{N-1} x\left(t - kT_s\right) \exp\left(-j2\pi f(t - kT_s)\right) \ . \tag{3.23}$$

Equation (3.22) will be used when computing the spectral correlation densities used in the TDOA estimation algorithms in order to arrive at stable estimates [13].

Using the signal model in (2.1) and (2.2) where $s(t)$ is a SOI that exhibits cyclostationarity and D replaces τ as the TDOA, the cyclic correlation functions are computed to be

$$R^{\alpha}_{x}(\tau) = R^{\alpha}_{s}(\tau) \tag{3.24}$$

$$R^{\alpha}_{y}(\tau) = R^{\alpha}_{s}(\tau) \exp(-j2\pi\alpha D) \tag{3.25}$$

$$R^{\alpha}_{yx}(\tau) = R^{\alpha}_{s}(\tau - D) \exp(-j\pi\alpha D) \tag{3.26}$$

where the noise auto and cross terms have been dropped due to the assumption that the noise terms are not cyclostationary and their cyclic correlations will be zero for $\alpha \neq 0$.

Following the form of the GCC method in (2.18) a function can be formed using the spectral correlation functions called the *spectral correlation ratio*, or SPECCOR, function [9, 10], that is defined as

$$b_\alpha(\tau) \triangleq \left| \int_{(f_\alpha - B_s/2)}^{(f_\alpha + B_s/2)} \frac{S_{yx}^\alpha(f)}{S_x^\alpha(f)} \exp(j2\pi ft)\, df \right| \tag{3.27}$$

where B_s is the signal spectrum bandwidth and α is a signal cyclic frequency. This function is considered ideal when dealing with complex data [10]. Notice that (3.27) is similar in form to the GCC method when using a ROTH weighting function. However, with the SPECCOR function the cyclic spectrums are used instead of the conventional signal spectrums. As with the GCC method, other weighting functions can be used in (3.27) and another common definition is

$$b_\alpha(\tau) \triangleq \left| \int_{(f_\alpha - B_s/2)}^{(f_\alpha + B_s/2)} \frac{S_{yx}^\alpha(f)}{\sqrt{S_x^\alpha(f) S_y^\alpha(f)}} \exp(j2\pi ft)\, df \right| , \tag{3.28}$$

which is sometimes called the *cyclic spectral coherence* [12]. Notice that (3.28) is similar to the GCC method using a SCOT weighting function. Using the cyclic correlation functions in (3.24)–(3.26) the maximum of (3.27) or (3.28)

$$max\{b_\alpha(\tau)\} = D \tag{3.29}$$

will be a peak at D, and will correspond to the estimated TDOA.

It was introduced in [9] that there are better functions than (3.27) for estimating the TDOA of cyclostationary signals. Probably the most widely accepted method is called *spectral coherence alignment*, or SPECCOA [9, 13]. The SPECCOA function is defined

as

$$c_\alpha(\tau) \triangleq \left| \int R_{yx}^{\alpha}(\tau) R_x^{\alpha}(\tau - D)^* \, d\tau \right| . \tag{3.30}$$

3.4.1 Signal Selective TDOA Estimation Examples

Now some examples will be shown from using the SPECCOA method to estimate TDOA for a cyclostationary signal. Figures 3.3 and 3.4 show plots of the SPECCOA output computed using the simulated SOI and SNOI signals outlined in Table 2.2 and the collection geometry in Figure 2.2. The left plot in Figure 3.3 is an example where only the SOI is present in a AWGN environment with a SNR at both receivers of 3 dB. The TDOA can be measured from the peak in the plot to be 69 microseconds, which correlates well to the true value of 70 microseconds considering no interpolation is used. It should be noted that like the GCC method, in the absence of interpolating, the spacing between samples in the SPECCOA output is determined by the receiver sample rate and any zero-padding used before the output transformation. The right plot in Figure 3.3 is from an example where only the SNOI is present in a AWGN environment with an SNR of 3 dB. Again, the TDOA is measured from the peak to be 63 microseconds, which correlates well to the true value of 63.3 microseconds.

As another example, Figure 3.4 illustrates a scenario where both the SOI and SNOI are present in a AWGN environment and an SIR of 0dB at both receivers. Their respective emitters are located 1 km apart. The left plot shows the output computed for a cyclic frequency, or α, equal to the symbol rate of the SOI. The right plot shows the output computed for α equal to the symbol rate of the SNOI. In both cases a separate TDOA estimation can be made regardless of the close location of the other emitter transmitting a spectrally overlapping signal. It is clear that the SPECCOA method is able to separate the SOI from the SNOI for TDOA estimation by exploiting cyclosta-

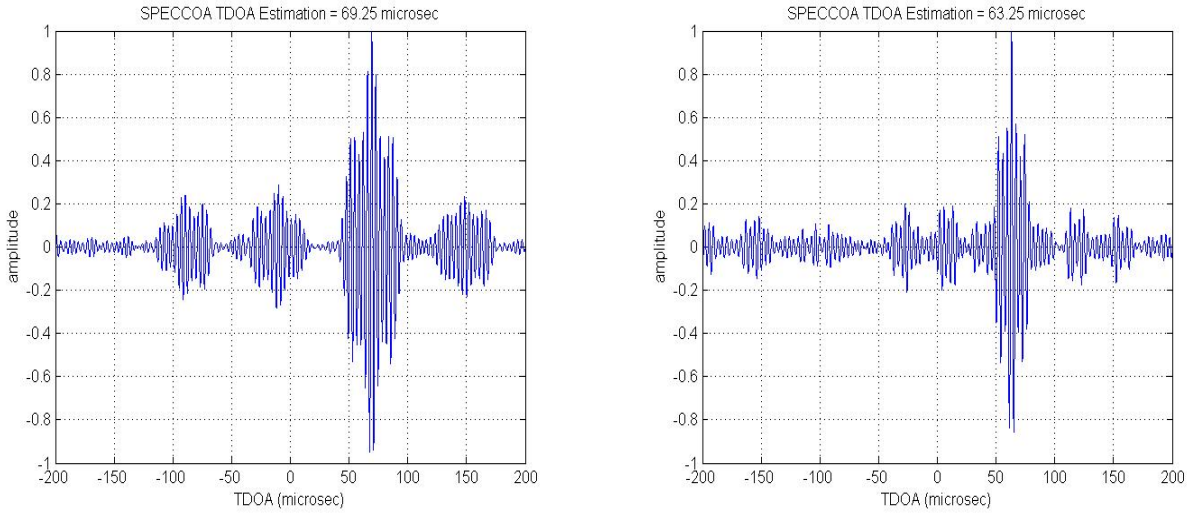

Figure 3.3: SPECCOA output for SOI only with SNR = 3dB. The cyclic frequency is fixed at the symbol rate of the SOI. The peak corresponds to the estimated TDOA (Left). SPECCOA output for SNOI only with SNR = 3dB. The cyclic frequency is fixed at the symbol rate of the SNOI. The peak corresponds to the estimated TDOA (Right).

tionarity. This is an improvement over the conventional GCC method that produced biased estimations under the same scenario.

The previous examples demonstrate that by exploiting cyclostationarity it is possible to achieve better estimation capabilities for emitter location applications when severe CCI can cause conventional methods to fail or be unreliable. In the next Chapter, it will be shown how it is possible to *jointly* estimate TDOA and FDOA using cyclostationary techniques.

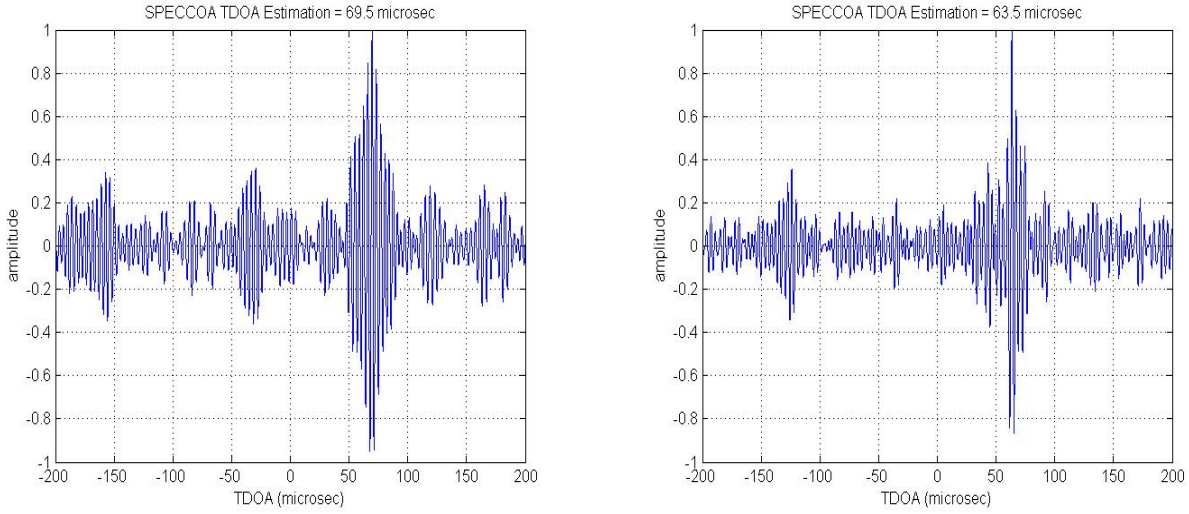

Figure 3.4: SPECCOA output for SOI and SNOI from emitters located 1 km apart and SIR = 0 dB. The cyclic frequency is fixed at the SOI symbol rate. The peak corresponds to the TDOA estimate for the SOI while the SNOI has been suppressed (Left). SPECCOA output for SOI and SNOI with SIR = 0 dB. The cyclic frequency is fixed at the SNOI symbol rate. The peak corresponds to the TDOA estimate for the SNOI while the SOI has been suppressed (Right).

Chapter 4 – SIGNAL SELECTIVE JOINT TDOA AND FDOA ESTIMATION

4.1 A New Correlation Function

This chapter begins with the development of a new correlation function that exploits cyclostationarity for joint TDOA and FDOA estimation. The derivation of this new function will use the same signal model used in the derivations for the CAF method. This model is expressed again here as

$$x(t) = s(t) + n_x(t) \tag{4.1}$$

$$y(t) = A_r s(t - D)\exp(j2\pi f_d t) + n_y(t)\ . \tag{4.2}$$

Recall from the last chapter that the CAF can be expressed as

$$A(\tau, f) = \int_0^T y(t)x^*(t + \tau)\exp(-j2\pi f t)\, dt\ . \tag{4.3}$$

Notice that (4.3) is a correlation function over two parameters, τ and f. If the received signals are assumed to be cyclostationary, then (4.3) can be modified to be a correlation function over three parameters, τ, f and α. This will allow signals to be separated using cyclic frequency for estimating their kinematic parameters. After forming a symmetrical delay product for each cyclostationary signal, a new correlation function can be written

as

$$A^{\gamma}(D,f) = \int_0^T \left[\int_{-T/2}^{T/2} y(t+\tau/2)x^*(t-\tau/2)\exp(-j2\pi\gamma t)\,dt \right] \left[\int_{-T/2}^{T/2} x(t+\tau/2+D/2)x^*(t-\tau/2-D/2)\exp(-j2\pi\alpha t)\,dt \right]^* \exp(-j2\pi f\tau)\,d\tau \tag{4.4}$$

where $\gamma = \alpha - f$ is a modified cyclic frequency adjusted for possible Doppler shift on signal y (see signal model). The notation for (4.4) can be simplified using the cyclic correlation function definitions to yield

$$A^{\gamma}(D,f) = \int_0^T R_{yx}^{\gamma}(\tau) R_x^{\alpha}(\tau - D)^* \exp(-j2\pi f\tau)\,d\tau\ , \tag{4.5}$$

which is the definition of the new *alpha cross ambiguity function*, or *alpha*CAF. The regular and modified cyclic frequency forms for the time-averaged cyclic correlation functions can be written as

$$R_x^{\alpha}(\tau) = \lim_{T\to\infty} \frac{1}{T} \int_{-T/2}^{T/2} x(t+\tau/2)x^*(t-\tau/2)\exp(-j2\pi\alpha t)\,dt \tag{4.6}$$

$$R_y^{\gamma}(\tau) = \lim_{T\to\infty} \frac{1}{T} \int_{-T/2}^{T/2} y(t+\tau/2)y^*(t-\tau/2)\exp(-j2\pi\gamma t)\,dt \tag{4.7}$$

$$R_{yx}^{\gamma}(\tau) = \lim_{T\to\infty} \frac{1}{T} \int_{-T/2}^{T/2} y(t+\tau/2)x^*(t-\tau/2)\exp(-j2\pi\gamma t)\,dt\ . \tag{4.8}$$

Using the signal model in (4.1) and (4.2), (4.6)–(4.8) can be expanded to be

$$R_x^{\alpha}(\tau) = R_s^{\alpha}(\tau) \tag{4.9}$$

$$R_y^{\gamma}(\tau) = |A|^2 R_s^{\gamma+2f_d}(\tau)\exp(-j2\pi(\gamma+2f_d)D) \tag{4.10}$$

$$R_{yx}^{\gamma}(\tau) = A R_s^{\gamma+f_d}(\tau - D)\exp(-j2\pi(\gamma+f_d)D)\exp(-j\pi f_d\tau)\ . \tag{4.11}$$

Equation (4.9) will be a maximum when $\alpha = 0$ or a signal's cyclic frequency, and when

$\tau = 0$. Likewise, (4.10) will be a maximum when $\gamma = -2f_d$ and $\tau = 0$, and (4.11) will be a maximum when $\gamma = -2f_d$, $\gamma = \alpha - 2f_d$ and $\tau = D$. This can be taken further using the fact that $\gamma = \alpha - f$ and deduce that (4.11) will be a maximum when $f = f_d$, $f = 2f_d$, and $f = 2f_d - \alpha$.

If (4.11) is used with (4.5) the new correlation function in (4.5) can be written to be

$$A^{\gamma}(\tau, f) = A \int_0^T R_s^{\gamma+f_d}(\tau - D) R_s^{\alpha}(\tau) \exp(-j\pi(\gamma + f_d)D) \exp(-j\pi(f_d - f)\tau)\, d\tau \ . \quad (4.12)$$

When α is at a signal's cyclic frequency, (4.12) is maximum when $\tau = D$ and $f = f_d$. Notice that it is a correlation of a cyclic cross correlation sequence with a frequency shifted cyclic autocorrelation sequence. Also, notice that (4.5) is similar in form to the SPECCOA function introduced in Section 3.4. However, (4.5) is a function of two dimensions for a fixed α, but the SPECCOA function is only a function of one dimension for a fixed α.

Since it is sometimes easier to work with the SCD instead of the cyclic correlation functions, it is useful to create a frequency domain version of (4.5). The spectral correlation functions can be found by taking the Fourier transform of the cyclic correlation functions as follows

$$S_x^{\alpha}(f') = \int_{-\infty}^{\infty} R_x^{\alpha}(\tau) \exp(-j2\pi f'\tau)\, d\tau \quad (4.13)$$

$$S_y^{\gamma}(f') = \int_{-\infty}^{\infty} R_y^{\gamma}(\tau) \exp(-j2\pi f'\tau)\, d\tau \quad (4.14)$$

$$S_{yx}^{\gamma}(f') = \int_{-\infty}^{\infty} R_{yx}^{\gamma}(\tau) \exp(-j2\pi f'\tau)\, d\tau \quad (4.15)$$

giving

$$S_x^{\alpha}(f') = S_s^{\alpha}(f') \tag{4.16}$$

$$S_y^{\gamma}(f') = |A|^2 S_s^{\gamma+2f_d}(f') \exp(-j2\pi(\gamma+2f_d)D) \tag{4.17}$$

$$S_{yx}^{\gamma}(f') = A S_s^{\gamma+f_d}(f'+f_d/2) \exp(-j2\pi(\gamma+f_d)D) \exp(-j\pi D f') \; . \tag{4.18}$$

Now (4.5) can be expressed in the frequency domain using (4.17)–(4.19). The frequency domain version of *alpha*CAF becomes

$$W^{\gamma}(D,f) = A \int_0^T S_{yx}^{\gamma}(f') S_x^{\alpha}(f'+f/2) \exp(-j2\pi\tau(f'+\alpha/2))\, df' \; . \tag{4.19}$$

It follows from (4.17) and (4.19) that $W^{\gamma}(\tau, f)$ can be expanded to be

$$W^{\gamma}(D,f) = A \int_0^T S_s^{\gamma+f_d}(f'+f_d/2) S_s^{\alpha}(f') \exp(-j2\pi(\gamma+f_d)D) \exp(-j2\pi\tau(f'+\alpha/2))\, df' \tag{4.20}$$

and will be maximum when $f = f_d$ and $\tau = D$ and α is equal to a signal's cyclic frequency. This is exactly the type of correlation function needed to overcome the problems encountered with the conventional methods introduced in Chapter 2.

For both the time domain *alpha*CAF in (4.5) and frequency domain *alpha*CAF in (4.19), frequency-smoothing and time-averaging can be used when forming the cyclic correlation functions and/or spectral correlation functions. However, frequency-smoothing has a low-pass filtering effect and can decrease the amplitude of the *alpha*CAF output at large TDOA values.

The *alpha*CAF equation in (4.5) provides a two dimensional output for each cyclic frequency chosen for the computation. However, computing the output for many cyclic frequencies comes with the a high computational cost. Clearly, the *alpha*CAF function

is best suited for applications where the cyclic frequencies of interest are known *a priori*. In Chapter 5 the actual benefits of using (4.5) over the conventional CAF method will be illustrated.

4.1.1 *alpha*CAF Examples

In this section of the thesis, some examples from the new *alpha*CAF correlation function developed in Section 4.1 are given. All of the figures for this section are located at the end of this section. The first example uses the SOI from Table 2.2 and no interference. The SNR at both receivers is 5 dB. The collection geometry is once again the same as that depicted in Figure 2.2. The collection length is 2048 microseconds long, or 2048 samples at a 1 MHz sample rate. Figure 4.1 displays an *alpha*CAF surface generated using the magnitude output from (4.5). Both the 3-D view and the 2-D top view are provided for comparison with the examples in Chapter 2. Just like the conventional CAF, the *alpha*CAF generates a peak at the estimated TDOA and FDOA values. The peak correlates well to the predicted TDOA (70 microseconds) and the predicted FDOA (850 Hz) values. Figure 4.2 shows the cross-section plots through the SOI peak in both the TDOA and FDOA dimensions.

The next example uses only the SNOI from Table 2.2 with no SOI present. The SNR at both receivers is 5 dB. Figure 4.3 displays the *alpha*CAF surface computed using the magnitude output from (4.5). Again, both the 3-D view and the top view are provided. A peak is clearly visible at the predicted SNOI TDOA (63.3 microseconds) and predicted FDOA (845 Hz) values. The values are easier to see in the cross-section plots in Figure 4.4.

The next example uses both the SOI and SNOI from Table 2.2 with an SIR of 0 dB at both receivers. The SOI and SNOI emitters are 1 km apart. Figure 4.5 displays the

*alpha*CAF surface computed with the cyclic frequency fixed at the symbol rate of the SOI ($16/256f_s$). The receiver sample rates are 1 MHz. Both the 3-D view and the top view are provided, with the cross-section plots displayed in Figure 4.6. A single peak is clearly visible at the predicted TDOA and FDOA values for the SOI even though the SNOI overlaps with it spectrally and spatially. Unlike the conventional CAF, the *alpha*CAF has separated the peak for the SOI from the peak for the SNOI by exploiting their different symbol rates.

Figure 4.7 displays an *alpha*CAF surface computed with the cyclic frequency fixed at the symbol rate of the SNOI ($26/256f_s$). In this case the peak for the SNOI has been separated from the peak for the SOI. Using the *alpha*CAF method a unique detection surface can be generated for any unique cyclic frequency. If it was computed over many cyclic frequencies, a three-dimensional detection cube could be formed for estimating TDOA, FDOA, and cyclic frequency. Figure 4.8 displays cross-section plots through the SNOI peak in Figure 4.7 in both the TDOA and FDOA dimensions.

In order to provide an even more obvious illustration of the separation capability of the *alpha*CAF, Figures 4.9–4.11 show surface plot top views from a CAF computation together with an *alpha*CAF computation using a co-channel scenario. In this example the SOI and SNOI emitters are separated spatially by a large distance so that their respective TDOAs and FDOAs are clearly resolvable in the conventional CAF surface. Figure 4.9 shows the conventional CAF output while Figure 4.10 and 4.11 show the *alpha*CAF output with the cyclic frequency fixed at the symbol rate for the SOI and SNOI respectively. This clearly demonstrates that the *alpha*CAF method can separate the signals according to their unique cyclic frequencies.

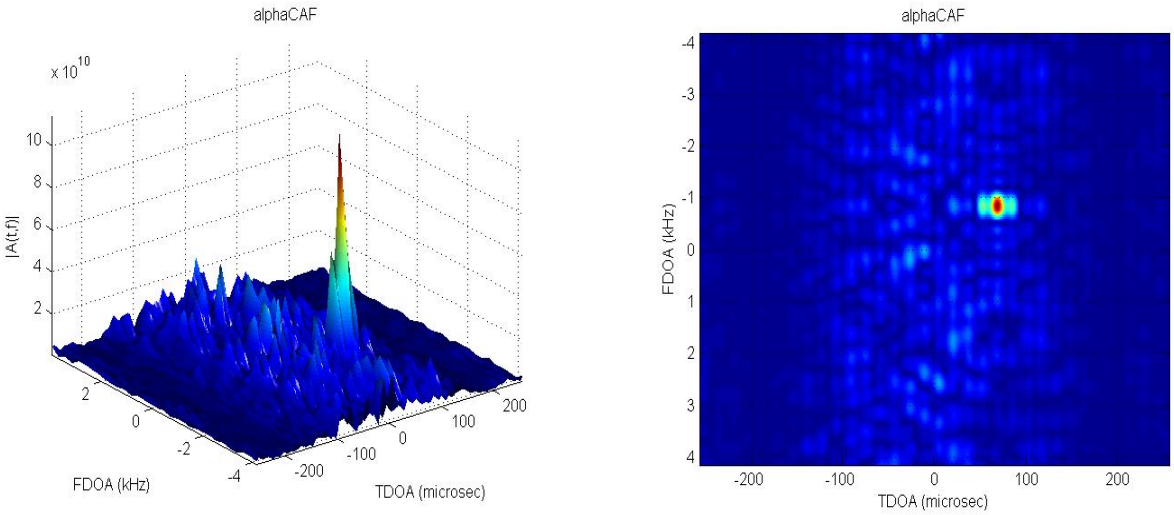

Figure 4.1: *alpha*CAF surface computed from SOI only with SNR = 5 dB. Cyclic frequency was fixed at the SOI symbol rate ($16/256 f_s$). The data record length is 2048 samples with a sample rate of 1 MHz (Left). Top view of surface to the left showing peak location corresponding to TDOA and FDOA estimate (Right).

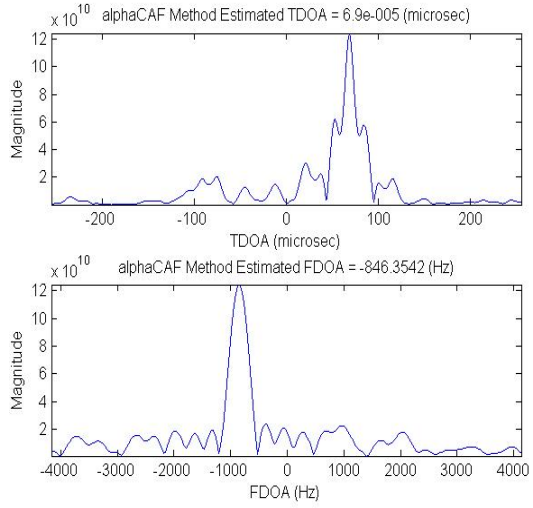

Figure 4.2: Cross-section plots through surface in Figure 4.1 in both the TDOA and FDOA dimensions.

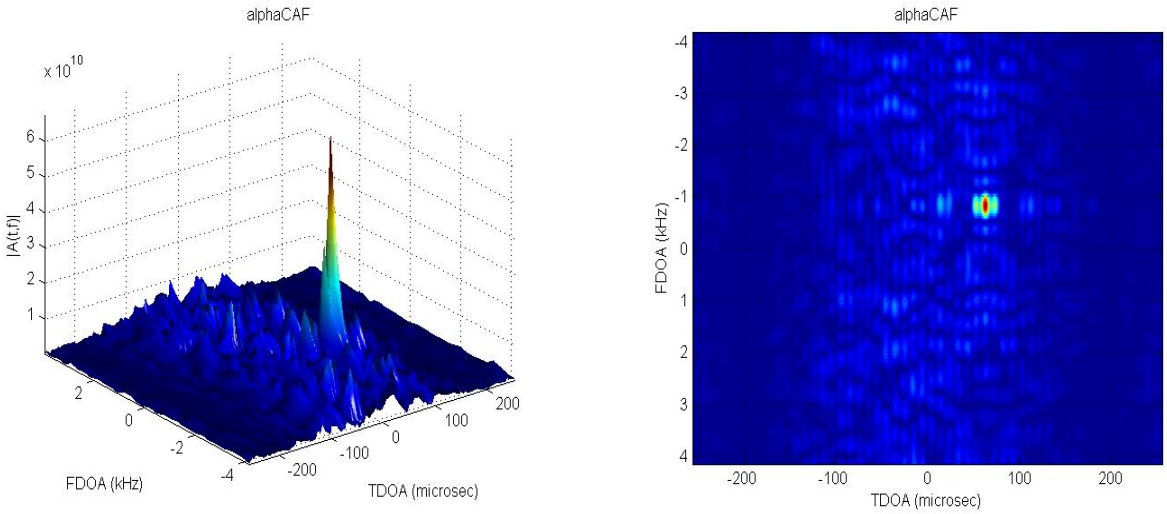

Figure 4.3: *alpha*CAF surface computed from SNOI only with SNR = 5 dB. Cyclic frequency was fixed at the SOI symbol rate ($26/256f_s$). The data record length is 2048 samples with a sample rate of 1 MHz (Left). Top view of surface to the left (Right).

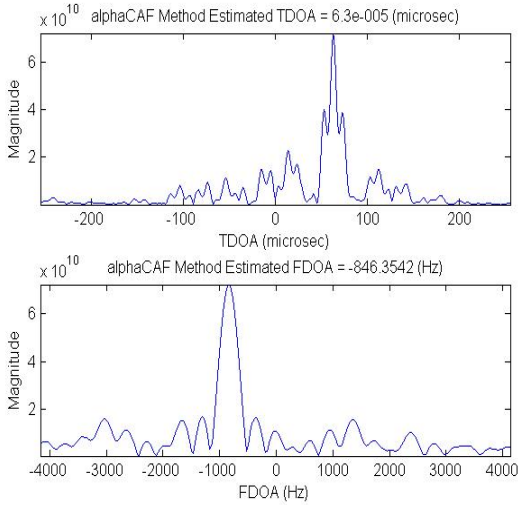

Figure 4.4: Cross-section plots through surface in Figure 4.3 in both the TDOA and FDOA dimensions.

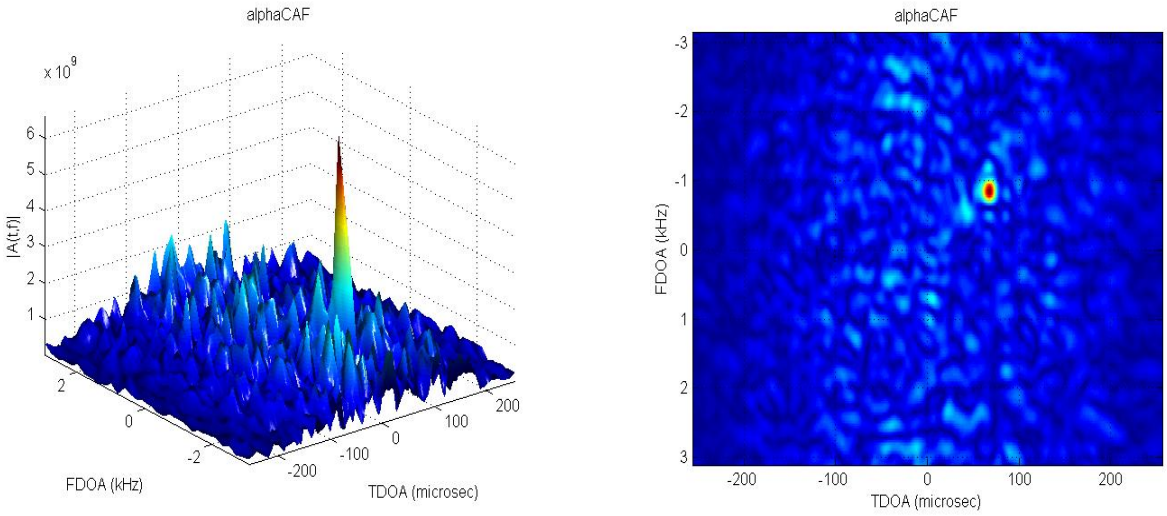

Figure 4.5: *alpha*CAF surface computed from SOI and SNOI with the cyclic freqeuncy fixed at the SOI symbol rate in order to separate the SOI estimate. The SIR = 0 dB for both receivers. The data record length was 2048 samples with a sample rate of 1 MHz (Left). Top view of surface to the left (Right).

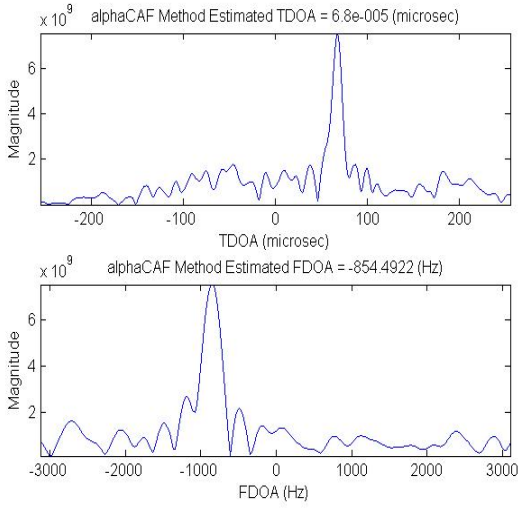

Figure 4.6: Cross-section plots through surface in Figure 4.5 in both the TDOA and FDOA dimensions.

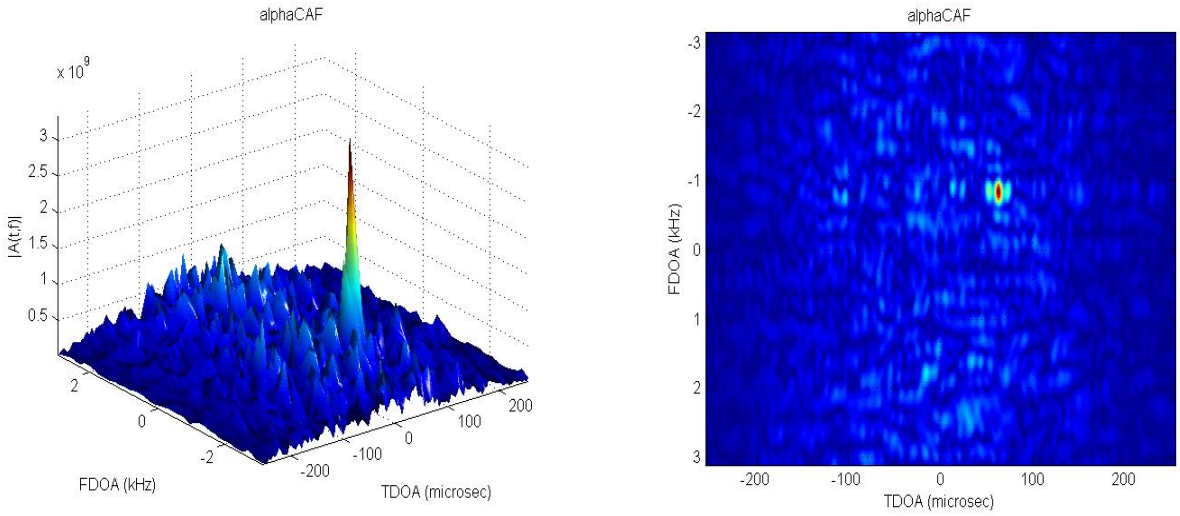

Figure 4.7: *alpha*CAF surface computed from SOI and SNOI with the cyclic freqeuncy fixed at the SNOI symbol rate in order to separate the SNOI estimate. The SIR = 0 dB for both receivers. The data record length was 2048 samples with a sample rate of 1 MHz (Left). Top view of surface to the left (Right).

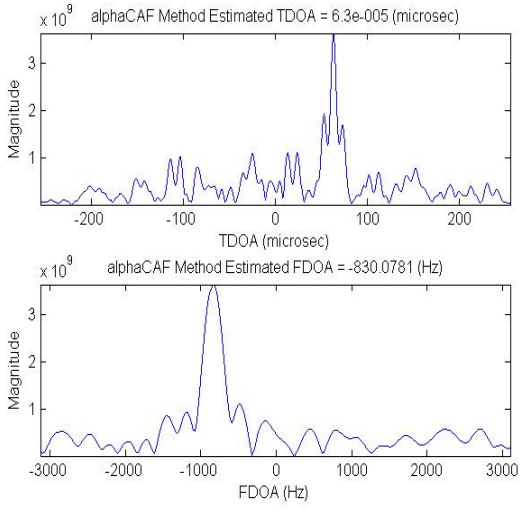

Figure 4.8: Cross-section plots through surface in Figure 4.7 in both the TDOA and FDOA dimensions.

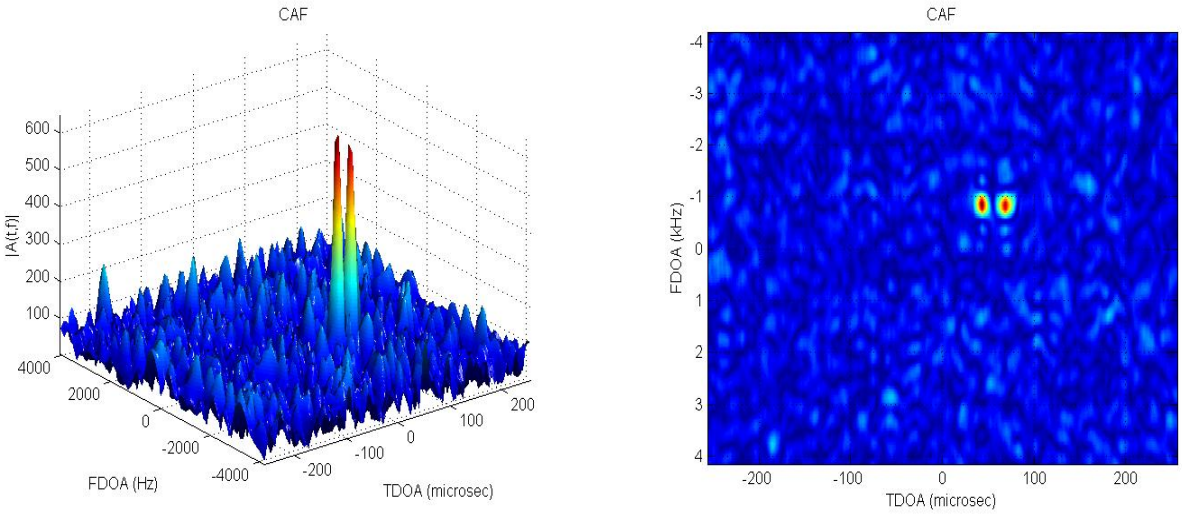

Figure 4.9: Conventional CAF output computed for spatially separated SOI and SNOI. The SIR = 0 dB for both receivers. The data record length is 2048 samples with a sample rate of 1 MHz (Left). Top view of surface on the left (Right).

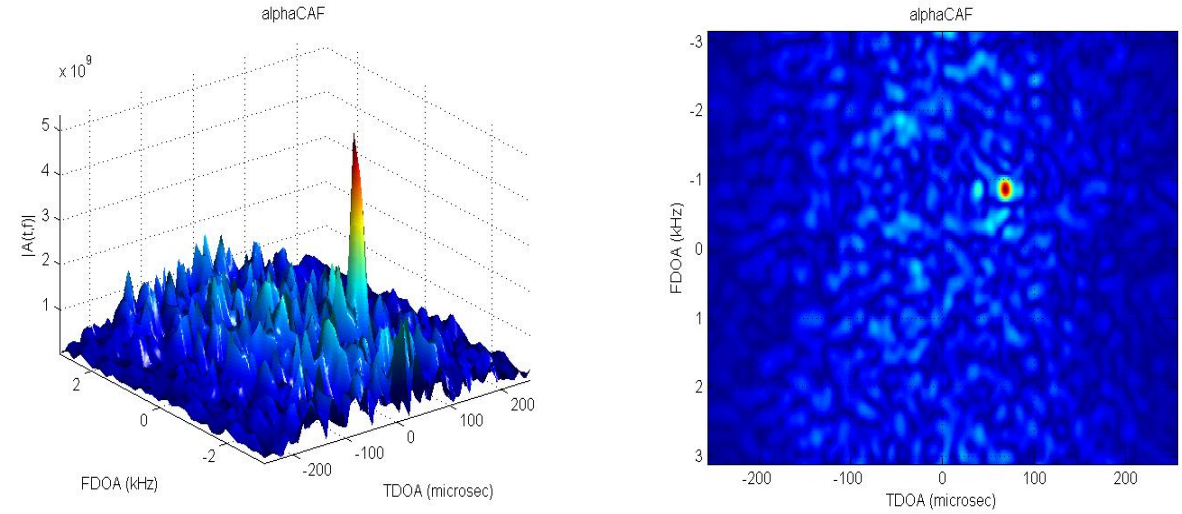

Figure 4.10: *alpha*CAF output computed for spatially separated SOI and SNOI. The SIR = 0 dB for both receivers. The cyclic frequency was fixed at the SOI symbol rate in order to separate the SOI estimate. The data record length is 2048 samples with a sample rate of 1 MHz (Left). Top view of surface on the left (Right).

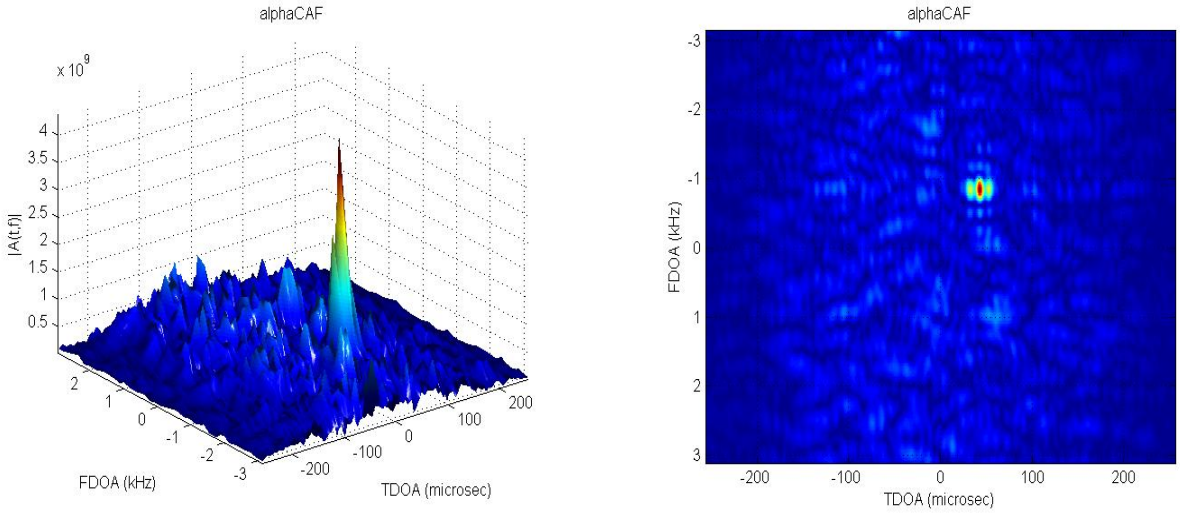

Figure 4.11: *alpha*CAF output computed for spatially separated SOI and SNOI. The SIR = 0 dB for both receivers. The cyclic frequency was fixed at the SNOI symbol rate in order to separate the SOI estimate. The data record length is 2048 samples with a sample rate of 1 MHz (Left). Top view of surface on the left (Right).

4.2 Maximum Likelihood Approach to Co-Channel Signal Separation

In this section the an estimator for joint TDOA, FDOA and cyclic frequency (α) estimation will be derived using a more complete signal model and a *maximum likelihood* (ML) approach. This section is motivated by the work presented in [14] that does not consider CCI in the signal model and does not result in a practical estimator. In this derivation the effects from CCI on the estimation process are considered. Therefore, a signal model that more accurately describes a CCI environment is used. Throughout the derivation, several simplifying assumptions will be made in order to justify the *alpha*CAF method as a practical estimator. In general, the goal is to arrive at the *alpha*CAF estimator using the ML approach [17]. In this section a slightly simplified version of the signal model introduced in (2.5) and (2.6) will be used. This simplified signal model can be expressed as

$$x_1(n) = s(n) + \sum_{i=1}^{p} s_i(n) + w_1(n) \tag{4.21}$$

$$x_2(n) = s(n-D)\exp(j2\pi f_d n) + \sum_{i=1}^{p} s_i(n-D_i)\exp(j2\pi f_{d_i} n) + w_2(n) \tag{4.22}$$

where the w_n terms represent the noise at each receiver, and the relative amplitude and phase mismatches between receivers have been ignored for mathematical convenience. However, the model does take into account CCI signals with unique delays and Doppler shifts that are received by both receivers.

If N signal samples are collected by each receiver then a vector signal model can be developed from (4.21) and (4.22) to be

$$\begin{bmatrix} \mathbf{x}_1 \\ \mathbf{x}_2 \end{bmatrix} = \begin{bmatrix} \mathbf{s}_n \\ \mathbf{s}_d \end{bmatrix} + \begin{bmatrix} \mathbf{c}_n \\ \mathbf{c}_d \end{bmatrix} + \begin{bmatrix} \mathbf{w}_1 \\ \mathbf{w}_2 \end{bmatrix} \tag{4.23}$$

where,

$$\begin{aligned}
\mathbf{x}_1 &= [x_1(0) \cdots x_1(N-1)]^T \\
\mathbf{x}_2 &= [x_2(0) \cdots x_2(N-1)]^T \\
\mathbf{s}_n &= [s_n(0) \cdots s_n(N-1)]^T \\
\mathbf{s}_d &= [s_d(0) \cdots s_d(N-1)]^T \\
\mathbf{c}_n &= [c_n(0) \cdots c_n(N-1)]^T \\
\mathbf{c}_d &= [c_d(0) \cdots c_d(N-1)]^T \\
\mathbf{w}_i &= [w_i(0) \cdots w_i(N-1)]^T
\end{aligned} \tag{4.24}$$

and $[\bullet]^T$ denotes the transpose operation, and

$$s_n = s(n) \tag{4.25}$$

$$s_d = s(n-D)\exp(j2\pi f_d n) \tag{4.26}$$

$$c_n = \sum_{i=0}^{p} s_i(n) \tag{4.27}$$

$$c_d = \sum_{i=0}^{p} s_i(n-D)\exp(j2\pi f_{d_i} n)\ . \tag{4.28}$$

The vector model in (4.23) can be written in a more compact form as

$$\mathbf{x} = \mathbf{s} + \mathbf{c} + \mathbf{w} \tag{4.29}$$

where each term represents a column vector that is $2N$ samples in length.

The goal is to estimate D, f_d and α. Let's assume the noise environment consists of only zero-mean white Gaussian noise. Therefore, the noise terms are uncorrelated with the signal and interference terms. Following the standard ML approach [17], the noise is modeled with a complex multivariate Gaussian distribution that depends on the signal parameters $\theta = [D, f_d]$. Letting $\mathbf{q} = \mathbf{s} + \mathbf{c}$ the probability distribution function (pdf)

has the form

$$p(\mathbf{w};\theta) = \frac{1}{(2\pi)^{2N}|\mathbf{R}|}\exp\left[-(\mathbf{x}-\mathbf{q})^{*T}\mathbf{R}^{-1}(\mathbf{x}-\mathbf{q})\right] . \tag{4.30}$$

Since the noise is zero-mean white Gaussian, the following definitions

$$\mathbf{R} = N_o\mathbf{I}_{2N\times 2N} \tag{4.31}$$

$$|\mathbf{R}| = N_o^{2N} \tag{4.32}$$

$$\mathbf{R}^{-1} = \frac{1}{N_o}\mathbf{I}_{2N\times 2N} \tag{4.33}$$

can be used with (4.30) to arrive at

$$p(\mathbf{w};\theta) = \frac{1}{(2\pi N_o)^{2N}}\exp\left[-\frac{(\mathbf{x}-\mathbf{q})^{*T}(\mathbf{x}-\mathbf{q})}{N_o}\right] \tag{4.34}$$

where $|\mathbf{R}|$ in (4.32) represents the determinant of the correlation matrix. After dropping the constant out front and expanding the product in the exponential, (4.34) becomes

$$p(\mathbf{w};\theta) \propto \exp\left[\frac{-\mathbf{x}^{*T}\mathbf{x} + \mathbf{x}^{*T}\mathbf{q} + \mathbf{q}^{*T}\mathbf{x} - \mathbf{q}^{*T}\mathbf{q}}{N_o}\right] . \tag{4.35}$$

In order to find the ML estimator $p(\mathbf{w};\theta)$ is maximized with respect to the parameters of interest. Expanding the exponential in (4.35) into the product of individual exponential terms yields

$$p(\mathbf{w};\theta) \propto \exp\left(\frac{-\mathbf{x}^{*T}\mathbf{x}}{N_o}\right)\exp\left(\frac{\mathbf{x}^{*T}\mathbf{q}}{N_o}\right)\exp\left(\frac{\mathbf{q}^{*T}\mathbf{x}}{N_o}\right)\exp\left(\frac{-\mathbf{q}^{*T}\mathbf{q}}{N_o}\right) . \tag{4.36}$$

Using the Taylor series expansion $\exp(x) = 1 + x + \frac{x^2}{2!} + \cdots$ with each of the exponential

terms in (4.36) yields

$$p(\mathbf{w};\theta) \propto \left\{ \begin{array}{l} \left(1 - \frac{\mathbf{x}^{*T}\mathbf{x}}{N_o} + \frac{(\mathbf{x}^{*T}\mathbf{x})^2}{2N_o^2}\right)\left(1 + \frac{\mathbf{x}^{*T}\mathbf{q}}{N_o} + \frac{(\mathbf{x}^{*T}\mathbf{q})^2}{2N_o^2}\right) \\ \times \left(1 + \frac{\mathbf{q}^{*T}\mathbf{x}}{N_o} + \frac{(\mathbf{q}^{*T}\mathbf{x})^2}{2N_o^2}\right)\left(1 - \frac{\mathbf{q}^{*T}\mathbf{q}}{N_o} + \frac{(\mathbf{q}^{*T}\mathbf{q})^2}{2N_o^2}\right) \end{array} \right\} . \tag{4.37}$$

After multiplying out the terms in (4.37) and dropping any terms higher than 4th order, the result is

$$p(\mathbf{w};\theta) \propto \left\{ \begin{array}{c} 1 - \frac{\mathbf{q}^{*T}\mathbf{q}}{N_o} + \frac{(\mathbf{q}^{*T}\mathbf{q})^2}{2N_o^2} + \\ \frac{\mathbf{q}^{*T}\mathbf{x}}{N_o} - \frac{\mathbf{q}^{*T}\mathbf{x}\mathbf{q}^{*T}\mathbf{q}}{N_o^2} + \frac{(\mathbf{q}^{*T}\mathbf{x})^2}{2N_o^2} + \\ \frac{\mathbf{x}^{*T}\mathbf{q}}{N_o} - \frac{\mathbf{x}^{*T}\mathbf{q}\mathbf{q}^{*T}\mathbf{q}}{N_o^2} + \frac{\mathbf{x}^{*T}\mathbf{q}\mathbf{q}^{*T}\mathbf{x}}{N_o^2} + \\ \frac{(\mathbf{x}^{*T}\mathbf{q})^2}{2N_o^2} - \frac{\mathbf{x}^{*T}\mathbf{x}}{N_o} + \frac{\mathbf{x}^{*T}\mathbf{x}\mathbf{q}^{*T}\mathbf{q}}{N_o^2} - \\ \frac{\mathbf{x}^{*T}\mathbf{x}\mathbf{q}^{*T}\mathbf{x}}{N_o^2} - \frac{\mathbf{x}^{*T}\mathbf{x}\mathbf{x}^{*T}\mathbf{q}}{N_o^2} + \frac{(\mathbf{x}^{*T}\mathbf{x})^2}{2N_o^2} \end{array} \right\} . \tag{4.38}$$

For relatively long collection times, the terms in (4.38) with only $\mathbf{x}^{*T}\mathbf{x}$ or $\mathbf{q}^{*T}\mathbf{q}$ inner vector products will only contribute average power to the output. These terms will not depend on the parameters of interest, f_d and D. Therefore, they can be dropped. Also, since the assumption is made that the signals being collected are man-made, but not necessarily cyclostationary, it is safe to assume that since the expected value of most digital communications signals is zero, the expected value of any term with an odd power of SOI terms will go to zero — i.e. $s(n)$ terms, because they will average to zero over the collection time. These two simplifications allow (4.38) to be written as

$$p(\mathbf{w};\theta) \propto \frac{(\mathbf{q}^{*T}\mathbf{x})^2}{2N_o^2} + \frac{\mathbf{x}^{*T}\mathbf{q}\mathbf{q}^{*T}\mathbf{x}}{N_o^2} + \frac{\mathbf{x}^{*T}\mathbf{q}\mathbf{q}^{*T}\mathbf{x}}{N_o^2} + \frac{(\mathbf{x}^{*T}\mathbf{q})^2}{2N_o^2} . \tag{4.39}$$

The four terms in (4.39) make up two sets of conjugate pairs and can be reduced to the

expression

$$p(\mathbf{w};\theta) \propto 2Re\left\{\frac{(\mathbf{x}^{*\mathbf{T}}\mathbf{q})^2}{2N_o^2} + \frac{\mathbf{x}^{*T}\mathbf{x}\mathbf{q}^{*T}\mathbf{q}}{N_o^2}\right\} . \tag{4.40}$$

Now, the terms in (4.40) can be expanded by substituting back in $\mathbf{q} = \mathbf{s} + \mathbf{c}$. Starting with only expanding the numerator of the first term yields

$$(\mathbf{x}^{*T}\mathbf{q})^2 = \mathbf{x}^{*T}\mathbf{s}\mathbf{x}^{*T}\mathbf{s} + \mathbf{x}^{*T}\mathbf{c}\mathbf{x}^{*T}\mathbf{s} + \mathbf{x}^{*T}\mathbf{s}\mathbf{x}^{*T}\mathbf{c} + \mathbf{x}^{*T}\mathbf{c}\mathbf{x}^{*T}\mathbf{c} . \tag{4.41}$$

Taking the first term of (4.41) and expanding yields

$$\mathbf{x}^{*T}\mathbf{s}\mathbf{x}^{*T}\mathbf{s} = \left[\sum_{n_1=0}^{N-1}(x_1^*(n_1)s_n(n_1) + x_2^*(n_1)s_d(n_1)\right]\left[\sum_{n_2=0}^{N-1}(x_1^*(n_2)s_n(n_2) + x_2^*(n_2)s_d(n_2)\right] , \tag{4.42}$$

which is further expanded into four sums as

$$\mathbf{x}^{*T}\mathbf{s}\mathbf{x}^{*T}\mathbf{s} = \left\{\begin{array}{l} \sum_{n_1=0}^{N-1}\sum_{n_2=0}^{N-1} x_1^*(n_1)s_n(n_1)x_2^*(n_2)s_n(n_2) + \\ \sum_{n_1=0}^{N-1}\sum_{n_2=0}^{N-1} x_1^*(n_1)s_n(n_1)x_2^*(n_2)s_d(n_2) + \\ \sum_{n_1=0}^{N-1}\sum_{n_2=0}^{N-1} x_1^*(n_1)s_d(n_1)x_2^*(n_2)s_n(n_2) + \\ \sum_{n_1=0}^{N-1}\sum_{n_2=0}^{N-1} x_1^*(n_1)s_d(n_1)x_2^*(n_2)s_d(n_2) \end{array}\right\} . \tag{4.43}$$

The first sum in (4.43) does not depend on the parameters of interest so it can be disregarded. Following this pattern by expanding the rest of the terms in (4.41) and eliminating any sums that do not depend on the parameters of interest leaves the individual terms

$$\mathbf{x}^{*T}\mathbf{c}\mathbf{x}^{*T}\mathbf{s} = \left\{ \begin{array}{l} \sum_{n_1=0}^{N-1}\sum_{n_2=0}^{N-1} x_1^*(n_1)c_n(n_1)x_2^*(n_2)s_d(n_2) + \\ \sum_{n_1=0}^{N-1}\sum_{n_2=0}^{N-1} x_2^*(n_1)c_d(n_1)x_1^*(n_2)s_n(n_2) + \\ \sum_{n_1=0}^{N-1}\sum_{n_2=0}^{N-1} x_2^*(n_1)c_d(n_1)x_2^*(n_2)s_d(n_2) \end{array} \right\} \tag{4.44}$$

$$\mathbf{x}^{*T}\mathbf{s}\mathbf{x}^{*T}\mathbf{c} = \left\{ \begin{array}{l} \sum_{n_1=0}^{N-1}\sum_{n_2=0}^{N-1} x_1^*(n_1)s_n(n_1)x_2^*(n_2)c_d(n_2) + \\ \sum_{n_1=0}^{N-1}\sum_{n_2=0}^{N-1} x_2^*(n_1)s_d(n_1)x_2^*(n_2)c_n(n_2) + \\ \sum_{n_1=0}^{N-1}\sum_{n_2=0}^{N-1} x_2^*(n_1)s_d(n_1)x_2^*(n_2)c_d(n_2) \end{array} \right\} \tag{4.45}$$

$$\mathbf{x}^{*T}\mathbf{c}\mathbf{x}^{*T}\mathbf{c} = \left\{ \begin{array}{l} \sum_{n_1=0}^{N-1}\sum_{n_2=0}^{N-1} x_1^*(n_1)c_n(n_1)x_2^*(n_2)c_d(n_2) + \\ \sum_{n_1=0}^{N-1}\sum_{n_2=0}^{N-1} x_2^*(n_1)c_d(n_1)x_1^*(n_2)c_n(n_2) + \\ \sum_{n_1=0}^{N-1}\sum_{n_2=0}^{N-1} x_1^*(n_1)c_d(n_1)x_2^*(n_2)c_d(n_2) \end{array} \right\} . \tag{4.46}$$

Doing the same thing for the numerator of the second term in (4.40), $\mathbf{x}^{*\mathbf{T}}\mathbf{q}\mathbf{q}^{*\mathbf{T}}\mathbf{x}$, yields

$$\mathbf{x}^{*T}\mathbf{s}\mathbf{s}^{*T}\mathbf{x} = \left\{ \begin{array}{l} \sum_{n_1=0}^{N-1}\sum_{n_2=0}^{N-1} x_1^*(n_1)s_n(n_1)s_d^*(n_2)x_2(n_2) + \\ \sum_{n_1=0}^{N-1}\sum_{n_2=0}^{N-1} x_2^*(n_1)s_d(n_1)s_n^*(n_2)x_1(n_2) + \\ \sum_{n_1=0}^{N-1}\sum_{n_2=0}^{N-1} x_2^*(n_1)s_d(n_1)s_d^*(n_2)x_2(n_2) \end{array} \right\} \tag{4.47}$$

$$\mathbf{x}^{*T}\mathbf{s}\mathbf{c}^{*T}\mathbf{x} = \left\{ \begin{array}{l} \sum_{n_1=0}^{N-1}\sum_{n_2=0}^{N-1} x_1^*(n_1)s_n(n_1)c_d^*(n_2)x_2(n_2) + \\ \sum_{n_1=0}^{N-1}\sum_{n_2=0}^{N-1} x_2^*(n_1)s_d(n_1)c_n^*(n_2)x_1(n_2) + \\ \sum_{n_1=0}^{N-1}\sum_{n_2=0}^{N-1} x_2^*(n_1)s_d(n_1)c_d^*(n_2)x_2(n_2) \end{array} \right\} \tag{4.48}$$

$$\mathbf{x}^{*T}\mathbf{c}\mathbf{s}^{*T}\mathbf{x} = \left\{ \begin{array}{l} \sum_{n_1=0}^{N-1}\sum_{n_2=0}^{N-1} x_1^*(n_1)c_n(n_1)c_d^*(n_2)x_2(n_2) + \\ \sum_{n_1=0}^{N-1}\sum_{n_2=0}^{N-1} x_2^*(n_1)c_d(n_1)c_n^*(n_2)x_1(n_2) + \\ \sum_{n_1=0}^{N-1}\sum_{n_2=0}^{N-1} x_2^*(n_1)c_d(n_1)c_d^*(n_2)x_2(n_2) \end{array} \right\} \tag{4.49}$$

$$\mathbf{x}^{*T}\mathbf{c}\mathbf{c}^{*T}\mathbf{x} = \left\{ \begin{array}{l} \sum_{n_1=0}^{N-1}\sum_{n_2=0}^{N-1} x_1^*(n_1)s_n(n_1)s_d^*(n_2)x_2(n_2) + \\ \sum_{n_1=0}^{N-1}\sum_{n_2=0}^{N-1} x_2^*(n_1)s_d(n_1)s_n^*(n_2)x_2(n_2) + \\ \sum_{n_1=0}^{N-1}\sum_{n_2=0}^{N-1} x_2^*(n_1)s_d(n_1)s_d^*(n_2)x_2(n_2) \end{array} \right\} . \tag{4.50}$$

After combining all of these terms the result is a large expression of twenty four terms. Obviously, this will be a very difficult expression to work with. Fortunately, some further simplifications can be made by combining similar term pairs. For example, the terms with $x_1^*(n_1)s_n(n_1)x_2^*(n_2)s_d(n_2)$ and $x_2^*(n_1)s_d(n_1)x_1^*(n_2)s_n(n_2)$ are a similar pair. After this reduction, the total expression becomes the following expression of fourteen terms

$$p(\mathbf{w};\theta) \propto \frac{Re}{N_o^2} \left\{ \begin{array}{l} \sum_{n_1=0}^{N-1}\sum_{n_2=0}^{N-1} x_1^*(n_1)s_n(n_1)x_2^*(n_2)s_d(n_2) + \\ \sum_{n_1=0}^{N-1}\sum_{n_2=0}^{N-1} x_2^*(n_1)s_d(n_1)x_2^*(n_2)s_d(n_2) + \\ \sum_{n_1=0}^{N-1}\sum_{n_2=0}^{N-1} x_1^*(n_1)c_n(n_1)x_2^*(n_2)s_d(n_2) + \\ \sum_{n_1=0}^{N-1}\sum_{n_2=0}^{N-1} x_2^*(n_1)c_d(n_1)x_1^*(n_2)s_n(n_2) + \\ \sum_{n_1=0}^{N-1}\sum_{n_2=0}^{N-1} x_2^*(n_1)c_d(n_1)x_2^*(n_2)s_d(n_2) + \\ \sum_{n_1=0}^{N-1}\sum_{n_2=0}^{N-1} x_1^*(n_1)c_n(n_1)x_2^*(n_2)c_d(n_2) + \\ \sum_{n_1=0}^{N-1}\sum_{n_2=0}^{N-1} x_2^*(n_1)c_d(n_1)x_2^*(n_2)c_d(n_2) + \\ 2\sum_{n_1=0}^{N-1}\sum_{n_2=0}^{N-1} x_1^*(n_1)s_n(n_1)s_d^*(n_2)x_2(n_2) + \\ 2\sum_{n_1=0}^{N-1}\sum_{n_2=0}^{N-1} x_2^*(n_1)s_d(n_1)s_d^*(n_2)x_2(n_2) + \\ 2\sum_{n_1=0}^{N-1}\sum_{n_2=0}^{N-1} x_1^*(n_1)s_n(n_1)c_d^*(n_2)x_2(n_2) + \\ 2\sum_{n_1=0}^{N-1}\sum_{n_2=0}^{N-1} x_2^*(n_1)s_d(n_1)c_n^*(n_2)x_1(n_2) + \\ 2\sum_{n_1=0}^{N-1}\sum_{n_2=0}^{N-1} x_2^*(n_1)s_d(n_1)c_d^*(n_2)x_2(n_2) + \\ 2\sum_{n_1=0}^{N-1}\sum_{n_2=0}^{N-1} x_1^*(n_1)c_n(n_1)c_d^*(n_2)x_2(n_2) + \\ 2\sum_{n_1=0}^{N-1}\sum_{n_2=0}^{N-1} x_2^*(n_1)c_d(n_1)c_d^*(n_2)x_2(n_2) \end{array} \right\}. \tag{4.51}$$

Assuming basebanded signals are used and the sample rate for the collection system is significantly greater than the signal bandwidth, (4.51) can be expressed using continuous time notation without loss of generality. For ease of notation lets start by looking only

at the first term in (4.51) after converting to continuous time:

$$\int_0^T \int_0^T x_1^*(t_1) s_n(t_1) x_2^*(t_2) s_d(t_2)\, dt_1\, dt_2 \; . \tag{4.52}$$

Taking the expectation and treating the receiver terms as non-random variables, and the signal terms as random variables, (4.52) can be written as

$$\int_0^T \int_0^T x_1^*(t_1) x_2^*(t_2) R_{s_n s_d^*}(t_1, t_2)\, dt_1\, dt_2 \tag{4.53}$$

where the definition

$$R_{ab}(t_1, t_2) \stackrel{\triangle}{=} E\{a(t_1), b^*(t_2)\} \tag{4.54}$$

has been used. Next, it is assumed that the co-channel interference and the signal of interest terms are uncorrelated since they are presumed to not share the same cyclic frequencies. Note that this assumption is only useful when exploiting cyclostationary processing. However, it is convenient to eliminate correlation terms here with the knowledge that cyclic correlation functions will be substituted later. With this assumption, terms 3, 4, 5, 10, 11 and 12 can be eliminated from (4.51). Now, using continuous time notation the following eight terms remain

$$p(\mathbf{w};\theta) \propto \frac{Re}{N_o^2} \left\{ \begin{array}{l} \int_0^T \int_0^T x_1^*(t_1) x_2^*(t_2) R_{s_n s_d^*}(t_1,t_2)\, dt_1\, dt_2 + \\ \int_0^T \int_0^T x_2^*(t_1) x_2^*(t_2) R_{s_d s_d^*}(t_1,t_2)\, dt_1\, dt_2 + \\ \int_0^T \int_0^T x_1^*(t_1) x_2^*(t_2) R_{c_n c_d^*}(t_1,t_2)\, dt_1\, dt_2 + \\ \int_0^T \int_0^T x_2^*(t_1) x_2^*(t_2) R_{c_d c_d^*}(t_1,t_2)\, dt_1\, dt_2 + \\ 2\int_0^T \int_0^T x_1^*(t_1) x_2(t_2) R_{s_n s_d}(t_1,t_2)\, dt_1\, dt_2 + \\ 2\int_0^T \int_0^T x_2^*(t_1) x_2(t_2) R_{s_d s_d}(t_1,t_2)\, dt_1\, dt_2 + \\ 2\int_0^T \int_0^T x_1^*(t_1) x_2(t_2) R_{c_n c_d}(t_1,t_2)\, dt_1\, dt_2 + \\ 2\int_0^T \int_0^T x_2^*(t_1) x_2(t_2) R_{c_d c_d}(t_1,t_2)\, dt_1\, dt_2 \end{array} \right\} . \tag{4.55}$$

Using the definition from Gardner [13] that

$$\hat{R}^{\alpha}_{x_T y_T} \triangleq \int_0^T x_T(t+\tau/2) y_T^*(t-\tau/2) \exp(-j2\pi\alpha t)\, dt \tag{4.56}$$

where

$$\begin{aligned} x_T &= u(t-\tau/2)x(t) \\ y_T &= u(t-\tau/2)y(t) \end{aligned} \tag{4.57}$$

$$u(t) = \left\{ \begin{array}{ll} 1 & |t| < T/2 \\ 0 & \text{otherwise} \end{array} \right. \tag{4.58}$$

and also from [13] that

$$R_{ab}(t_1,t_2) = \sum_{\alpha} R^{\alpha}_{ab}(t_1-t_2) \exp(j\pi\alpha(t_1+t_2)) \, , \tag{4.59}$$

the following form is arrived at for the first term in (4.55)

$$\begin{aligned} &\int_0^T \int_0^T x_1^*(t_1) x_2^*(t_2) R_{s_n s_d^*}\, dt_1\, dt_2 = \\ &\textstyle\int_0^T \int_0^T x_1^*(t_1) x_2^*(t_2) \sum_{\alpha} R^{\alpha}_{s_n s_d^*}(t_1-t_2) \exp(j\pi\alpha(t_1+t_2)\, dt_1\, dt_2 \, . \end{aligned} \tag{4.60}$$

Substituting in (4.56) and working out some basic tedious algebra enables (4.60) to be expressed as

$$\int_0^T \int_0^T x_1^*(t_1) x_2^*(t_2) R_{s_n s_d^*}\, dt_1\, dt_2 = \sum_\alpha \int_0^T \hat{R}^\alpha_{x_1^* x_2}(\tau) R^\alpha_{s_n^* s_d}(\tau)^*\, d\tau \ . \tag{4.61}$$

The total expression for the pdf in (4.55) can now be written as

$$p(\mathbf{w};\theta) \propto \frac{Re}{N_o^2} \left\{ \begin{array}{l} \sum_\alpha \int_0^T \hat{R}^\alpha_{x_1^* x_2}(\tau) R^\alpha_{s_n^* s_d}(\tau)^*\, d\tau + \\ \sum_\alpha \int_0^T \hat{R}^\alpha_{x_2^* x_2}(\tau) R^\alpha_{s_d^* s_d}(\tau)^*\, d\tau + \\ \sum_\alpha \int_0^T \hat{R}^\alpha_{x_1^* x_2}(\tau) R^\alpha_{c_n^* c_d}(\tau)^*\, d\tau + \\ \sum_\alpha \int_0^T \hat{R}^\alpha_{x_2^* x_2}(\tau) R^\alpha_{c_n^* c_d}(\tau)^*\, d\tau + \\ 2\sum_\beta \int_0^T \hat{R}^\beta_{x_2 x_1}(\tau) R^\beta_{s_n s_d}(\tau)^*\, d\tau + \\ 2\sum_\beta \int_0^T \hat{R}^\beta_{x_2 x_2}(\tau) R^\beta_{s_d s_d}(\tau)^*\, d\tau + \\ 2\sum_\beta \int_0^T \hat{R}^\beta_{x_2 x_1}(\tau) R^\beta_{c_n c_d}(\tau)^*\, d\tau + \\ 2\sum_\beta \int_0^T \hat{R}^\beta_{x_2 x_2}(\tau) R^\beta_{c_d c_d}(\tau)^*\, d\tau \end{array} \right\} \tag{4.62}$$

where α and β are the conjugate and non conjugate cyclic frequencies [13].

Next, s_n, s_d, c_n, and c_d are substituted into (4.62) to get it in terms of the received signals $x_1(t)$ and $x_2(t)$. In order to avoid dealing with the summations in (4.27) and (4.28) it is assumed that only one SNOI is present. With these substitutions and

assumptions the correlation function in (4.62) becomes

$$p(\mathbf{w};\theta) \propto \frac{Re}{N_o^2} \left\{ \begin{array}{l} \sum_{\alpha} \int_0^T \hat{R}^{\alpha}_{x_1^* x_2}(\tau) R^{\alpha+f_d}_{s_n^* s_n}(\tau - D)^* \exp(-j\pi(\alpha + f_d)D) \exp(-j\pi f_d \tau)\, d\tau + \\ \sum_{\alpha} \int_0^T \hat{R}^{\alpha}_{x_2^* x_2}(\tau) R^{\alpha+2f_d}_{s_n^* s_n}(\tau)^* \exp(-j\pi(\alpha + 2f_d)D) \exp(-j2\pi f_d \tau)\, d\tau + \\ \sum_{\alpha} \int_0^T \hat{R}^{\alpha}_{x_1^* x_2}(\tau) R^{\alpha+f_d}_{s^* s}(\tau - D)^* \exp(-j\pi(\alpha + f_d)D) \exp(-j\pi f_d \tau)\, d\tau + \\ \sum_{\alpha} \int_0^T \hat{R}^{\alpha}_{x_2^* x_2}(\tau) R^{\alpha+f_d}_{s^* s}(\tau - D)^* \exp(-j\pi(\alpha + f_d)D) \exp(-j\pi f_d \tau)\, d\tau + \\ 2\sum_{\beta} \int_0^T \hat{R}^{\beta}_{x_2 x_1}(\tau) R^{\beta+f_d}_{s_n s_n}(\tau - D)^* \exp(-j\pi(\beta + f_d)D) \exp(j\pi f_d \tau)\, d\tau + \\ 2\sum_{\beta} \int_0^T \hat{R}^{\beta}_{x_2 x_2}(\tau) R^{\beta+2f_d}_{s_n s_n}(\tau)^* \exp(-j\pi(\beta + 2f_d)D) \exp(-j2\pi f_d \tau)\, d\tau + \\ 2\sum_{\beta} \int_0^T \hat{R}^{\beta}_{x_2 x_1}(\tau) R^{\beta+f_d}_{ss}(\tau - D)^* \exp(-j\pi(\beta + f_d)D) \exp(j\pi f_d \tau)\, d\tau + \\ 2\sum_{\beta} \int_0^T \hat{R}^{\beta}_{x_2 x_2}(\tau) R^{\beta+2f_d}_{ss}(\tau)^* \exp(-j\pi(\beta + 2f_d)D) \exp(-j2\pi f_d \tau)\, d\tau \end{array} \right\} \tag{4.63}$$

where the complete expression represents an ideal estimator because it requires knowledge of the SOI and SNOI for the computation of the cyclic correlation functions. Since this knowledge is generally not available in practice, the cyclic correlation functions computed using the signal data $x_1(t)$ are substituted for the ideal cyclic correlation functions of the known SOI. After dropping conjugate terms, replacing $x_1(t)$ or $x_2(t)$ with x and y respectively, keeping only one term from similar term pairs and keeping only terms that depend only upon the two parameters of interest, (4.63) becomes

$$p(\mathbf{w};\theta) \propto \frac{2Re}{N_o^2} \left\{ \sum_{\alpha} \int_0^T \hat{R}^{\beta}_{yx}(\tau) R^{\beta+f_d}_{x}(\tau - D)^* \exp(-j\pi(\beta + f_d)D) \exp(-j\pi f_d \tau)\, d\tau \right\}. \tag{4.64}$$

Notice that this is very similar to the function derived in Section 4.1. In fact, after shifting the limits of integration and letting $f_d = f$ and $\beta = \alpha - f$, (4.64) computed at

a fixed cyclic frequency reduces to

$$p(\mathbf{w};\theta) \propto K \int_{-T/2}^{T/2} \hat{R}_{yx}^{\alpha-f}(\tau) R_x^{\alpha}(\tau - D)^* \exp(-j2\pi\alpha D) \exp(-j\pi f\tau)\, d\tau \ . \tag{4.65}$$

which is almost identical to the *alpha*CAF function derived in Section 4.1 except for the constant phase term, which can be moved out of the integral into the complex amplitude term, yielding

$$p(\mathbf{w};\theta) \propto K' \int_{-T/2}^{T/2} \hat{R}_{yx}^{\alpha-f}(\tau) R_x^{\alpha}(\tau - D)^* \exp(-j2\pi f\tau)\, d\tau \ . \tag{4.66}$$

This suggests that the *alpha*CAF function can be arrived at using the ML approach and several simplifying assumptions. In the next chapter it will be determined if the *alpha*CAF estimator approaches optimal performance for large data records and high SNR scenarios. Specifically, it will be explored experimentally whether or not the *alpha*CAF estimator is a less biased estimator than the CAF when CCI and closely spaced emitters are a concern.

Chapter 5 – ALGORITHM PERFORMANCE — ILLUSTRATIVE EXAMPLES

5.1 Test Environments

To demonstrate the tolerance to co-channel interference and the separation capabilities exhibited by the new *alpha*CAF method, two simulated collection test environments are considered. The two test environments cover scenarios of narrow-band interference to wide-band interference and single and multiple signal sources. In both environments there is uncorrelated zero-mean Gaussian noise added to the received signals. Several SNR conditions are considered for each test environment. In this sense, the analysis is similar to the analysis in [10] used to test cyclostationary TDOA only estimation algorithms. A similar format is used here so that comparisons to the analysis in the literature are possible. In all cases the SOI is the same signal used throughout the previous chapters, with parameters listed in Table 2.2. The sample rate for both receivers is f_s =1 MHz. The data record length is fixed for all the following examples to be $2048T_s$. For the qualitative analysis, interpolation is not used and therefore the nearest sample quantization error in the measurements is expected to be on the order of 1 microsecond for the TDOA and 488 Hz for the FDOA. For the quantitative analysis a simple polynomial interpolation method is used to get more precise estimates. Each test environment is discussed in detail in the following subsections.

5.1.1 Environment A: Wide-band Co-Channel Interference

In this environment the interference consists of two BPSK modulated signals with carrier frequencies of $f_1 = 0.218 f_s$ and $f_2 = 0.281 f_s$ and bandwidths of $B_1 = 0.102 f_s$ and $B_2 = 0.125 f_s$ respectively. The location of the first interference emitter is approximately 1 km away from the SOI emitter. The location of the second interference emitter is only 0.5 km away from the SOI emitter. The predicted TDOA for the SOI is 70 microseconds. The interference signals have a predicted TDOA of 63 microseconds and 66 microseconds respectively. The predicted FDOA for the SOI is -850 Hz and the predicted FDOA for the interference signals are -845 Hz and -843 Hz respectively. The spatial locations of the emitters are chosen such that separate delay/Doppler estimates for each emitter should not be possible using the conventional CAF method given the signal bandwidths and the fixed collection time.

5.1.2 Environment B: Narrow-band Co-Channel Interference

In this test environment, the interference consists of one BPSK modulated signal with a carrier frequency of $f_1 = 0.242 f_s$ and a bandwidth of $B_1 = 0.031 f_s$. Note that the interfering signal spectrum lies completely within the SOI spectrum and is considered a narrow-band interferer. The location of the narrow-band interference emitter is approximately 0.5 km away from the SOI emitter. The predicted TDOA for the SOI is 70 microseconds and the predicted TDOA for the interference signal is 66 microseconds. The predicted FDOA for the SOI is -850 Hz and the predicted FDOA for the interference signal is -845 Hz. Again, th emitter locations were chosen so that separate estimates for the SOI emitter and SNOI emitter should not be possible using the conventional CAF method.

5.2 Qualitative Assessment of Estimator Bias

In order to properly assess the increased resolution performance of the new *alpha*CAF method, it is compared to the conventional CAF method using the test environments described above. In Figure 5.1 the conventional CAF output is displayed for Test Environment A and a SIR of 0 dB. Although there are three co-channel signals received, the CAF method is not able to produce separate peaks for each signal. The cross-section plot for the TDOA dimension shows a double peak. One side of the double peak is at the predicted TDOA for one of the interfering signals (66 microseconds). The other peak is located at a larger TDOA value than the actual SOI TDOA. It is not possible to make out three separate peaks even though it is known that there are actually three emitters involved. Notice that an estimate of the SOI TDOA in this scenario is biased, which will result in an incorrect location estimate if this TDOA is used to generate x,y location parameters.

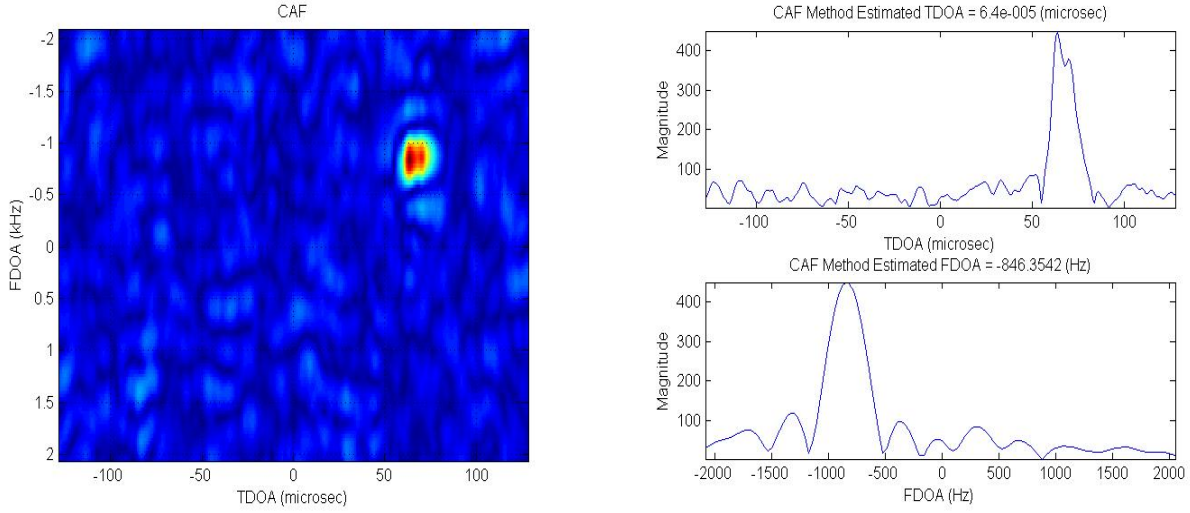

Figure 5.1: Top view of conventional CAF output for test environment A, SIR = 0 dB (Left). Cross-section plots from surface plot on the left in both the TDOA and FDOA dimension (Right).

In contrast, the output from the *alpha*CAF (computed at a cyclic frequency equal to

the SOI symbol rate of 62,500 Hz) displayed in Figure 5.2 is able to uniquely separate the peak for the SOI and provide an accurate TDOA estimate of 70 microseconds and FDOA estimate of -849 Hz. It was shown in the last chapter that the peaks for the interfering signals can also be uniquely separated. Notice in the *alpha*CAF cross-section plots that the TDOA and FDOA measurements for the SOI match the actual values within the expected error range. It will be quantitatively demonstrated in the next section that unlike the conventional CAF, the *alpha*CAF estimates are unbiased even though the co-channel emitters are located spatially close together. Figures 5.3 and 5.4 show the same analysis using Test Environment A, but with a lower SIR of -6 dB at both receivers. Even at the lower SIR accurate estimates are produced.

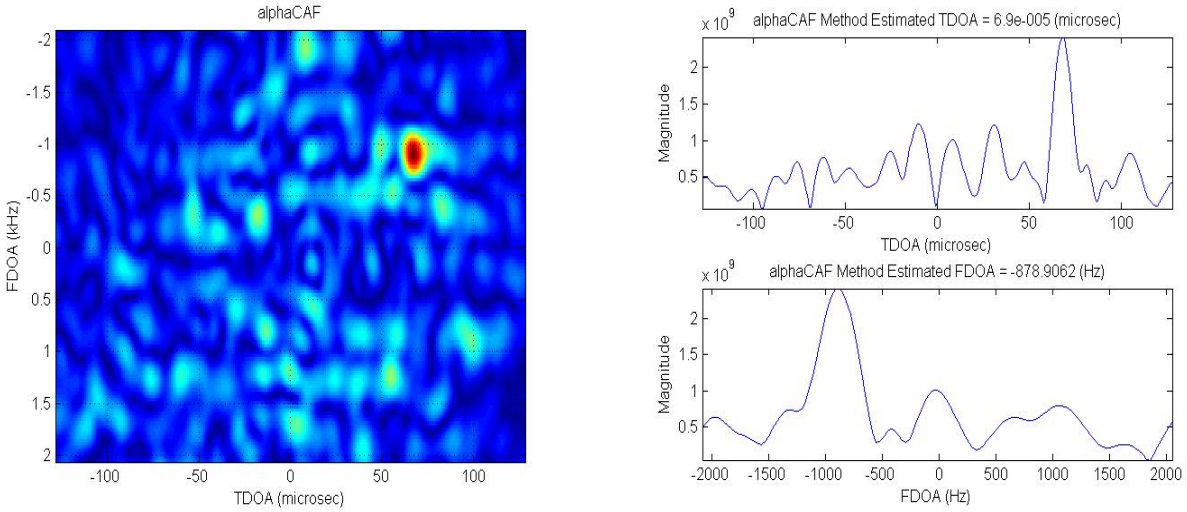

Figure 5.2: Top view of new *alpha*CAF output for test environment A, SIR = 0 dB (Left). Cross-section plots from surface plot on the left in both the TDOA and FDOA dimension (Right).

Now, the same analysis will be illustrated for Test Environment B. As mentioned earlier, this is a narrow-band case where the interfering signal bandwidth is completely inside the SOI bandwidth. In Figure 5.5 the conventional CAF output is displayed for Test Environment B with a SIR of 0 dB. Since there are two co-channel signals

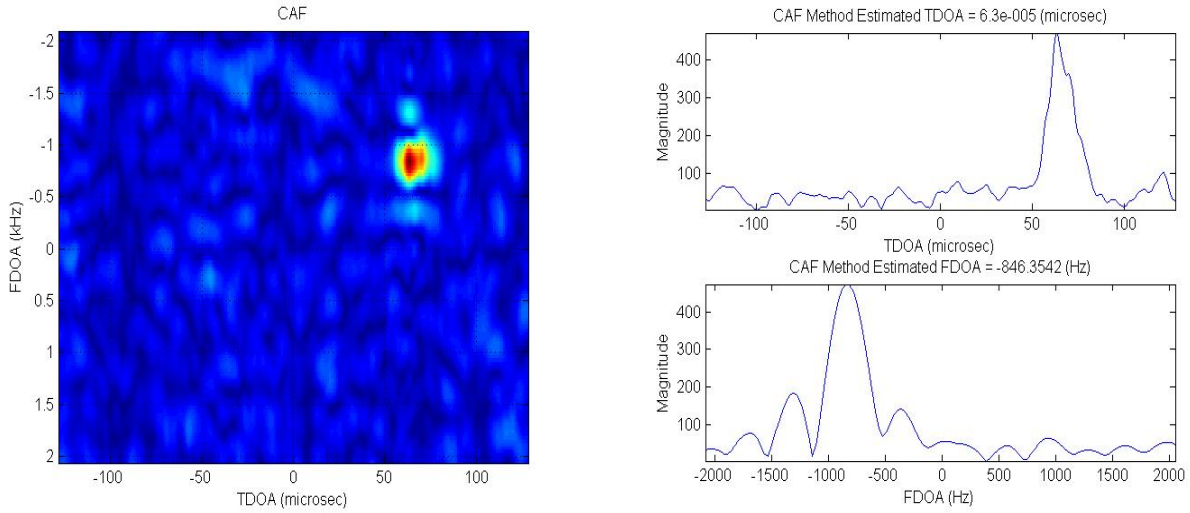

Figure 5.3: Top view of conventional CAF output for test environment A, SIR = -6 dB (Left). Cross-section plots from surface plot on the left in both the TDOA and FDOA dimension (Right).

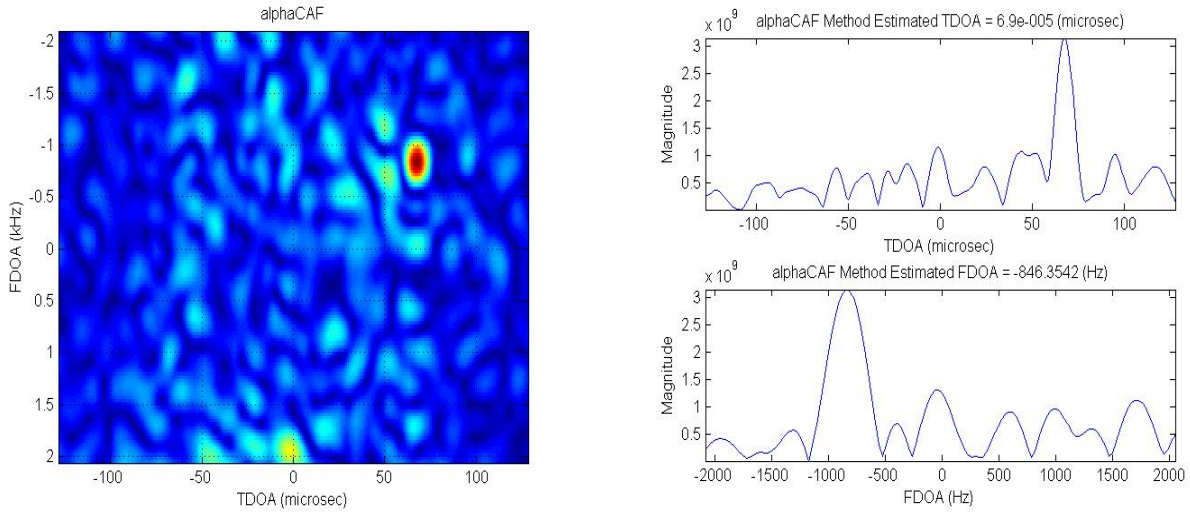

Figure 5.4: Top view of new *alpha*CAF output for test environment A, SIR = -6 dB (Left). Cross-section plots from surface plot on the left in both the TDOA and FDOA dimension (Right).

received, two peaks are expected. However, the CAF method is again not capable of distinguishing the TDOA and FDOA parameters for both the SOI and SNOI. Looking at the cross-section plots only one peak can be seen. The peak location is closer to the

predicted TDOA for the interfering signal (66 microseconds) than it is to the actual SOI TDOA. In other words, the estimate for the SOI TDOA is biased toward the SNOI TDOA. Therefore, it is not possible to make an accurate measurement for the SOI due to the narrow-band CCI and close interfering emitter.

In contrast, the output from the *alpha*CAF method displayed in Figure 5.6 is again able to uniquely separate the peak corresponding to the SOI and provide a TDOA estimate of 70 Microseconds and an FDOA estimate of -849 Hz. By using the *alpha*CAF method it is possible to get a TDOA and FDOA measurement for a SOI even with the co-channel interference from a spatially close emitter. Figures 5.7 and 5.8, show the same analysis using Test Environment B, but with a lower SIR of -6 dB at both receivers. Again, accurate estimates are produced even at the lower SIR.

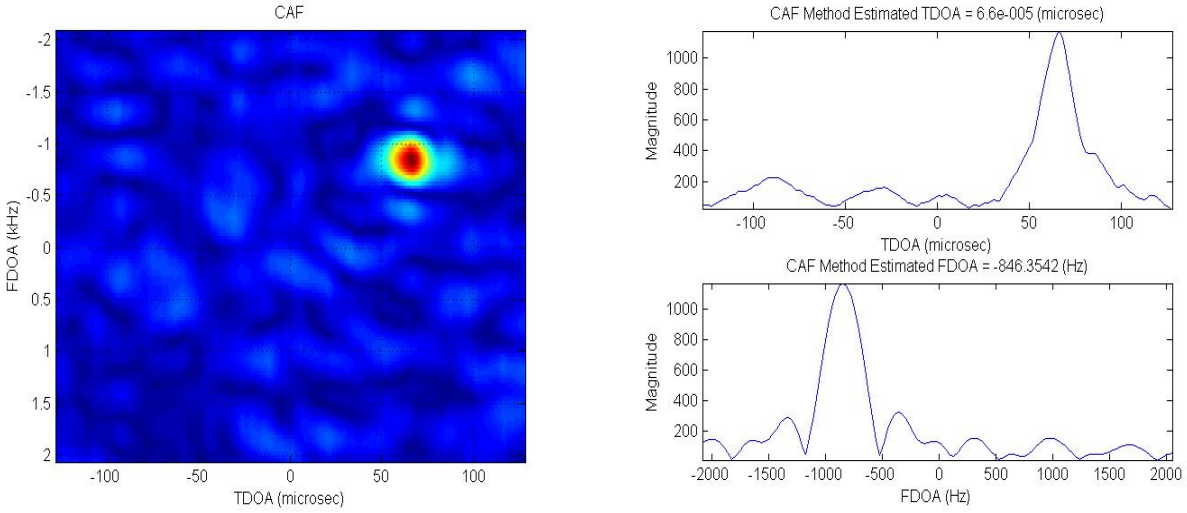

Figure 5.5: Conventional CAF output for test environment B, SIR = 0 dB (Left). Top view of surface on the left (Right).

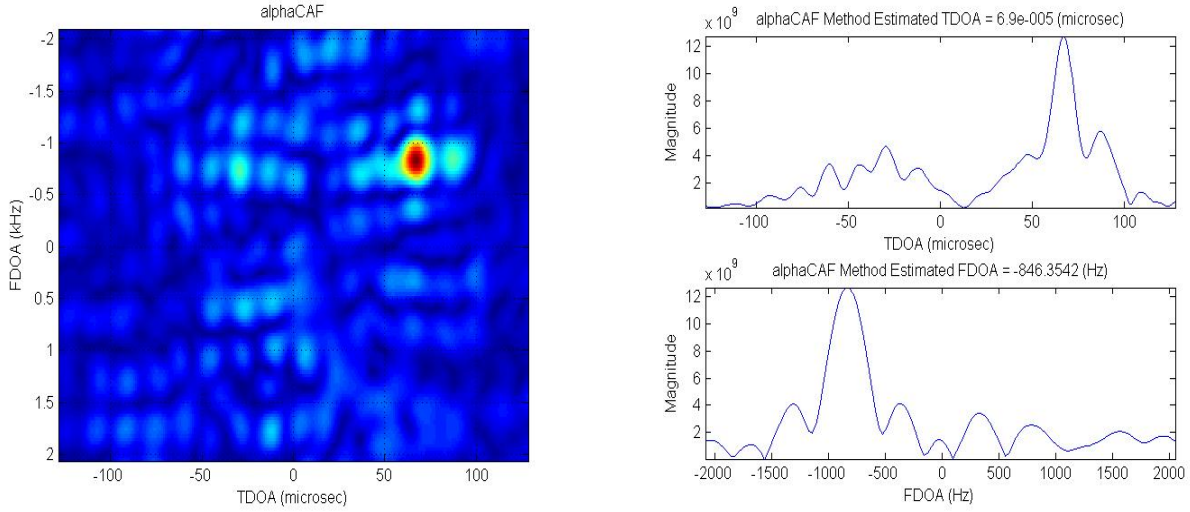

Figure 5.6: New *alpha*CAF output for test environment B, SINR = 0 dB (Left). Top view of surface on the left (Right).

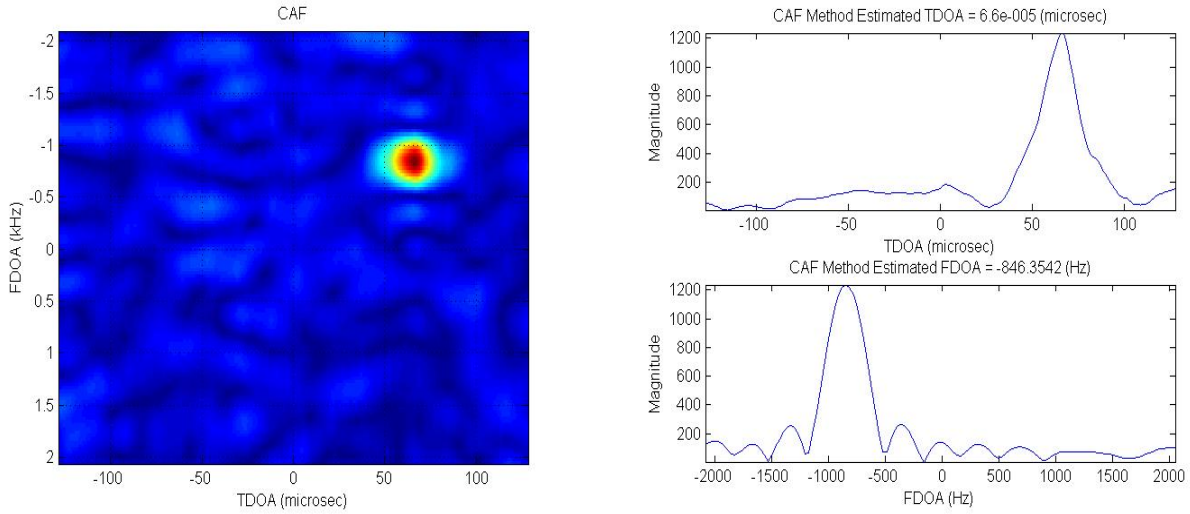

Figure 5.7: Conventional CAF output for test environment B, SINR = -6 dB (Left). Top view of surface on the left (Right).

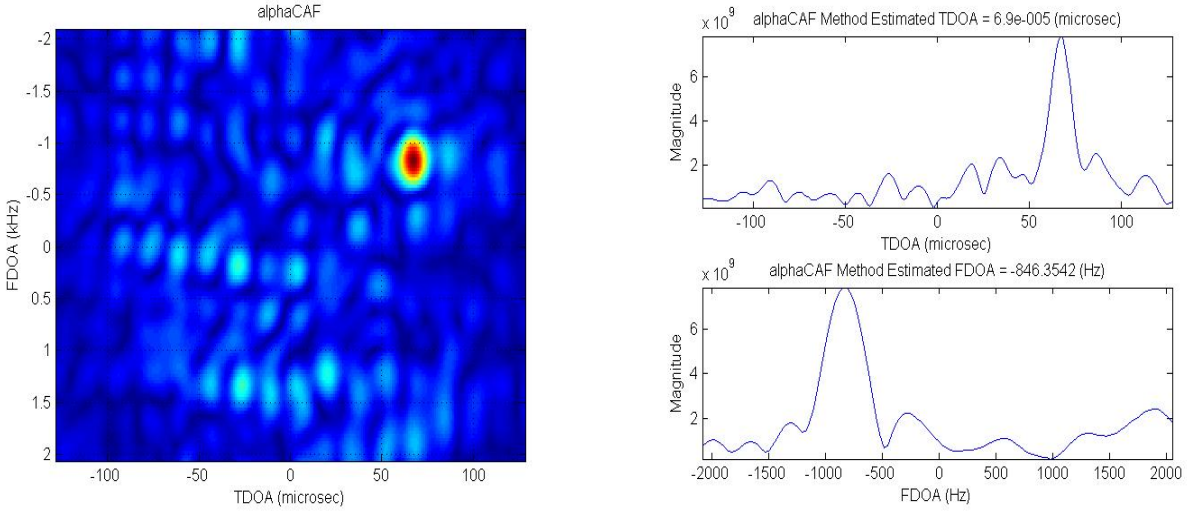

Figure 5.8: New *alpha*CAF output for test environment B, SINR = -6 dB (Left). Top view of surface on the left (Right).

5.3 Quantitative Assessment of Estimator Bias

To quantitatively assess the estimate bias when using the *alpha*CAF method, the same simulated signals and test environments used in the previous section are considered in this section. The goal of this section is to experimentally determine if the *alpha*CAF method produces unbiased estimates when the CAF method does not. The conventional CAF estimator is a maximum likelihood estimator if only a single SOI is present in AWGN [7], and therefore an unbiased estimator for large enough data records [17]. However, it has been shown in this thesis that the CAF method produces biased estimates when multiple co-channel signals are received that originate from spatially close emitters. This was demonstrated qualitatively in the last section using both wide-band and narrow-band CCI.

In order to quantitatively explore the question about the *alpha*CAF estimator's capability to produce unbiased estimates a multi-trial, or Monte Carlo analysis for several collection lengths and different SNR conditions was conducted. This approach was chosen due to the difficult and intractable appearance of proving this fact analytically. To simplify the analysis FDOA was fixed and only TDOA estimates were considered. At this stage it will be assumed that the bias behavior in the TDOA dimension is representative of the FDOA dimension. Analysis of the full three-dimensional bias performance of the *alpha*CAF estimator will be left for future research efforts.

For each collection length multiple independent data records were simulated. For each data record a CAF surface and a *alpha*CAF surface were computed. Interpolation was used on each surface to get more precise measurements. Next, peak detection was performed as an estimate of TDOA. Using the estimates for all trials for a given collection length a histogram was computed along with the mean and variance of the estimates. The mean was then compared to the true TDOA value predicted from the

collection geometry. The precise predicted SOI TDOA from the collection geometry was 69.80 microseconds. The predicted SNOI TDOA from the collection geometry was 66.60 microseconds. Note that given a collection geometry like the one in Figure 2.2, the SNOI can only bias the SOI estimate in the TDOA dimension. Therefore, the statistics for the FDOA measurements were not considered, but in other scenarios it may need to be considered in order to completely test the 2-D (and even 3-D) bias characteristics.

First, a baseline of performance was established using a collection length of 2048 samples. The left plot in Figure 5.9 shows a histogram generated using 1000 TDOA measurements computed using the conventional CAF and 1000 independent simulated data records. The simulations consisted of only the SOI with AWGN. The mean and the variance of the measurements were computed to be 69.77 microseconds and 0.01 respectively. The estimated mean was reasonably close to the actual predicted TDOA of 69.80 microseconds. The predicted variance using (2.36) was computed to be 0.008. Notice that the distribution in the left plot of Figure 5.9 is approximately Gaussian, except for an unexplained artifact on the right end.

The right plot in Figure 5.9 shows a histogram generated using another 1000 TDOA measurements, but computed using the new *alpha*CAF method. Again, the distribution is approximately Gaussian. The mean and variance of the measurements was computed to be 69.61 microseconds and 0.094 respectively. The measured TDOA was less than that measured using the CAF method. However, it is reasonably close to the predicted TDOA and the difference is likely due to the difference in Matlab code for each process. As far as the variance is concerned it was unlikely that (2.36) accurately applies to cyclostationary joint estimation, as the data suggests. The statistics from the plots in Figure 5.9 will be used as a baseline estimate for the next tests.

Next, the same analysis for both a SOI and a SNOI in AWGN was considered. Figures 5.10 and 5.11 display histograms generated from 250 independent trials with

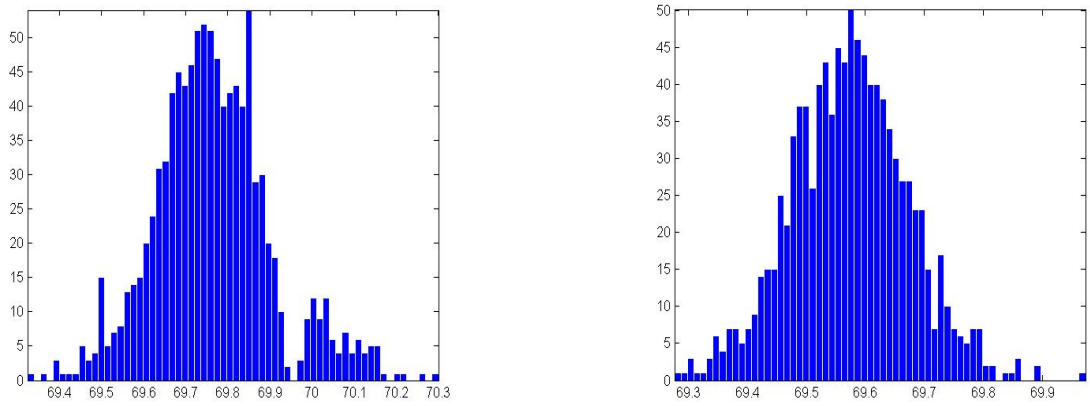

Figure 5.9: Baseline histogram from 1000 trials computed using the conventional CAF method for the SOI only scenario (Left). Histogram from 1000 trials computed using the *alpha*CAF method for the SOI only scenario (Right).

TDOA measurements computed by both the conventional CAF and *alpha*CAF methods. Two separate collection lengths were used with an SIR of 0 dB.

From the examples in Figures 5.10 and 5.11 the CAF method histogram means were 66.65 microseconds for the 2048 sample length collection and 66.62 microseconds for the 4096 sample length collection. The variances were 0.011 and 0.005 respectively. Remember from Figure 5.1 that the CAF was unable to generate unique peaks for both the SOI and the SNOI. Instead, it produced one wider peak that was shifted toward the actual SNOI TDOA value, resulting in a biased measurement. The histogram analysis also suggests that indeed the conventional CAF method does produce biased estimates when co-channel emitters are too close together. A much larger number of independent trials would need to be used in order to more definitively determine the validity of the bias claims.

From Figure 5.11 the *alpha*CAF method histogram means were 68.97 microseconds for the 2048 sample length collection and 69.04 microseconds for the 4096 sample length collection, with variances of 0.096 and 0.059 respectively. These measurements differ

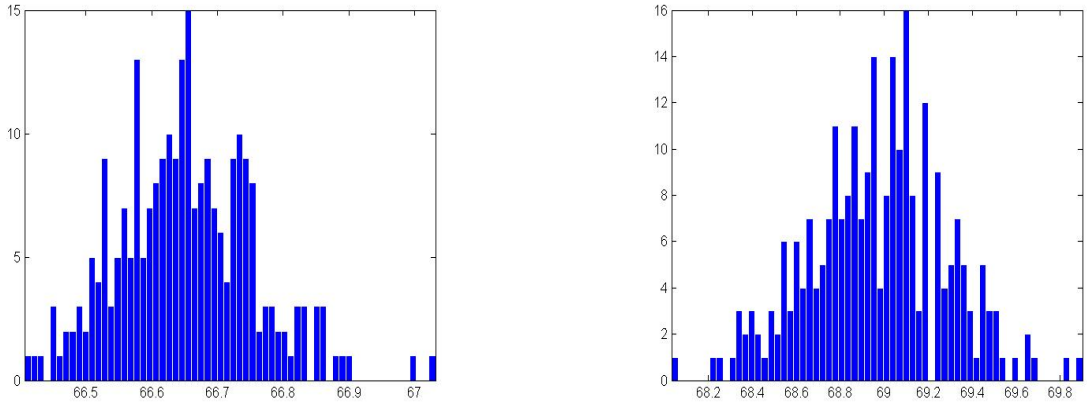

Figure 5.10: Histogram from 250 trials computed using the conventional CAF method for the SOI and SNOI scenario. Data record length was 2048 samples, SIR = 0 dB (Left). Histogram from 250 trials computed using the *alpha*CAF method for the SOI and SNOI scenario. Data record length was 2048 samples, SIR = 0 dB (Right).

from the baseline measurement by approximetely 0.6 microseconds. However, they are considerably better than the measurements from the conventional CAF method and less than 1 microsecond in error from the baseline estimate. Also, the estimates tend to get better with longer data records, and more trials are most certainly necessary for more accurate results.

Next, the same analysis was considered for both a SOI and a SNOI in AWGN, but for a lower SIR. Figures 5.12 and 5.13 display histograms generated from 250 TDOA measurements computed by both the conventional CAF and *alpha*CAF methods using two separate collection lengths and an SIR of -10 dB. For these examples the CAF method histogram means were 66.65 microseconds for the 2048 sample length collection and 66.62 microseconds for the 4096 sample length collection. These are identical to the means for the SIR equals 0 dB examples. However, as expected the variances are slightly larger. The *alpha*CAF method histogram means are 68.95 microseconds for the 2048 sample length collection and 69.00 microseconds for the 4096 sample length collection, with variances of 0.114 and 0.065 respectively. Again, the measurements from

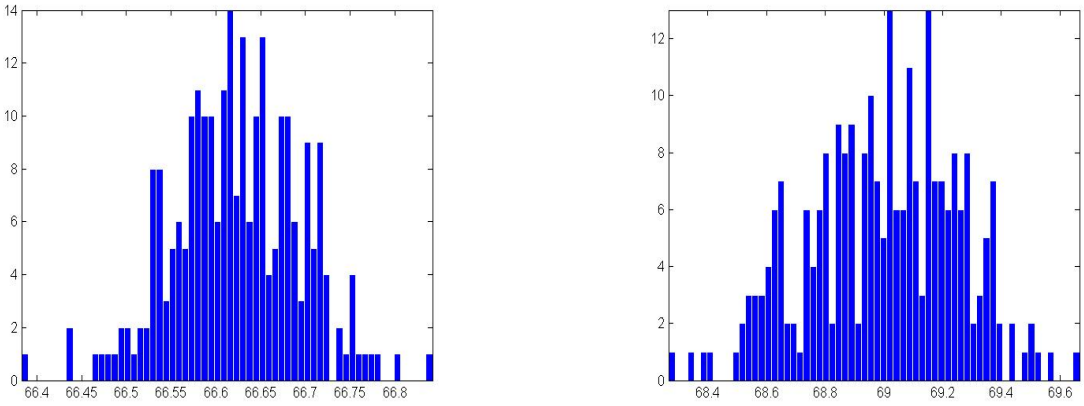

Figure 5.11: Histogram from 250 trials computed using the conventional CAF method for the SOI and SNOI scenario. Data record length was 4096 samples, SIR = 0 dB (Left). Histogram from 250 trials computed using the *alpha*CAF method for the SOI and SNOI scenario. Data record length was 4096 samples, SIR = 0 dB (Right).

the *alpha*CAF method are much better than the CAF method measurements.

From the analysis presented in this section it is possible to suggest that the *alpha*CAF method produces estimates that probably trend toward an unbiased behavior given adequate collection lengths. The *alpha*CAF outperforms the conventional CAF method when a SOI overlaps spectrally with a SNOI and their emitters are too closely located for conventional methods to resolve separate estimates.

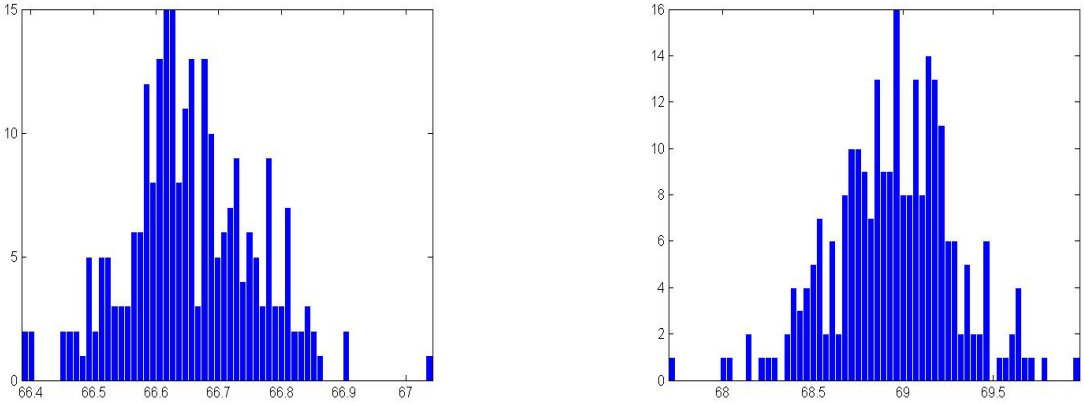

Figure 5.12: Histogram from 250 trials computed using the conventional CAF method for the SOI and SNOI scenario. Data record length was 2048 samples, SIR = -6 dB (Left). Histogram from 250 trials computed using the *alpha*CAF method for the SOI and SNOI scenario (Right).

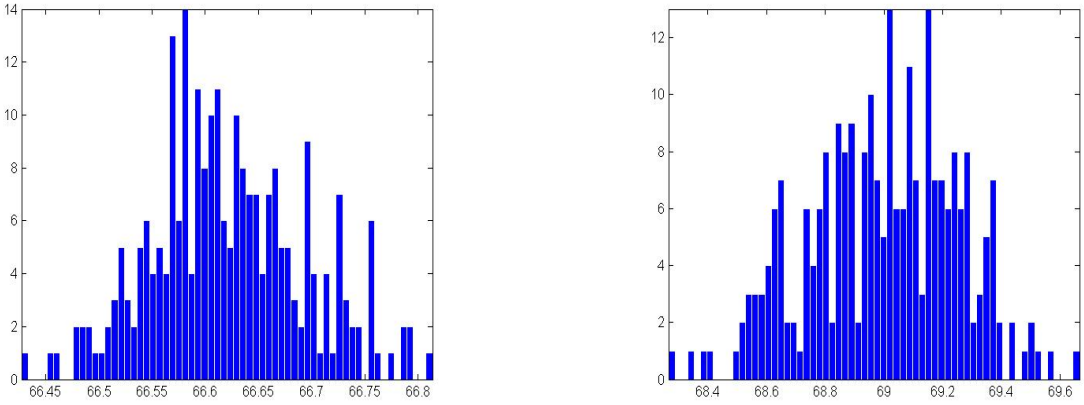

Figure 5.13: Histogram from 250 trials computed using the conventional CAF method for the SOI and SNOI scenario. Data record length was 4096 samples, SIR = -6 dB (Left). Histogram from 250 trials computed using the *alpha*CAF method for the SOI and SNOI scenario (Right).

Chapter 6 – ALGORITHM PERFORMANCE — PARAMETRIC TRADEOFFS

6.1 Resolution Capabilities

To further demonstrate the capabilities of the *alpha*CAF method, in this chapter its resolution performance is compared to the resolution performance of the conventional CAF method. The major advantage of the *alpha*CAF method over the conventional CAF method is evidenced when a fixed-length data record is used to estimate TDOA and FDOA when multiple emitters are contributing to the signal received at the collectors. In this scenario the conventional CAF method may or may not produce separate TDOA and FDOA estimates for each emitter. Recall from Chapter 2 that the width of the CAF peak in the FDOA dimension is proportional to the inverse of the observation time. Also, the width of the CAF peak in the TDOA dimension is proportional to the inverse of the measured signal bandwidth. These facts set a limit on the resolution capability of the conventional CAF method. If two emitters are spatially located such that their respective signal correlations in the CAF surface are not resolvable, then separate estimates for geolocation will not be possible no matter how much effort is put into the computations — i.e., interpolation, etc. On the other hand, the *alpha*CAF method exploits additional signal properties to overcome the resolution limitations of the conventional CAF method. Since most of the man-made signals used in modern communications have cyclostationary features, the *alpha*CAF method can be widely applied to overcome the deficiencies of the conventional CAF method.

In order to demonstrate and assess the improved resolution capabilities of the *al-*

*pha*CAF method, this section begins with several simulated comparisons. Figure 6.1 shows four cross-section plots in the TDOA dimension. Each plot has the combined results from both a conventional CAF surface and two separate *alpha*CAF surfaces, each one computed from the same data record. For each plot the data record consisted of a SOI and a SNOI from two spatially separated emitters. The signal modulation and frequency parameters were the same as those listed in Table 2.2. However, the individual emitter TDOAs were simulated to vary from a large value (easily separable in the CAF surface) to a small value (not separable within the CAF surface) in order to demonstrate the higher resolution capabilities of the *alpha*CAF method. The individual *alpha*CAF cross-sections in each plot where computed for the SOI and SNOI symbol rates respectively.

It is interesting to notice that the *alpha*CAF method was able to separate the SOI and SNOI as the difference in TDOA became smaller. On the other hand, the conventional CAF method produced only a single peak for small TDOA differences. Likewise, Figure 6.2 shows a similar analysis for the FDOA dimension. The interesting observation about the FDOA dimension is that the conventional CAF method gave a biased estimate for one or the other of the two signals (SOI and SNOI) in almost every plot. In the bottom right plot only a single peak is observed in the CAF and the peak is located almost halfway between the two true SOI and SNOI TDOA values. It appears that FDOA estimation using the conventional CAF method is more sensitive to co-channel interference than TDOA estimation.

Figure 6.3 shows the same analysis as Figure 6.1, but for a longer data record length of 8192 samples. Since TDOA peak resolution is only affected by the signal bandwidth and not the observation time, Figures 6.1 and 6.3 are not noticeably different. Again, the *alpha*CAF method separated the individual TDOA peaks for both the SOI and SNOI while the conventional CAF method did not.

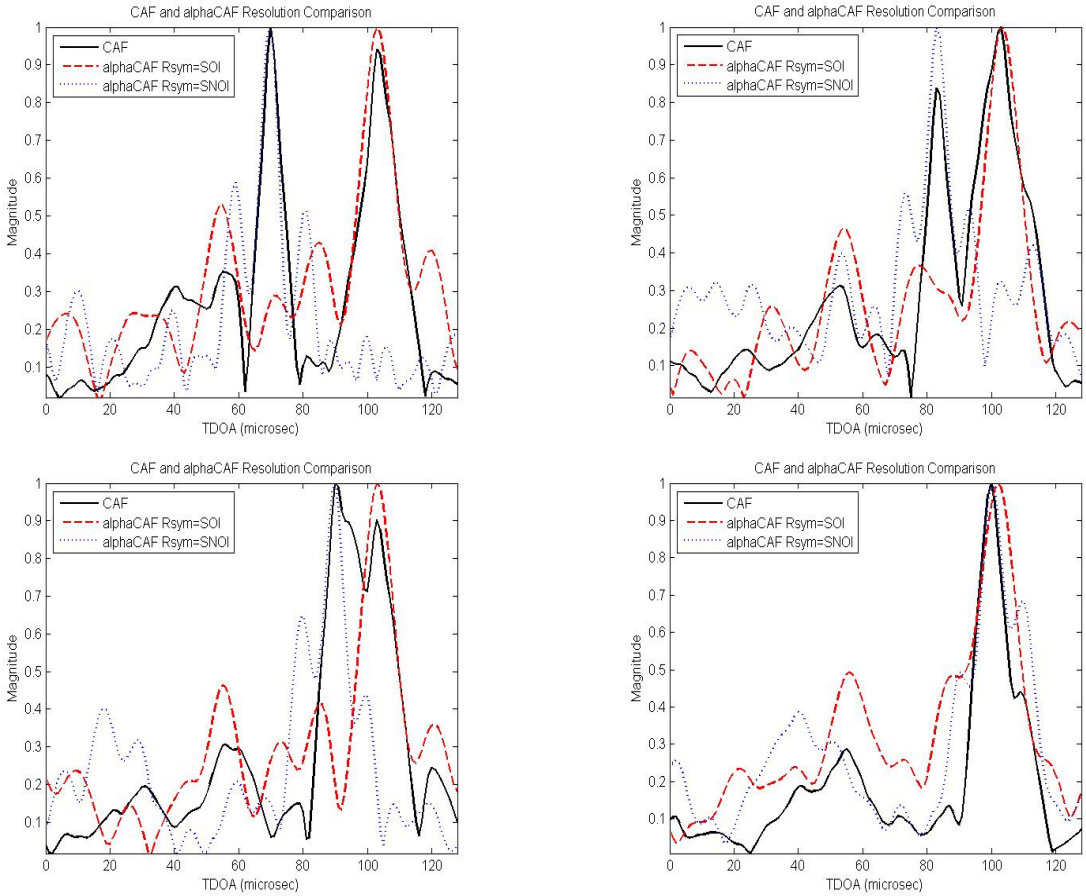

Figure 6.1: Demonstration of *alpha*CAF resolution performance compared to the conventional CAF using a data record length of 2048 samples at a sample rate of 1MHz. The TDOA difference between the SOI and SNOI varies from large to small starting at the top left plot, getting smaller from left to right.

Figure 6.4 shows the same analysis as Figure 6.2, but with a longer data record length of 8192 samples. It is easy to see that as predicted by theory, the FDOA peak became narrower as the observation length increased. Both the conventional CAF and *alpha*CAF FDOA resolutions scale similarly with increased data record size. With a longer data record the conventional CAF was able to separate the SOI and SNOI peaks in every plot. However, if the SNOI FDOA had been simulated to be even closer to the SOI FDOA, then there would have been a point at which the conventional CAF would have only produced a single peak.

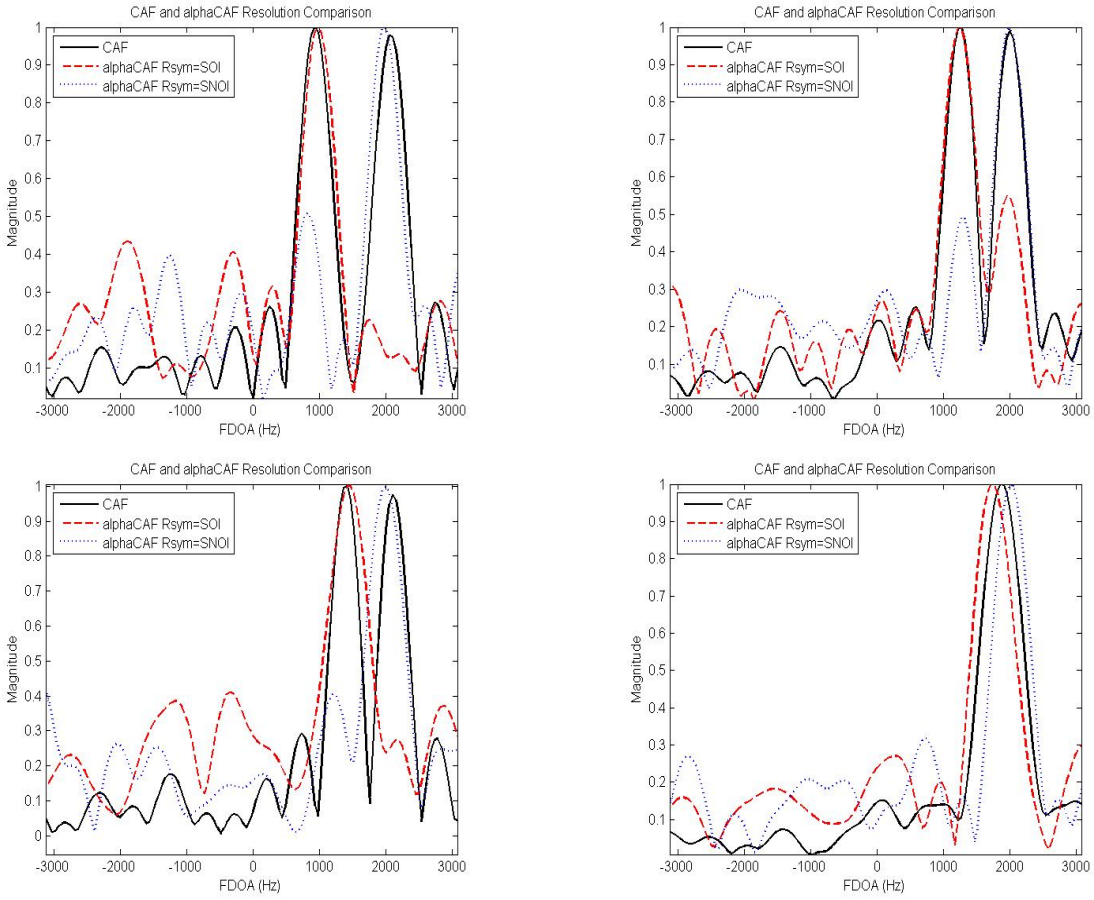

Figure 6.2: Demonstration of *alpha*CAF resolution performance compared to the conventional CAF using a data record length of 2048 samples at a sample rate of 1 MHz. The FDOA difference between the SOI and SNOI varies from 1000 Hz to 250 Hz starting at the top left plot, getting smaller from left to right.

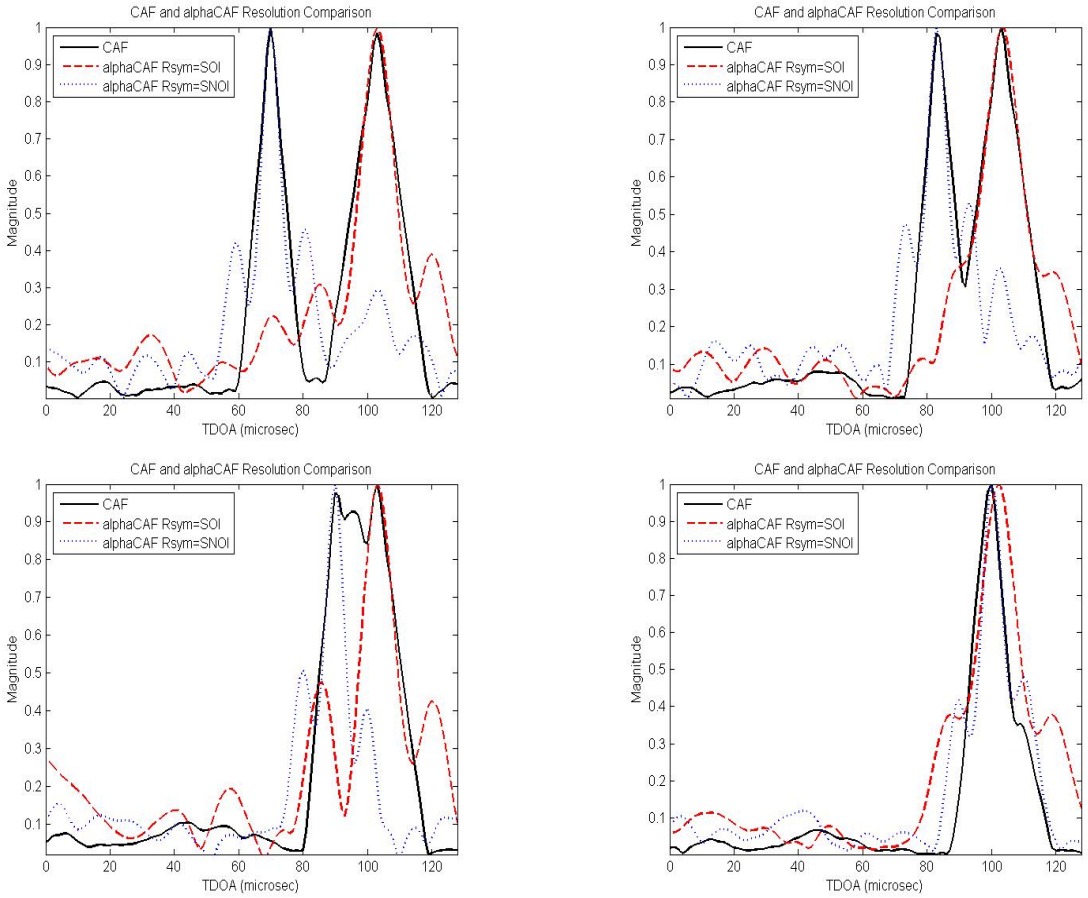

Figure 6.3: Demonstration of *alpha*CAF resolution performance compared to conventional CAF using data record length of 2048 samples at 1MHz sample rate. The TDOA difference between the SOI and SNOI goes from large to small starting at the top left plot, getting smaller from left to right.

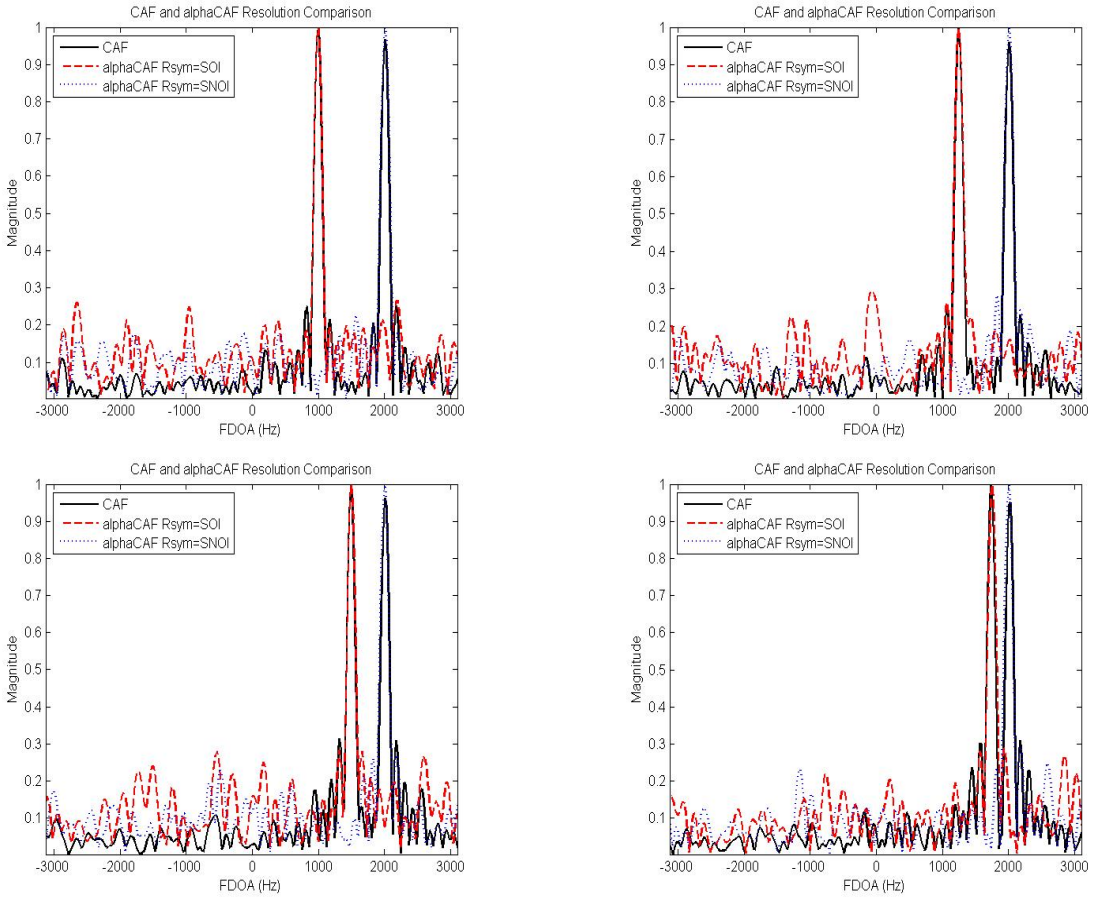

Figure 6.4: Demonstration of *alpha*CAF resolution performance compared to the conventional CAF using a data record length of 8192 samples at a sample rate of 1 MHz. The FDOA difference between the SOI and SNOI varies from 1000 Hz to 250 Hz starting at the top left plot, getting smaller from left to right.

6.2 Symbol Rate Dependencies

It is worth considering how the *alpha*CAF method is affected by the difference in symbol rate between the SOI and SNOI signals. In other words, how well does the *alpha*CAF method separate signals that have similar symbol rates? Figure 6.6 shows two plots similar to the plots shown in the previous section for resolution assessment. Each plot consists of overlaid cross-section plots from a conventional CAF surface and two *alpha*CAF surfaces computed using the SOI and SNOI symbol rates. For each plot the SOI and SNOI TDOAs were simulated to be large enough that the conventional CAF could easily separate the individual signal correlation peaks. For each plot the SOI symbol rate was fixed to the standard value listed in Table 2.2. The symbol rate for the SNOI was varied. Both the SOI and SNOI modulations were BPSK. For the top plot the SNOI symbol rate was selected to be 5 percent less than the SOI symbol rate. The middle plot shows the results when the SOI and SNOI have symbol rates that are equal. Obviously, in this scenario the *alpha*CAF method is reduced to the conventional CAF method and separation of the signals in the cyclic frequency domain is not possible. In the bottom plot the SNOI symbol rate was selected to be 5 percent greater than the SOI symbol rate. Again, the *alpha*CAF method separates the individual signal peaks. This demonstrates that even when the SOI and SNOI symbol rates are only a few percent different the *alpha*CAF method can make reliable estimates.

The *alpha*CAF outputs do show higher amplitude side lobes around the main peaks than the conventional CAF exhibits. The same thing can be seen in the conventional cyclostationary TDOA algorithms introduced in Chapter 3, and does not seem to be unique to the *alpha*CAF algorithm.

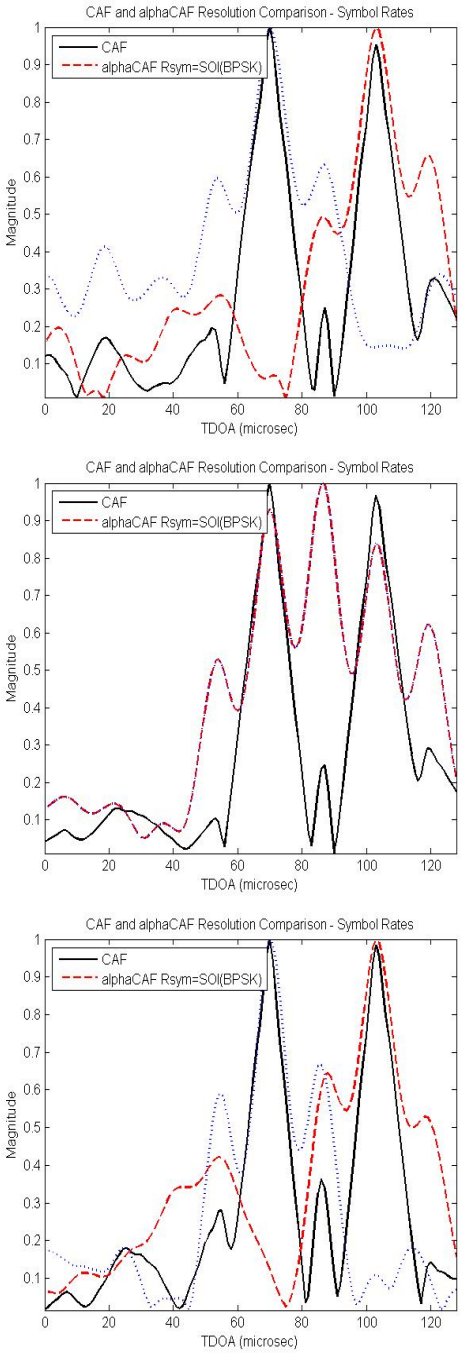

Figure 6.5: Demonstration of *alpha*CAF resolution performance compared to conventional CAF using data record length of 4096 samples at 1 MHz sample rate. The TDOA difference between the SOI and SNOI is fixed to be large enough that the CAF method can easily generate separate peaks . The SOI symbol rate is fixed at 16/256 the sample rate. The SNOI symbol rate is shown for $15.2/256fs$, $16/256fs$, $16.8/256fs$ from top to bottom respectively.

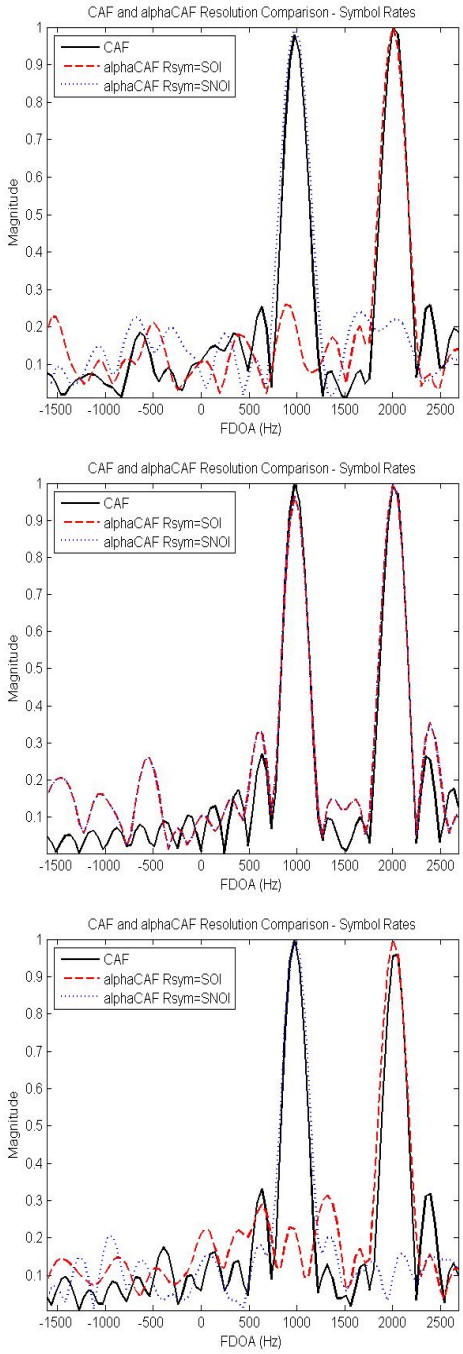

Figure 6.6: Demonstration of *alpha*CAF resolution performance compared to conventional CAF using data record length of 4096 samples at 1 MHz sample rate. The FDOA difference between the SOI and SNOI is fixed to be large enough that the CAF method can easily generate separate peaks. The SOI symbol rate is fixed at 16/256 the sample rate. The SNOI symbol rate is shown for $15.2/256fs$, $16/256fs$, $16.8/256fs$ from top to bottom respectively.

6.3 Detection and Estimation

It was mentioned earlier that the CAF surface can be used as a detection statistic to detect the presence of a SOI before estimating the TDOA and FDOA parameters for geolocation. The same principle applies with the *alpha*CAF surface. To further determine the detection and estimation capabilities of the *alpha*CAF method, *Monte Carlo testing* (MCT) was performed. The MCT provided a numerical measure of the performance of the *alpha*CAF and provided a means for direct comparison to the CAF performance under identical scenarios. The testing also provided a means for comparison to the stationary *Cramer Rao lower bound* (CRLB), which consists of (2.36) and (2.37). Although the CRLB stated here applies to the conventional CAF and not necessarily *alpha*CAF, it will be used anyway since the objective is to compare *alpha*CAF to the performance of the conventional CAF.

One of the first things to consider in designing the MCT is the number of trials needed per test case. In order to determine this number, the stability of the estimates was measured by averaging the error results over the trails. The cumulative sum of the squared errors in the TDOA and FDOA estimates was used as the metric, computed by

$$SE_{TDOA}(sec) = \frac{1}{L}\sum_{l=1}^{L}(D - \hat{D}_l)^2 \tag{6.1}$$

$$SE_{FDOA}(Hz) = \frac{1}{L}\sum_{l=1}^{L}(f_d - \hat{d}_{d_l})^2 \ . \tag{6.2}$$

Another common rule-of-thumb is to use a factor of 100 more trials than the precision, $10^{(-x)}$, desired. For example, if the desired precision is 1 decimal place, then $10^{(1+2)}$, or 1000 trials are needed. Figure 6.7 displays the TDOA stability plot from computing the cumulative sum of the squared error over the trial number as a function of the trial

number. An adequate number of trials would produce a small variation in the result. It is easy to see from the plot that stability occurs just before 1000 trials. Thus, it was concluded that 1 decimal place in precision was adequate, and 1000 trials was necessary for each computational stage in the MCT. Figure 6.8 displays the stability plot for the FDOA estimates. Although the FDOA stability was better than the TDOA stability with fewer trials, it was decided to use 1000 trials for the FDOA MCT also in order to achieve the desired precision.

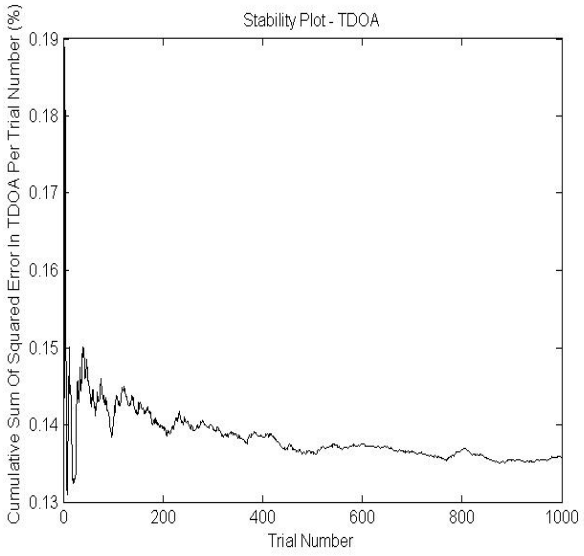

Figure 6.7: TDOA Stability plot for *alpha*CAF using data record length of 2048 samples at 1 MHz sample rate. Test environment A was used and 1000 trials computed for an SIR = 0 dB.

Once the appropriate number of trials was determined, MCT was used to produce a quantitative measure of the *alpha*CAF performance as a function of data record length. For this analysis each trial produced an *alpha*CAF surface and cross-section plots through the surface in the TDOA and FDOA dimensions. From the cross-section plots, the TDOA and FDOA measurements were made. The error in the estimates was computed using knowledge of the true TDOA and FDOA values. The same analysis was done using the conventional CAF method. For each data record length the errors from

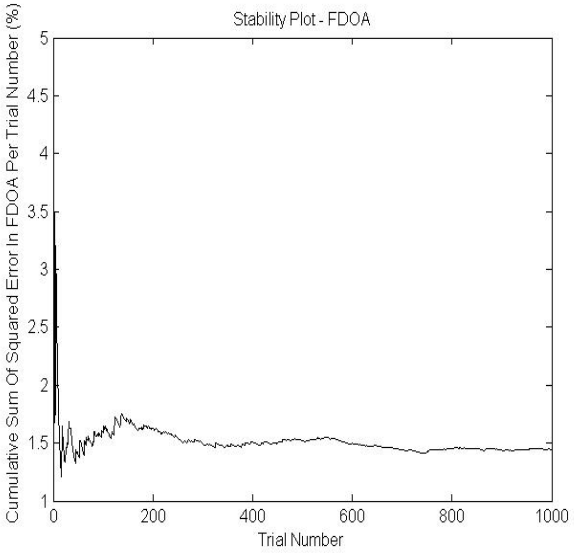

Figure 6.8: FDOA Stability plot for *alpha*CAF using data record length of 2048 samples at 1 MHz sample rate. Test environment A was used and 1000 trials computed for an SIR = 0 dB.

the 1000 trials were used to compute the *root mean squared error* (RMSE) using

$$RMSE_{TDOA}(sec, dB) = 20\log_{10}\left[\frac{1}{L}\sum_{l=1}^{L}(D-\hat{D}_l)^2\right]^{1/2} \tag{6.3}$$

$$RMSE_{FDOA}(Hz, dB) = 20\log_{10}\left[\frac{1}{L}\sum_{l=1}^{L}(f_d-\hat{d}_{d_l})^2\right]^{1/2} \tag{6.4}$$

where L is the number of trials and D and f_d are the actual TDOA and FDOA respectively, and $\hat{D}$ and $\hat{f}_d$ are the estimated TDOA and FDOA respectively.

In Figure 6.9, the TDOA estimation performance of the *alpha*CAF method was compared to the conventional CAF and CRLB for a SOI only scenario. The SOI parameters used are listed in Table 2.2.

The MCT results suggests that for the SOI-only scenario the conventional CAF method produces better estimates than the *alpha*CAF method for short data record

lengths. However, as the data record length gets larger than 2048 samples the *alpha*CAF approaches the performance level of the conventional CAF. For TDOA estimation both methods approach the CRLB as the data record length increases. The FDOA estimation shows a similar performance difference compared to the CAF and CRLB. In general, the *alpha*CAF starts to perform as well as the conventional CAF as data record lengths get larger than 4096 samples.

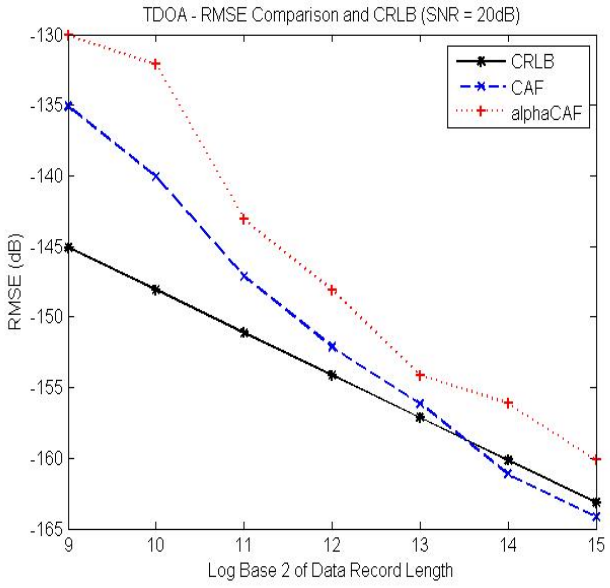

Figure 6.9: SOI only TDOA estimate RMSE versus data record length computed using 1000 trials for each record length and an SNR = 20 dB at both receivers.

After setting a baseline for the conventional CAF and *alpha*CAF performance in an SOI-only scenario, the same MCT using test environment A was performed. Recall that his environment consisted of both a SOI and SNOI. However, for this test the location of the SNOI emitter was moved far enough away from the SOI emitter so that the conventional CAF could produce two distinct peaks in the TDOA/FDOA surface. Figure 6.11 shows the TDOA estimation performance for test environment A of the *alpha*CAF method compared to the conventional CAF and CRLB. It is easy to see that there is an overall degradation of the performance of the conventional CAF for this scenario as

compared to the SOI only scenario in Figure 6.9. The degradation seems to get more pronounced at longer data record lengths. There is little degradation in the *alpha*CAF TDOA estimation performance. In fact, the *alpha*CAF performs better at longer data record lengths than the conventional CAF for test environment A. This demonstrates that the *alpha*CAF method can be used when severe co-channel interference is a problem. Figure 6.12 shows the FDOA estimation performance for test environment A of the *alpha*CAF method compared to the conventional CAF and CRLB. Again, there is a overall degradation of the performance of the conventional CAF compared to the SOI baseline. The *alpha*CAF shows very little degradation due to the SNOI interference. Similar to the TDOA performance for test environment A, the *alpha*CAF FDOA estimation performance exceeds the conventional CAF performance for long data records.

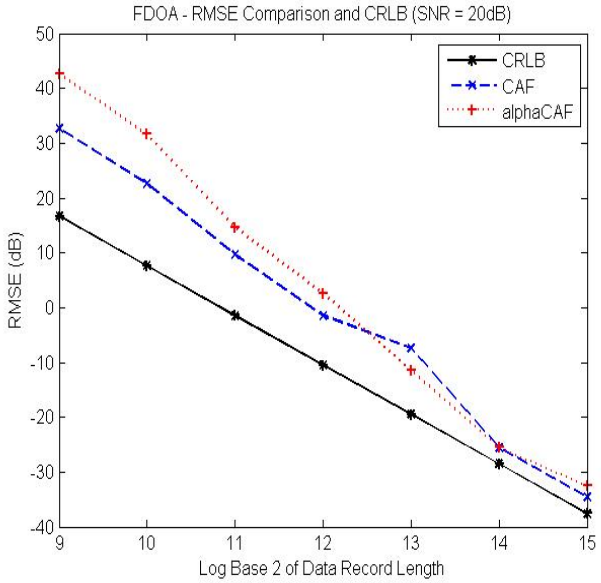

Figure 6.10: SOI only FDOA estimate RMSE versus data record length computed using 1000 trials for each record length and an SNR = 20 dB at both receivers.

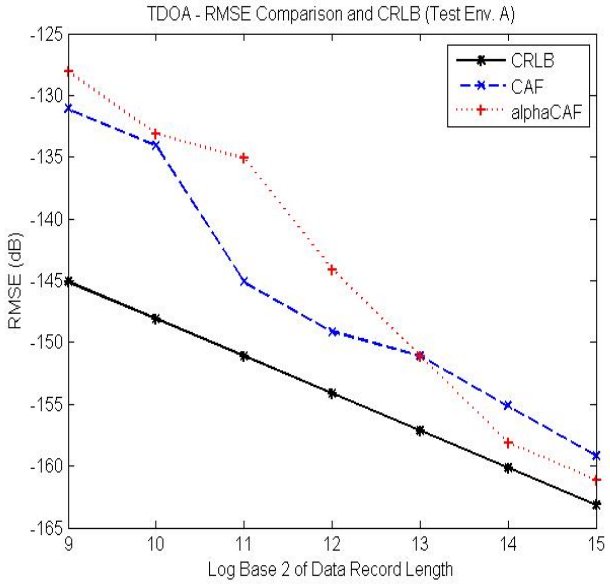

Figure 6.11: SOI TDOA estimate RMSE versus data record length computed using 1000 trials for each record length and for test environment A. SIR = 0 dB at both receivers.

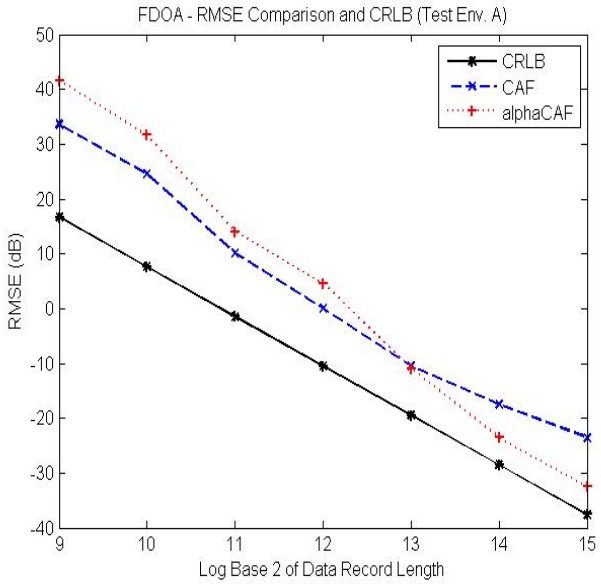

Figure 6.12: SOI FDOA estimate RMSE versus data record length computed using 1000 trials for each record length and for test environment A. SIR = 0 dB at both receivers.

6.4 Parameter Separation

The most difficult scenario in which to estimate TDOA and FDOA is not just a co-channel interference environment, but an environment where the SOI and SNOI emitters are located spatially such that the SOI and SNOI TDOA and/or FDOA peaks cannot be resolved in the CAF surface. It was demonstrated in previous sections of this thesis that this causes the TDOA and/or FDOA estimates to be biased. This problem can be visualized using MCT. Figure 6.13 shows the results of MCT for a fixed data record length of 4096 samples, but as a function of TDOA difference between the SOI and SNOI. The TDOA difference is a result of moving the SNOI emitter increasingly closer to the SOI emitter. Figure 6.13 shows that the conventional CAF performs as expected until the TDOA difference between the SOI and SNOI becomes less than the CAF resolution spacing. At that point, the performance degrades dramatically as the estimator produces biased results due to the SNOI. On the other hand, the *alpha*CAF method only produces a single peak for the SOI by exploiting the different symbol rates of the SOI and SNOI. It continues to produce good estimates as the TDOA difference becomes less than the conventional CAF resolution size.

Figure 6.14 shows the results of the MCT as a function of FDOA difference between the SOI and SNOI. The FDOA difference is a function of the two collection platform velocity vectors and the center frequencies of the SOI and SNOI. Therefore, when the SOI and SNOI emitters are spatially close together FDOA is primarily influenced by the signal parameters. For the MCT results shown in Figure 6.14 the TDOA was fixed and the FDOA adjusted by frequency translating the SNOI center frequency relative to the SOI center frequency. Again, the plot shows that the conventional CAF method starts to degrade dramatically when the FDOA difference becomes less than the FDOA resolution size. However, the *alpha*CAF method continues to produce good estimates

regardless of the FDOA difference.

Figures 6.13 and 6.14 present compelling evidence that when co-channel emitters are encountered in a geolocation application it can be very advantageous to use the *alpha*CAF method for estimating TDOA and FDOA instead of the conventional CAF method. This will be demonstrated further in a simulated geolocation example in Chapter 7.

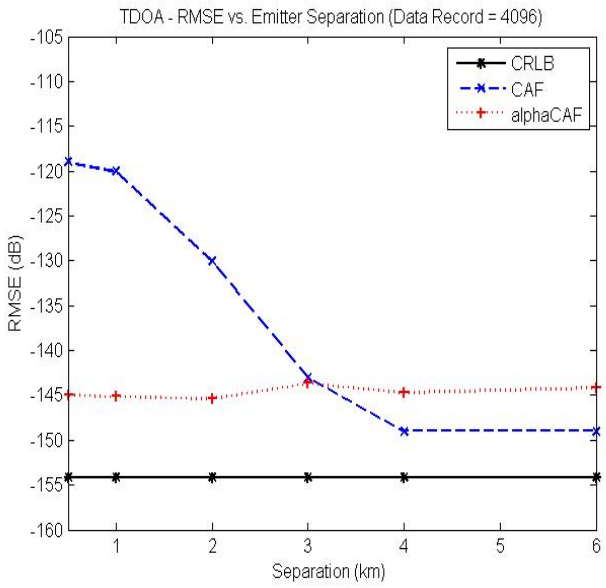

Figure 6.13: TDOA estimate RMSE versus TDOA separation for SOI and SNOI scenario computed using 1000 trials for each record length and an SIR = 0 dB at both receivers.

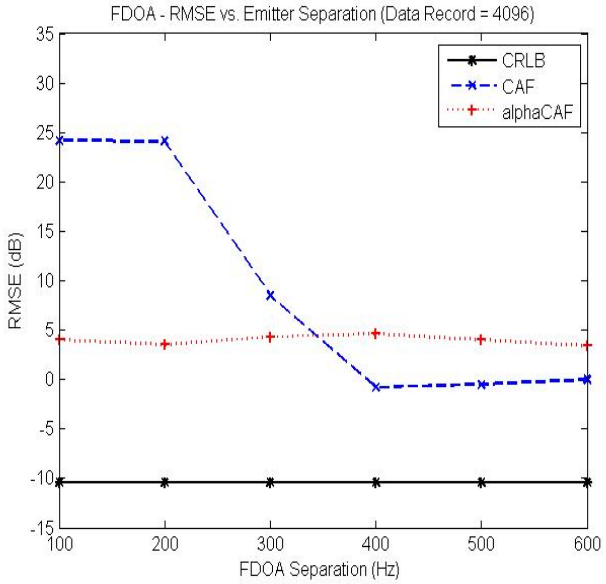

Figure 6.14: FDOA estimate RMSE versus FDOA separation for SOI and SNOI scenario computed using 1000 trials for each record length and an SIR = 0 dB at both receivers.

6.5 Modulation Types

So far, only BPSK signals for both the SOI and SNOI have been considered. In modern complex signal environments there will be many different signals present with various unique modulations. Therefore, the *alpha*CAF method has been tested using a mixture of simulated modulation types. This was done to determine how well the *alpha*CAF method can separate co-channel signals with disparate modulation types.

Figure 6.15 displays four plots similar to the ones presented in Section 6.1 for the resolution performance analysis. However, the results shown in Figure 6.15 are from a scenario where the SNOI is a *amplitude modulated* (AM) signal instead of a BPSK signal. The parameters of the SNOI were chosen to be comparable to the SNOI listed in Table 2.2. For example, the center frequency is the same. However, the modulation rates are different with the AM signal bandwidth being less than the SOI bandwidth. This is evident in the plots by the peak width in the TDOA dimension for the SNOI being greater than for the SOI. The *alpha*CAF output is only computed for the SOI since the interest is in separating it from the SNOI. It is clear in the plots that the *alpha*CAF method can separate the SOI from the SNOI even though the SNOI is an AM modulated signal instead of a BPSK signal.

Figure 6.16 shows the same analysis for the FDOA dimension. Again, the conventional CAF is not able to separate the SOI from the amplitude modulated SNOI when the FDOA spacing is less than the resolution size. At that point, the conventional CAF produces a biased FDOA estimate due to the interfering signal. In contrast, the *alpha*CAF method separates the SOI and produces a good estimate.

Figure 6.17 displays four plots showing the resolution performance analysis from a scenario in which the SNOI is a *frequency modulated* (FM) signal instead of a BPSK signal. Again, the parameters of the SNOI were chosen to be comparable to the SNOI

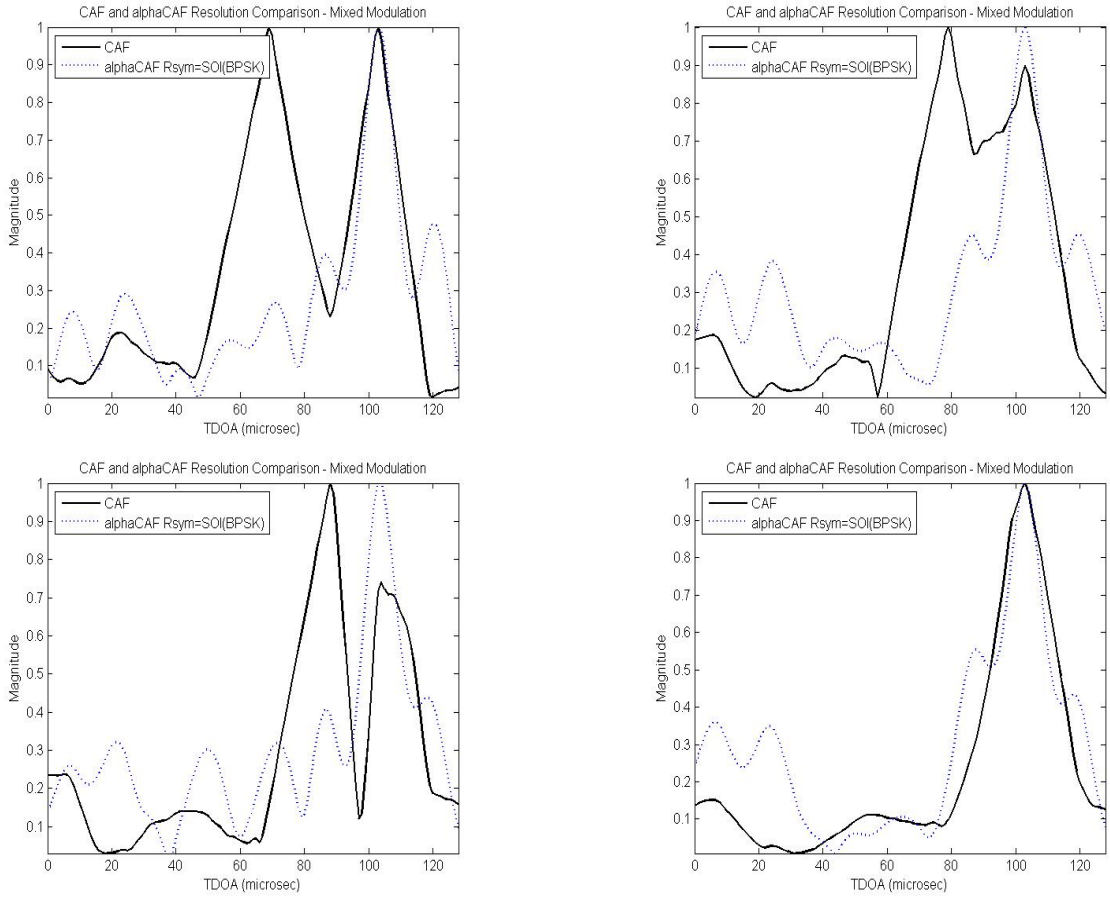

Figure 6.15: Demonstration of *alpha*CAF resolution performance compared to the conventional CAF using *amplitude modulated* (AM) data record length of 2048 samples at a sample rate of 1 MHz. The TDOA difference between the SOI and SNOI varies from large to small starting at the top left plot, getting smaller from left to right.

listed in Table 2.2, with the center frequency being the same but the modulation rates being different. Again, the *alpha*CAF output is only computed for the SOI. Like the previous analysis, the *alpha*CAF method separates the SOI from the SNOI even though the SNOI is an FM signal using random modulation instead of a BPSK signal. This is a further demonstration that the *alpha*CAF method performance is independent of the SNOI modulation type.

Figure 6.18 shows the same analysis for the FDOA dimension. Again, the conventional CAF is not able to separate the SOI from the frequency modulated SNOI when

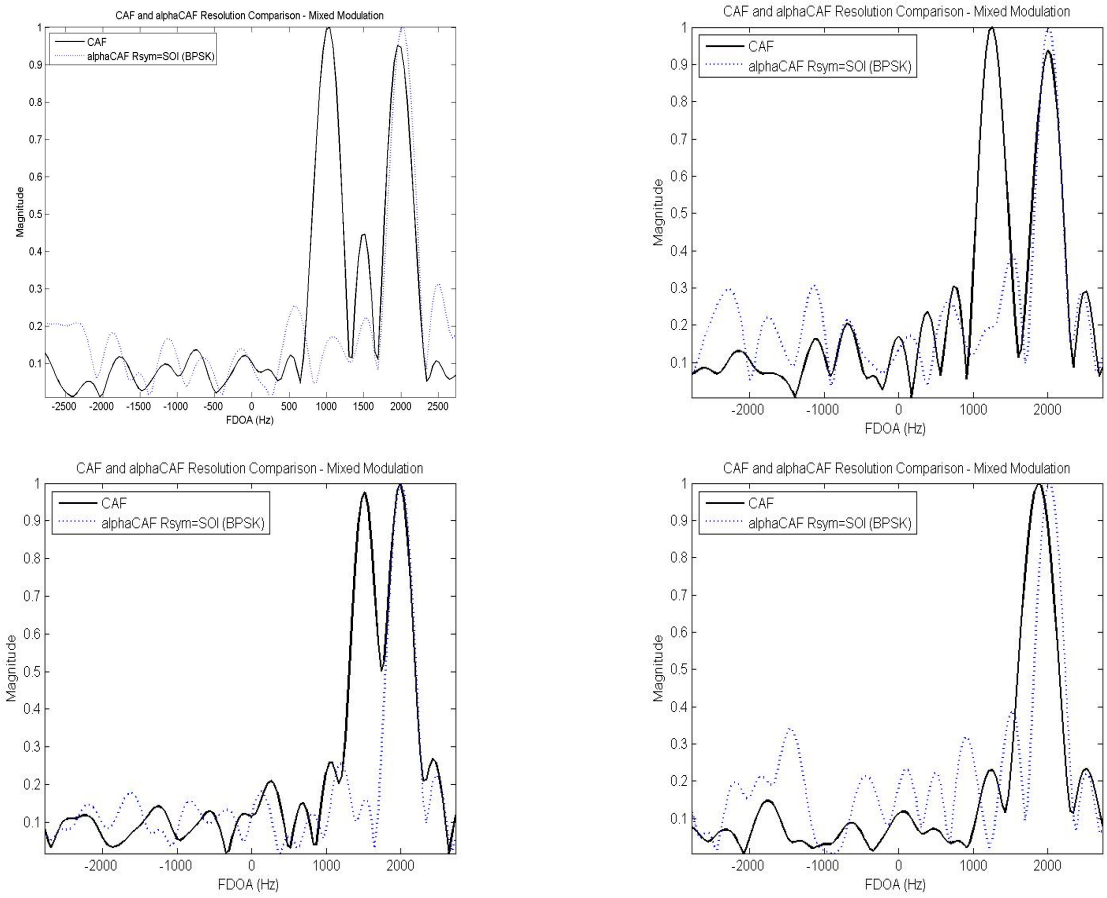

Figure 6.16: Demonstration of *alpha*CAF resolution performance compared to the conventional CAF using *amplitude modulated* (AM) data record length of 2048 samples at a sample rate of 1 MHz. The FDOA difference between the SOI and SNOI varies from 1000 Hz to 250 Hz starting at the top left plot, getting smaller from left to right.

the FDOA spacing is less than the resolution size. The *alpha*CAF method does separate the SOI and produces a good estimate.

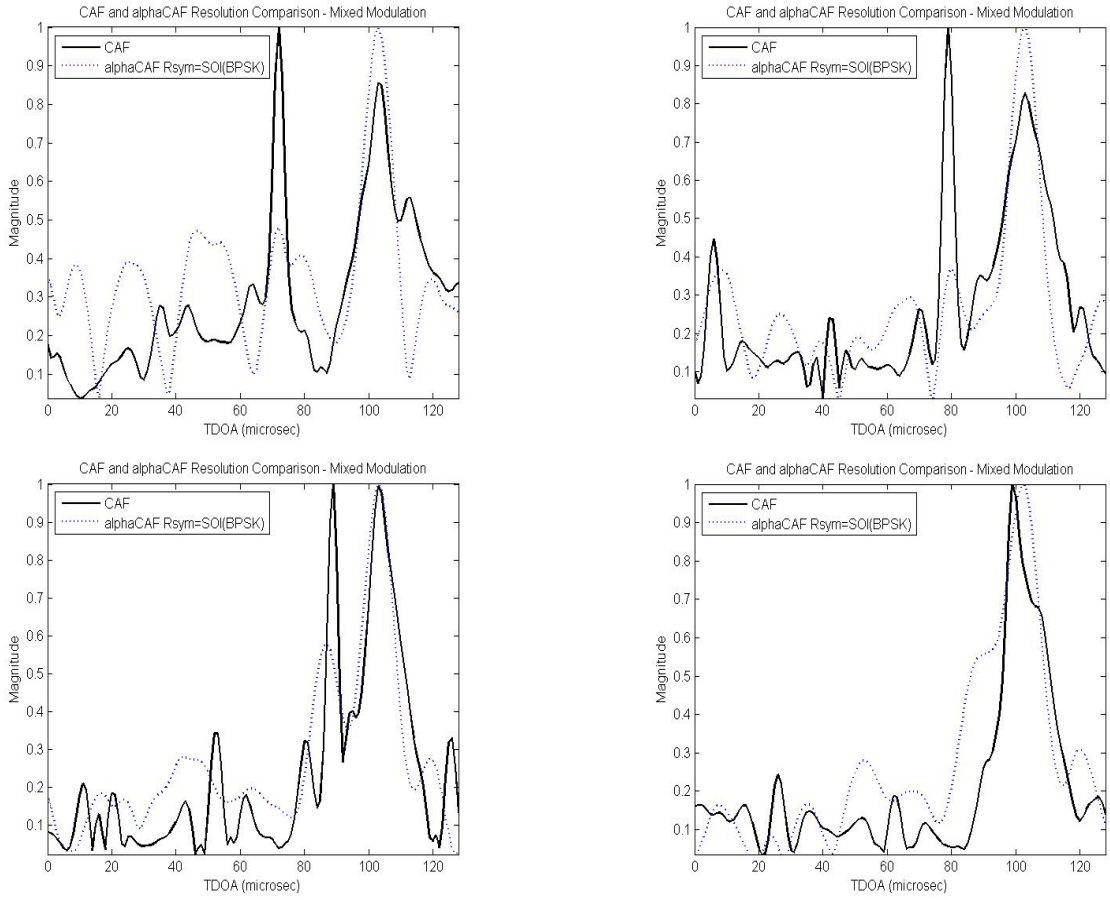

Figure 6.17: Demonstration of *alpha*CAF resolution performance compared to the conventional CAF using *frequency modulated* (FM) signal data record length of 2048 samples at a sample rate of 1 MHz. The TDOA difference between the SOI and SNOI varies from large to small starting at the top left plot, getting smaller from left to right.

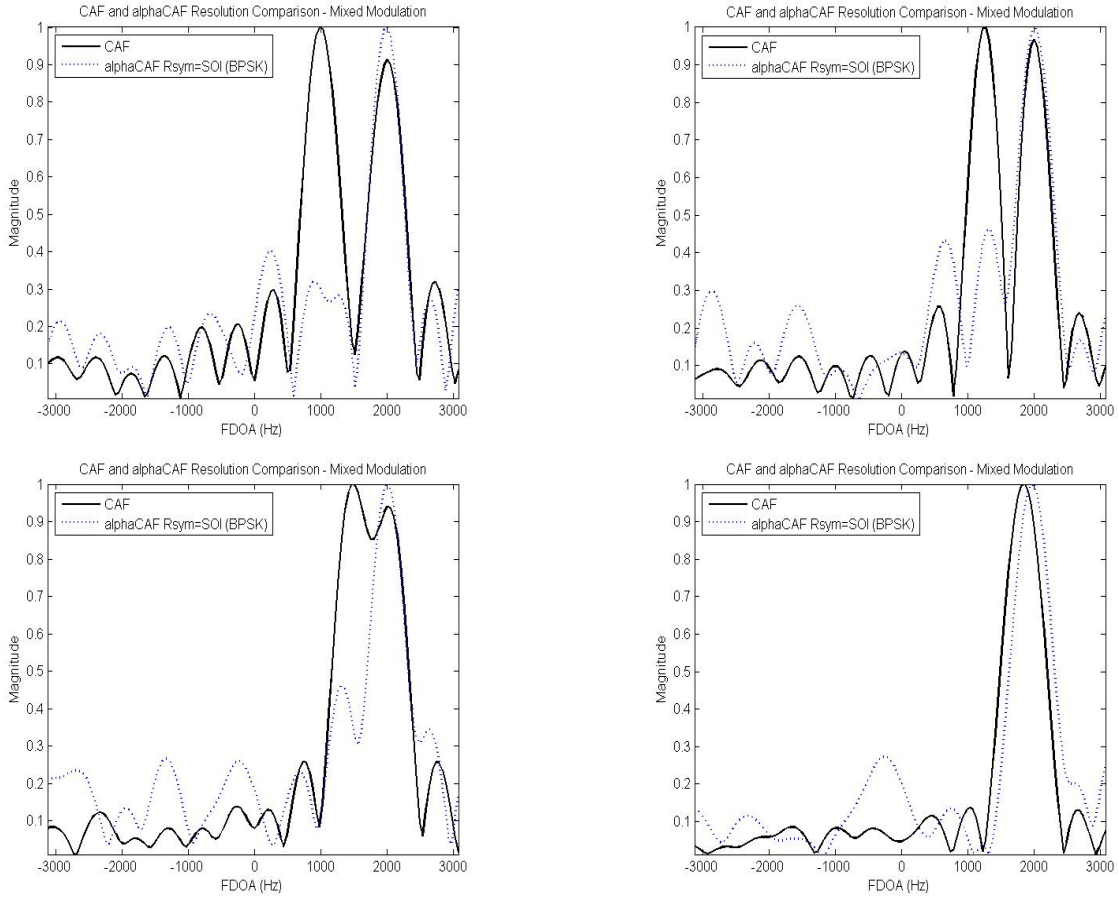

Figure 6.18: Demonstration of *alpha*CAF resolution performance compared to the conventional CAF using *frequency modulated* (FM) data record length of 2048 samples at a sample rate of 1 MHz. The FDOA difference between the SOI and SNOI varies from 1000 Hz to 250 Hz starting at the top left plot, getting smaller from left to right.

Chapter 7 – EMITTER GEOLOCATION

7.1 Historical Review of Emitter Location Methods

Due to the fact that emitter location methods have many applications, they have been intensely studied in the past. Various algorithms and implementations have been developed, and there exists a wide range of literature showcasing work on the topic. Some of the most sophisticated methods for locating emitters use antenna arrays and *direction-of-arrival* (DOA) techniques. However, these techniques are susceptible to array calibration errors and can fail if the number of emitter wavefronts impinging on the array is greater than one-half the number of array antenna elements [20]. For these reasons, methods that locate emitters based on their TDOA and FDOA at multiple collectors are preferred for application where robustness and cost is of primary interest.

The earliest published emitter location methods were applied to the location of ground emitters using stationary land-based receivers [22]. These methods used a combination of *direction finding* (DF) with what is now commonly known as triangulation. One of the earliest algorithms was called Stansfield's algorithm [22]. More recent modifications of the algorithm have been published by Gavish [28]. The concepts behind Stansfield's algorithm were later utilized using TDOA measurements [15]. The concepts were later used in another algorithm called the multilateration algorithm, or hyperbolic algorithm [30].

A novel algorithm based on TDOA measurements was later developed by Schmidt [24] and has proved to be very useful in real applications. The first applications of Stansfield's methods to airborne receiver systems was presented by Ancker [25]. Later, many

airborne methods were introduced [23] that used the simplifying assumption of a flat earth surface and direct path propagation. Since these assumptions introduce significant errors, other methods that did not make these assumptions were later developed.

The problem of locating a target position in 3-D space using range-difference measurements was first described by Lee [30], and the first formulation of the emitter location problem using multiple measurement types (TDOA with AOA, etc.) was presented by Foy [27] to locate emitters on a plane. A general method of emitter location in 3-D space using multiple measurement types was published by Wax [31]. Later, methods using FDOA were developed and published by Chestnut [32] and Chan and Towers [26].

In general, all of the most popular emitter location algorithms cited above depend on the measurements of TDOA and/or FDOA from a collected signal. With the increase in wireless communications technology around the world and the increased use of the radio spectrum, obtaining reliable TDOA and FDOA parameter estimates can be difficult. In order for the emitter location algorithms to give reliable results as the RF spectrum becomes more heavily used, methods for estimating TDOA and FDOA that are tolerant to co-channel interference become increasingly important. In the next section one of the most practical emitter location algorithms will be explained.

7.2 Conventional Geolocation

To determine the location estimate of an emitter in n-dimensions, it is necessary to have n or more TDOA or FDOA measurements. Usually it is best to have more than n measurements so that the geolocation problem is over-determined (more estimates than location parameters to be evaluated). This also increases the accuracy of the location estimate.

A measurement is used to find a line or surface of constant TDOA or FDOA on

which the emitter is estimated to be located. In real three-dimensional space this line is a curve on the surface of the earth. Two measurements will provide two lines or surfaces, and the intersection of the lines or surfaces provides an estimate of the emitter location. Since the measurements are subject to various types of errors, the line can be considered a random variable. The variances of the lines can be used to generate an error estimate contained within an error ellipse, to represent the accuracy of the estimate for emitter location.

In order to demonstrate these concepts further, TDOA-only measurements will be considered first. If two spatially separated time-synchronized receivers exist, then the range difference for the two receivers can be expressed as

$$\tau = \frac{(R_2 - R_1)}{c} \tag{7.1}$$

where τ is the TDOA, R_1 and R_2 are the ranges from the emitter to the receivers, and c is the speed of propagation. For a given value of TDOA, this equation represents a hyperboloid of revolution on which the emitter lies [32]. For example, if the emitter is located on the surface of the earth, then the intersection of this hyperboloid and the earth surface is a curve on which the emitter is located. Using one more estimated TDOA or FDOA values, the intersection of two curves will give the emitter location estimate.

A measurement of FDOA can also be used to locate an emitter. FDOA is the difference in frequency of the received signal at two spatially separated receivers, or the change in range difference as a function of time. An FDOA measurement is a result of exploiting receiver motion. Therefore, at least one of the receivers must be moving for a measurement to be possible. Also, the greater the relative motion, the better the FDOA measurement possible.

A signal received by a moving receiver (assuming a stationary emitter) will have a different observed frequency than the emitter's transmitted frequency due to Doppler shift. If the signal is collected over a time T, then the average observed frequency over the collection time is

$$f_{average} = f_c - (R_{1e} - R_{1b})/\lambda T \tag{7.2}$$

where f_c is the center frequency transmitted by the emitter, λ is the wavelength, and R_{1b} and R_{1e} are the ranges from the emitter to the first receiver at the beginning and end of the collection interval. Therefore, a measurement of this average frequency provides a measurement of the change in range over the collection interval. This is similar to a TDOA measurement, but with the two receiver locations corresponding to the receiver locations at the beginning time and the end time of the collection. Since the emitter's transmitted frequency is not known, the difference of the average frequency measured from spatially separated receivers is used. The resulting FDOA measurement represents the difference between changes of range of two receivers and does not depend on the actual transmitted frequency. This information provides a surface in space on which the receiver must be located. By using two or more FDOA measurements, the emitter's location can be estimated. Note, that two receivers can obtain one TDOA measurement and one FDOA measurement and can estimate the emitter's location without the use of additional receivers. Figure 7.1 shows a diagram depicting the concept of a line of constant TDOA on the surface of the earth. Figure 7.2 shows the more conceptually complicated lines of constant FDOA. When using both TDOA and FDOA measurements, the intersection of the TDOA line and the FDOA line on the surface of the earth provides the emitter location estimate. Figure 7.3 shows this concept with a single line of constant TDOA and a single line of FDOA.

Using the average frequency observed by two receivers over the collection interval,

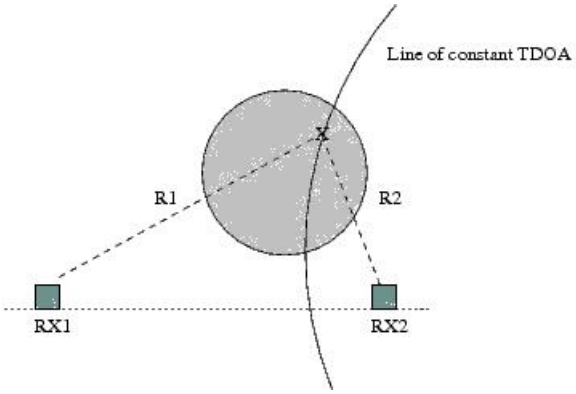

Figure 7.1: Illustration of constant line of TDOA on the surface of the earth from two receivers on a baseline.

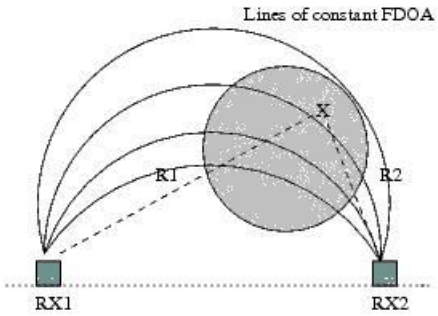

Figure 7.2: Illustration of constant lines of FDOA on the surface of the earth from two receivers moving on the same baseline.

FDOA is expressed by

$$FDOA = f_1 - f2 = \left(\frac{f_c}{cT}\right)(R_{2e} - R_{2b} - R_{1e} - R_{1b}) \tag{7.3}$$

where again the subscripts indicate which receiver is being referenced and whether it is at the beginning or end of the collection interval. Equation (7.3) defines a surface in space on which the emitter must be located [32]. Analogous to TDOA, using two FDOA measurements from separate collector pairs will give two surfaces. The intersection of the two surfaces gives the emitter location estimate.

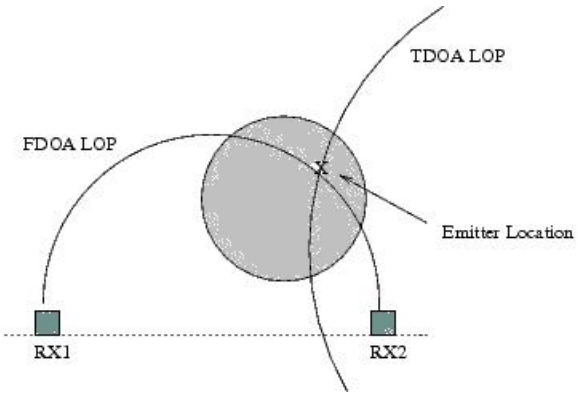

Figure 7.3: Illustration of constant line of TDOA, or line of position (LOP), and line of constant FDOA crossing on the surface of the earth. The crossing point is the location estimate of the emitter.

The TDOA and/or FDOA measurements can be made using one of the estimation methods introduced in earlier chapters. Usually these measurements are made for a given collection *snapshot*, or data record. The measurements are passed to a geolocation algorithm that computes the emitter location estimate. One of the most popular geolocation algorithms is the Newton-Raphson method. This method will be explained in the next, along with how it is used to compute location estimates from TDOA and FDOA measurements.

7.2.1 Newton-Raphson Method of Geolocation

The Newton-Raphson method is a technique that numerically approximates the root of an equation. It is an iterative process that follows a set of guidelines to approximate one or two roots of a function using its derivative and initial estimates of the roots. The Newton-Raphson method can compute location estimates using only TDOA measurements or both TDOA and FDOA measurements. Error sources such as system bias can also be input into the computations. Next, is a simple example to show how this method

works.

If a pair of collection receivers (See Figure 2.2) makes a measurement for an emitter at position $\mathbf{p} = [x\ y]^T$, the measurements, $\mathbf{m}$, can be related to the emitter position and receiver positions and velocities, $\mathbf{w}$, by the unspecified kinematics-based function

$$\mathbf{m} = F\left(x, y, \mathbf{w}\right) \ . \tag{7.4}$$

To solve the geolocation problem the measurements $\mathbf{m}$ and known receiver kinematic parameters $\mathbf{w}$ are used to find the emitter coordinates. At first glance, this seems like a simple least squares problem where the goal is to solve the inverse problem and find the relationship in (7.4), and solve for the parameter vector $\mathbf{w}$. However, it turns out that the right side of (7.4) is a non-linear function and therefore, not invertible. For this type of problem the Newton-Raphson method excels [16].

The first step in using the Newton-Raphson method to solve (7.4) is to linearize the nonlinear function by expanding it into the first few terms of its Taylor series approximation around an initial guess of the emitter position, $\mathbf{p_0}$. This approximation gives us

$$\mathbf{m} = F(\mathbf{p}) \approx F(\mathbf{p}_0) + (\mathbf{p} - \mathbf{p}_0)^T \nabla F(\mathbf{p}_0) + \frac{1}{2}(\mathbf{p} - \mathbf{p}_0)^T \nabla\nabla F(\mathbf{p}_0)(\mathbf{p} - \mathbf{p}_0) \tag{7.5}$$

where the gradient of $F(\mathbf{p})$ is given by

$$\nabla F(\mathbf{p}) = \begin{bmatrix} \frac{\partial F(\mathbf{p})}{\partial x} \\ \frac{\partial F(\mathbf{p})}{\partial y} \end{bmatrix} \tag{7.6}$$

and $\nabla\nabla F(\mathbf{p})$ is the Hessian of $F(\mathbf{p})$ given by

$$\nabla\nabla F(\mathbf{p}) = \begin{bmatrix} \frac{\partial^2 F(\mathbf{p})}{\partial x^2} & \frac{\partial F(\mathbf{p})}{\partial x \partial y} \\ \frac{\partial F(\mathbf{p})}{\partial y \partial x} & \frac{\partial^2 F(\mathbf{p})}{\partial y^2} \end{bmatrix} . \tag{7.7}$$

Now, after differentiating (7.5) with respect to $\mathbf{p}$ and setting it equal to zero, $\mathbf{p}$ can be solved for to get

$$\mathbf{p} = \mathbf{p}_0 - \left[\nabla\nabla F(\mathbf{p}_0)\right]^{-1} \nabla F(\mathbf{p}_0) , \tag{7.8}$$

which can be written into the form of an iterative technique to search for the position estimate that minimizes $F(\mathbf{p})$ by

$$\mathbf{p}_{k+1} = \mathbf{p}_k - \left[\nabla\nabla F(\mathbf{p}_k)\right]^{-1} \nabla F(\mathbf{p}_k) . \tag{7.9}$$

Now, if $F(\mathbf{p})$ represents a weighted squared error function, the weighted least squares iteration can be expressed as [16]

$$\mathbf{p}_{k+1} = \mathbf{p}_k - \left[\mathbf{J}^T\mathbf{W}\mathbf{J}\right]^{-1} \mathbf{J}^T\mathbf{W}\mathbf{e}(\mathbf{p}_k)) \tag{7.10}$$

where in the case of two measurements and two-dimensions, $\mathbf{W}$ is a 2×2 weighting matrix and $\mathbf{J}$ is the 2×2 Jacobian of $\mathbf{e}(\mathbf{p})$. Note, that $\mathbf{e}(\mathbf{p})$ is the prediction error vector given by

$$\mathbf{e}(\mathbf{p}) = \mathbf{h}(\mathbf{p}) - \mathbf{m} \tag{7.11}$$

where $\mathbf{h}(\mathbf{p})$ is a vector of measurement predictions for a given $\mathbf{p}$. The known receiver positions and velocities, along with the collection geometry model, are used to predict the measured TDOA and FDOA values.

Now, (7.10) can be expressed in a more compact form as

$$\Delta \mathbf{m} \approx \mathbf{A} \Delta \mathbf{p} \tag{7.12}$$

where $\mathbf{A}$ is the pseudo-inverse from (7.10) with partial derivatives of a function that relates the TDOA and FDOA measurements to the emitter position. For reference, Appendix A derives the relationship between TDOA/FDOA and the emitter position in greater detail.

Let the positions and the velocities of the collection receivers be denoted by $\mathbf{p}_1$, $\mathbf{p}_2$, and $\mathbf{v}_1$, $\mathbf{v}_2$, respectively. The unknown emitter location $\mathbf{p}$ is assumed to be stationary. Unit vectors pointing from the unknown emitter position to the two receiver positions can be formed by

$$\mathbf{u}_1 = \frac{\mathbf{p}_1 - \mathbf{p}}{|\mathbf{p}_1 - \mathbf{p}|} \tag{7.13}$$

$$\mathbf{u}_2 = \frac{\mathbf{p}_2 - \mathbf{p}}{|\mathbf{p}_2 - \mathbf{p}|} \tag{7.14}$$

where $|\bullet|$ represents the vector L2 vector norm. The following expressions relate the TDOA and FDOA parameters to the emitter position using the receiver positions, velocities and the unit vectors from (7.13) and (7.14) above:

$$\mathbf{TDOA} = \frac{1}{c}\left(|\mathbf{p}_2 - \mathbf{p}| - |\mathbf{p}_1 - \mathbf{p}|\right) \tag{7.15}$$

$$\mathbf{FDOA} = \frac{f_c}{c}\left(\mathbf{v}_2^T \mathbf{u}_2 - \mathbf{v}_1^T \mathbf{u}_1\right) \tag{7.16}$$

where c is the speed of light and f_0 is the center frequency of the transmitted signal from the emitter. Taking the partials of (7.13) and (7.14) yields

$$\nabla \mathbf{TDOA} = \frac{1}{c}\left(\mathbf{u}_2 - \mathbf{u}_1\right) \tag{7.17}$$

$$\nabla\mathbf{FDOA} = \frac{f_c}{c}\left(\frac{(\mathbf{I}-\mathbf{u}_2\mathbf{u}_2^T)\mathbf{v}_2}{|\mathbf{p}_2-\mathbf{p}|} - \frac{(\mathbf{I}-\mathbf{u}_1\mathbf{u}_1^T)\mathbf{v}_1}{|\mathbf{p}_1-\mathbf{p}|}\right). \tag{7.18}$$

Equations (7.15) and (7.16) are used to solve for the emitter position estimates.

The weighting or conditioning matrix $\mathbf{W}$ in (7.10) is chosen to account for the differences in quality of the observations, and it is common to make it equal to the inverse of the measurement covariance matrix $\mathbf{M}$

$$\mathbf{W} = \mathbf{M}^{-1} \tag{7.19}$$

where $\mathbf{M}$ can be written as the two-dimensional matrix

$$\mathbf{M} = \begin{bmatrix} \frac{1}{\sigma_1} & 0 \\ 0 & \frac{1}{\sigma_2} \end{bmatrix} \tag{7.20}$$

where σ_1 and σ_2 are error variances that are approximated using

$$\sigma_{TDOA} = \frac{0.55}{B_s}\frac{1}{\sqrt{TB\gamma}} \tag{7.21}$$

$$\sigma_{FDOA} = \frac{0.55}{T}\frac{1}{\sqrt{TB\gamma}} \tag{7.22}$$

where B_s is the signal bandwidth, B is the noise bandwidth, T is the integration time and γ is the effective SNR defined in (2.20). Note that (7.21) and (7.22) are the same relations introduced in Chapter 2 as the TDOA and FDOA CRLBs for the CAF method.

Now everything can be put together into a geolocation algorithm for estimating the position of an emitter. The following is a step-by-step description of the Newton-Raphson geolocation algorithm:

1. Make initial prediction of emitter location $\mathbf{p}_0$ using collection geometry.
2. Compute predicted measurements $\mathbf{h}(\mathbf{p})$ using (7.15) and (7.16).
3. Calculate the prediction error using (7.11).
4. Exit algorithm if residual is small enough.
5. Update position estimate using (7.10).
6. Return to step 2 and repeat.

7.2.2 The Error Ellipse

After calculating the estimate for the emitter's position and the variances that are associated with the estimate, the error ellipse can be computed. Calculating the 95% confidence ellipse is a standard technique and has been explained in [33]. The derivation is not included here, but instead, the results from the liturature are used [16].

The covariance of the position vector can be expressed by

$$cov\mathbf{P} = (\mathbf{J}^T\mathbf{M}^{-1}\mathbf{J})^{-1} = \begin{bmatrix} \sigma_x^2 & \rho\sigma_x\sigma_y \\ \rho\sigma_x\sigma_y & \sigma_y^2 \end{bmatrix} \tag{7.23}$$

where $\mathbf{J}$ is the Jacobian of $e(\mathbf{p})$, and assuming that $cov\mathbf{M}^{-1}$ is symmetric. Note that the lengths of the semi-axes for the error ellipse are the eigenvalues of the covariance matrix and the orientation is determined from its eigenvectors [16]. The diagonal terms in (7.22), σ_x and σ_y, are the variances, and ρ is the correlation coefficient for the parameters x and y. The off-diagonal terms are the covariance for x and y. The terms in (7.22) are used to arrive at the following calculations for the the semi-major and semi-minor axes and the orientation of the error ellipse [33]:

$$(\sigma_a + \sigma_b)^2 \;=\; \sigma_x^2 + \sigma_y^2 + \sigma_x\sigma_y(1-\rho^2) \tag{7.24}$$

$$(\sigma_a - \sigma_b)^2 \;=\; \sigma_x^2 + \sigma_y^2 - \sigma_x\sigma_y(1-\rho^2) \tag{7.25}$$

where σ_a^2 and σ_b^2 are the variances of the contour error ellipse semi-major and semi-minor axes respectively. Note that it is assumed that the errors are independent and normally distributed with zero-mean. The chi-square distribution for the error variances is

$$\frac{a}{\sigma_a}^2 + \frac{b}{\sigma_b}^2 = \chi^2 \; . \tag{7.26}$$

The quantity χ^2 can be found in statistical tables. For a 95% error ellipse, the result is $\chi^2 = 5.991$. Using this with (7.26) to solve for a and b yields $a = 2.448\sigma_a$ and $b = 2.448\sigma_b$.

Figure 7.4 illustrated the error ellipse along with the various parameters used to form it. The error ellipse orientation is given by

$$\theta = \arctan \frac{2\rho\sigma_x\sigma_y}{\sigma_x^2 - \sigma_y^2} \; . \tag{7.27}$$

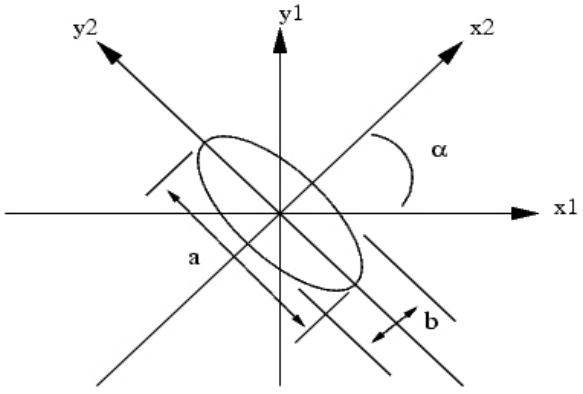

Figure 7.4: Illustration of the error ellipse.

7.3 Geolocation and the *alpha*CAF Method

Now that the performance of the *alpha*CAF method has been established, and a geolocation algorithm introduced, an example of how *alpha*CAF is used in an application to get precise emitter location estimates can be presented. For the example an image from Google Earth showing an airport and some open space along the Columbia River in Oregon was used. The image and its approximate ground dimensions were used to setup a flat earth coordinate system in a Matlab program. A SOI and SNOI were simulated to originate coordinates that correlate with the locations indicated on the image. Note that the SNOI was located at the airport and the SOI was from a lost and injured hiker out in the open space to the image-right of the airport. The hiker location was chosen to be about 1km away from the SNOI source location. Both the SOI and SNOI parameters were the same as those listed in Table 2.2.

Both the conventional CAF and *alpha*CAF were used to estimate TDOA and FDOA for the SOI. The *alpha*CAF used the known SOI symbol rate to compute the two-dimensional surface with the cyclic frequency fixed. The TDOA and FDOA estimates from each method were then passed to the geolocation algorithm presented in the previous section. Since it is not the intention of this dissertation to explore the details of computing the error ellipse, the error ellipse was not actually computed, but was contrived for demonstration purposes.

Figure 7.5 displays the Google aerial image, along with the overlaid SOI and SNOI emitter locations and geolocation estimates computed using the TDOA and FDOA estimates from the conventional CAF method and the *alpha*CAF method. The geolocation estimate computed from the conventional CAF method was inaccurate and missed the hiker by approximetely 0.5 km. This is due to the fact that the TDOA and FDOA estimates passed by the conventional CAF method were biased estimates due to the

SNOI interference. In contrast, the geolocation computed using the TDOA and FDOA estimates from the *alpha*CAF method were fairly accurate. In a real application the *alpha*CAF method would increase the likelihood of locating the lost hiker when co-channel emitters are problematic for conventional methods.

Figure 7.5: Simulated example of geolocation of a lost hiker in a co-channel signal environment using both the conventional CAF method and the new *alpha*CAF method. Computed location estimates are overlaid on an aerial photograph. The actual location of the SNOI emitter is at the airport. The hiker location is marked in the open space to the right of the airport. The computed geolocation results are overlaid on the photograph showing that the conventional CAF method produced biased TDOA and FDOA measurements and therefore an incorrect geolocation. The *alpha*CAF method produced good TDOA and FDOA estimates allowing the hiker to successfully be located.

Chapter 8 – OBSERVATIONS AND CONCLUSIONS

8.1 Comments and Analysis Results

Conclusions can now be made about how the *alpha*CAF method performs compared to the conventional CAF method when estimating TDOA and FDOA for co-channel signals that originate from emitters that are located close together. The advantages of the *alpha*CAF method over the conventional CAF method have been experimentally demonstrated both qualitatively and quantitatively. Although the CAF method can produce estimates when TDOAs differ by more than the reciprocal of the signal bandwidths and FDOAs differ by more than the reciprocal of the collection time, it fails to produce reliable estimates when these conditions do not apply. When an interferer is spatially close to the source of a SOI, the conventional CAF method will generate a biased estimate of the SOI TDOA and FDOA parameters. Depending on the relative strength and bandwidth of the interfering signal, the bias can be significant. A biased estimate for TDOA and/or FDOA will cause the geolocation algorithm to produce incorrect location estimates. Therefore, the *alpha*CAF method for producing separated unbiased TDOA and FDOA measurements in these conditions is a significant contribution. By exploiting the cyclostationary properties of modern communications signals the *alpha*CAF method can produce unbiased estimates when the conventional CAF method fails. The main contribution is the use of one additional exploitable signal parameter, the cyclic frequency, to separate signals previously inseparable by the conventional CAF. As most modern communication signals tend to be bauded digital emissions, cyclostationary properties are frequently exploitable.

8.2 Areas for Further Research

There are several areas related to the work in this dissertation that would be interesting to research further. I have selected a few areas that I believe to be most important and potentially fruitful. The following subsections contain short descriptions and recommendations for each suggested area.

8.2.1 Efficient Computational Methods

The *alpha*CAF method requires the computation of several cyclic spectrums. The computation of the entire cyclic spectrum is considerably more complex and time-consuming than computation of the conventional PSD. Over the past few decades several efficient algorithms for computing the cyclic spectrum have been developed [11]. These algorithms can be divided into two groups: the frequency-smoothing algorithms and the time-smoothing algorithms. In this dissertation the cyclic spectrums were computed without the advantage of these fast computational algorithms. It would be useful to implement the *alpha*CAF method using one of the available computationally efficient algorithms for computing the cyclic spectrums. Research into what effect this has on the estimates would be necessary. Also, instead of just computing the cyclic spectrums using known fast algorithms, a new fast algorithm for computing the entire three-dimensional *alpha*CAF could be developed.

8.2.2 Cyclostationary Hybrid Method

The *hybrid* method introduced in Chapter 2 could be modified to exploit cyclostationary signals. This would likely be another iterative method that would be useful for applications where *alpha*CAF is too computationally demanding. It may also lead

to other parameters being estimated, such as signal bandwidth. However, this method comes at the cost of reduced sensitivity due to breaking up the data record into smaller sub-records during the processing.

8.2.3 Analytical Analysis of *alpha*CAF Bias in Three-Dimensions

In this thesis an experimental approach was taken to determining if the *alpha*CAF method produces unbiased estimates. In order for this to be more substantially proved, an analytical proof would need to be worked out. Along with this effort a CRLB for the *alpha*CAF estimator could also be found. Together these two results would be a substantial contribution.

8.2.4 Additional Modulation Types

There are still many modulation types that could be explored and characterized using the *alpha*CAF method. For example, frequency hopping signals can be challenging to attempt to geolocate while still exhibiting cyclostationary properties. How does the *alpha*CAF method perform when the SOI or the SNOI is of the frequency hopping modulation type? Also, a logical extension of the BPSK signal work completed in this dissertation is a similar assessment of *quadrature phase shift keyed* (QPSK) signals and other variations such as OQPSK, MSK, GMSK, etc.

8.2.5 Least Squares Approach

An intuitive approach was used in deriving the *alpha*CAF method in Section 4.1. Then a ML approach in Section 4.2 was used and compared to the results in Section

4.1 to suggest that the *alpha*CAF method could produce unbiased estimates with sufficient data record lengths. Research could be conducted into using a *least squares* (LS) approach to derive a new correlation function that jointly estimates TDOA, FDOA and cyclic frequency. This new function could then be compared to the *alpha*CAF and a performance comparison made. In addition, other methods such as nontraditional weighted forms could be explored that may lead to better estimators.

8.2.6 Time–Varying Doppler

For a stationary emitter, measurement of TDOA using data collected from two spatially separated receivers will define a hyperbola on which the emitter must lie. The intersection of multiple hyperbola gives the source location estimate. When the source is moving, FDOA measurements must be used in addition to TDOA measurements to estimate the source position and velocity. Although several techniques are available in the literature for stationary emitter location, relatively little work is available for moving source tracking. Since an emitter's location is nonlinearly related to TDOA and FDOA measurements, determining an emitter's position and velocity from TDOA and FDOA measurements obtained at a single time instant is not a trivial task [9]. Research could be conducted into the effects of emitter movement on the TDOA and FDOA estimations made using the *alpha*CAF method. Since the receiver platforms can also experience non-uniform motion, methods for mitigating TDOA/FDOA estimation errors due to this motion could also be explored.

Bibliography

[1] G. C. Carter, "Coherence and Time Delay Estimation," *Proceedings of the IEEE*, vol. 75, pp. 236–255, February 1987.

[2] C. H. Knapp and G. C. Carter, "The Generalized Correlation Method for Estimation of Time Delay," *IEEE Trans. on Acoustics, Speech, and Signal Processing*, vol. ASSP-24, No. 4, August 1976.

[3] M. Azaria and D. Hertz, "Time-Delay Estimation by Generalized Cross-Correlation Methods," *IEEE Trans. on Acoustics, Speech, and Signal Processing*, vol. ASSP-32, No. 2, April 1984.

[4] S. S. Stein, "Algorithms for Ambiguity Function Processing," *IEEE Trans. on Acoustics, Speech, and Signal Processing*, vol. ASSP-29, No. 3, June 1981.

[5] Bassem R. Mahafza, *Simulations for Radar System Design*, second edition, published by Chapman and Hall/CRC, 2004.

[6] R. Tolimieri and S. Winograd, "Computing the Ambiguity Surface," *IEEE Trans. on Acoustics, Speech, and Signal Processing*, vol. ASSP-33, No. 4, October 1985.

[7] S. S. Stein, "Differential Delay/Doppler ML Estimation with Unkown Signals," *IEEE Trans. on Signal Processing*, vol. 41, No. 8, August 1993.

[8] R. J. Ulman, "Wideband TDOA/FDOA Processing Using Summation of Short-Time CAF's," *IEEE Trans. on Signal Processing*, vol. 47, No. 12, December 1999.

[9] W. A. Gardner and C. Chen, "Signal-Selective Time-Difference-of-Arrival Estimation for Passive Location of Man-Made Signal Sources in Highly Corruptive Environments, Part I: Theory and Method," *IEEE Trans. on Acoustics, Speech, and Signal Processing*, vol. 40, No. 5, May 1992.

[10] W. A. Gardner and C. Chen, "Signal-Selective Time-Difference-of-Arrival Estimation for Passive Location of Man-Made Signal Sources in Highly Corruptive Environments, Part II: Algorithms and Performance," *IEEE Trans. on Acoustics, Speech, and Signal Processing*, vol. 40, No. 5, May 1992.

[11] W. A. Gardner, "Exploitation of Spectral Redundancy in Cyclostationary Signals," *IEEE Signal Processing Magazine*, pp.14-36, April 1991.

[12] W. A. Gardner and C. Chen, "Interference-Tolerant Time-Difference-of-Arrival Estimation for Modulated Signals," *IEEE Trans. on Acoustics, Speech, and Signal Processing*, vol. 36, No. 9, September 1988.

[13] W. A. Gardner, *Statistical Spectral Analysis: A Nonprobabilistic Theory*, published by Prentice Hall, Englewood, New Jersey, 1988.

[14] D. A. Streight, "Maximum-Likelihood Estimators for the Time and Frequency Differences Of Arrival of Cyclostationary Digital Communications Signals," PhD. Dissertation, Naval Post Graduate School, 1999.

[15] K. C. Ho and W. Xu, "An Accurate Algebraic Solution for Moving Source Location Using TDOA and FDOA Measurements," *IEEE Trans. on Signal Processing*, vol. 52, No. 9, Sept. 2004.

[16] M. C. Glidewell, "Notes on Emitter Geolocation, Report," September, 2006.

[17] S. M. Kay, *Fundamentals Of Statistical Signal Processing: Estimation Theory*, published by Prentice Hall, Englewood, New Jersey, 1993.

[18] H. L. VanTrees, *Detection, Estimation, and Modulation Theory*, published by John Wiley and Sons, New York, 1968.

[19] T. K. Moon and W. C. Stirling, *Mathematical Methods and Algorithms for Signal Processing*, published by Prentice Hall, Englewood, New Jersey, 1999.

[20] D. H. Johnson and D. E. Dudgeon, *Array Signal Processing*, published by Prentice Hall, Upper Saddle River,

[21] J. G. Proakis, *Digital Communications*, published by McGraw-Hill, New York, NY,2001.

[22] R. G. Stansfield, "Statistical Theory of DF Fixing," *Journal of IEE, Part IIIA*, Vol. 94, PP. 762-770.

[23] J. Poirot, "Application of Linear Statistical Models to Radar Location Techniques," *IEEE Trans on AES*, vol. 10, pp. 830-834, 1974.

[24] R. O. Schmidt, "An algorithm for Two Receiver TDOA/FDOA Emitter Location," *IEEE Trans on AP*, vol. 34, pp. 134-139, 1986.

[25] C. J. Anker, "Airborne Direction Finding—The Theory of Navigation Errors," *IRE Trans on ANE*, vol. 5, No. 4, pp. 199-210, 1958.

[26] Y. T. Chan and J. J. Towers, "Geolocation of a Known Altitude Object From TDOA and FDOA Measurements," *IEEE Trans on AES*, vol. 28, pp. 1084-1090, 1992.

[27] W. H. Foy, "Position-location Solution by Taylor-series Estimations", *IEEE Trans on AES*, vol. 12, pp. 187-194, 1976.

[28] M. Gavish and A. J. Weiss, "Performance Analysis of Bearing-only Target Location Algorithms," *IEEE Trans on AES*, vol. 28, pp. 817-828, 1992.

[29] H. E. Daniels, *Journ.Roy.Statist.Soc.,Series B*, vol. 13, pp. 186-207, 1951.

[30] H. B. Lee, "A Novel Procedure for Assessing the Accuracy of Hyperbolic Multilateration Systems," *IEEE Trans on AES*, vol. 11, pp. 2-15, 1975.

[31] M. Wax, "Optimum Localization of Multiple Sources by Passive Arrays," *IEEE Trans on AES*, vol. 19, pp. 658-662, 1983.

[32] P. C. Chesnut, "Emitter Location Accuracy Using TDOA and Differential Doppler," *IEEE Trans on AES*, vol. 18, pp. 214-218, 1982.

[33] G. Clark, "Simplified Determination of The Ellipse of Uncertainty," *Navigation Journal*, vol. 21, No. 4, pp. 343-350, 1974-1975.

APPENDICES

Appendix A – RELATIONSHIP BETWEEN FDOA AND TDOA

A simple relationship exists between the rate of change of the *time-difference-of-arrival*, which I will call TDOA-dot, or $\dot{TDOA}$, and the *frequency-difference-of-arrival*, or FDOA. Consider the two-dimensional cartesian coordinate system in Figure A.1, where two receivers are initially located at (x_1, y_1) and (x_2, y_2) and a target emitter is located at (x_T, y_T).

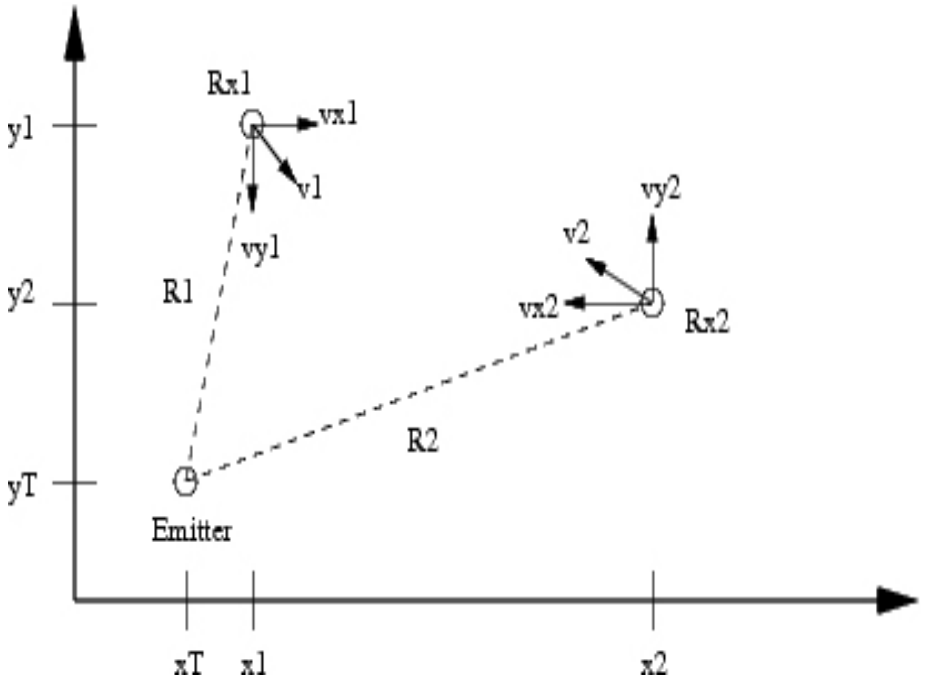

Figure A.1: Collection geometry diagram.

The two receivers are moving with a velocity vector $\mathbf{v}_1$ and $\mathbf{v}_2$ respectively. Their initial positions result in the ranges R_1 and R_2 to the target emitter. So, the positions at time

t will be

$$\begin{aligned} x_1(t) &= x_1(0) + v_{1x}t \quad \text{and} \quad y_1(t) = y_1(0) + v_{1y}t \\ x_2(t) &= x_2(0) + v_{2x}t \quad \text{and} \quad y_2(t) = y_2(0) + v_{2x}t \ . \end{aligned} \tag{A.1}$$

The ranges at time t will be

$$\begin{aligned} R_1^2(t) &= (x_t - x_1(t))^2 + (y_t - y_1(t))^2 \\ R_2^2(t) &= (x_t - x_2(t))^2 + (y_t - y_2(t))^2 \ . \end{aligned} \tag{A.2}$$

The TDOA of the emitter signal at the two receivers is

$$TDOA = \frac{R1 - R2}{c} \tag{A.3}$$

where c is the speed of light. The rate of change of TDOA, or $\dot{TDOA}$, is the derivative of (A.3),

$$\dot{TDOA} = \frac{d(TDOA)}{dt} = \frac{d}{dt}\left(\frac{R1 - R2}{c}\right) \tag{A.4}$$

which becomes

$$\dot{TDOA} = \frac{1}{c}\left[\frac{dR_1}{dt} - \frac{dR_2}{dt}\right] \ . \tag{A.5}$$

Using (A.1) and (A.2), (A.5) can be written as

$$\dot{TDOA} = \frac{1}{c}\left[\frac{(x_T - x_1)v_{1x} + (y_T - y_1)v_{1y}}{R_1} - \frac{(x_T - x_2)v_{2x} + (y_T - y_2)v_{2y}}{R_2}\right] \ . \tag{A.6}$$

If the emitter transmits at frequency f, then due to relative motion between the receivers

and the emitter, physics tells us that the signal frequencies at receivers 1 and 2 are

$$\begin{aligned} f1 &= f\,(1 + v_{1r}/c) \\ f2 &= f\,(1 + v_{2r}/c) \end{aligned} \tag{A.7}$$

where v_{1r} and v_{2r} are the radial velocity magnitudes of the receivers with respect to the emitter. Note that

$$\begin{aligned} v_{1r} &= \mathbf{v}_1 \cdot \frac{\mathbf{R}_1}{|\mathbf{R}_1|} \\ v_{2r} &= \mathbf{v}_2 \cdot \frac{\mathbf{R}_2}{|\mathbf{R}_2|}\ . \end{aligned} \tag{A.8}$$

Some algebra will show that

$$\begin{aligned} v_{1r} &= \left[\frac{(x_T - x_1(t))v_{1x} + (y_T - y_1(t))v_{1y}}{|\mathbf{R}_1|}\right] \\ v_{2r} &= \left[\frac{(x_T - x_2(t))v_{2x} + (y_T - y_2(t))v_{2y}}{|\mathbf{R}_2|}\right]\ . \end{aligned} \tag{A.9}$$

Since FDOA is defined as

$$FDOA = f_1 - f_2\ , \tag{A.10}$$

then using (A.7) and (A.9) it is possible to arrive at

$$FDOA = \frac{f}{c}\,(v_{1r} - v_{2r}) = (f)(\dot{TDOA})\ , \tag{A.11}$$

which is the relationship between FDOA and TDOA. It is clear from (A.11) that a changing TDOA gives rise to a FDOA.

Appendix B – THE SIMULATED BPSK SIGNAL

A BPSK signal can be modeled by [9]

$$s(t) = a(t)cos(2\pi f_c t + \phi_0) \tag{B.1}$$

where

$$a(t) = \sum_{n=-\infty}^{\infty} a_n q(t - t_0 - nT_0) \tag{B.2}$$

in which a_n is a binary (± 1) sequence and $q(t)$ is a finite-energy keying envelope given by

$$q(t) \triangleq \left\{ \begin{array}{lll} 1 & , & |t| \leq T_0/2 \\ 0 & , & otherwise \end{array} \right\} \tag{B.3}$$

where T_0 is the keying envelop width.

It can be shown [13] that the spectral correlation function for $s(t)$ is given by

$$\begin{array}{c} S_s^\alpha(f) = \frac{1}{4T_0}\left[Q(f + f_0 + \alpha/2)Q^*(f + f_0 - \alpha/2)\right]\exp(-j2\pi\alpha t) \\ +\frac{1}{4T_0}\left[Q(f - f_0 + \alpha/2)Q^*(f - f_0 - \alpha/2)\right]\exp(-j2\pi\alpha t) \end{array} \tag{B.4}$$

for $\alpha = n/T_0$ and $Q(f)$ being the Fourier transform of the keying envelope $q(t)$

$$Q(f) = \int_{-\infty}^{\infty} q(t)\exp(-j2\pi f t)\ . \tag{B.5}$$

Likewise, for $\alpha = \pm 2f_c + n/T_0$

$$\begin{aligned} S_s^{\alpha}(f) = \tfrac{1}{4T_0}\left[Q(f + f_0 + \alpha/2)Q^*(f + f_0 - \alpha/2)\exp(-j2\pi(\alpha + 2f_c)t)\right] \\ + \tfrac{1}{4T_0}\left[Q(f - f_0 + \alpha/2)Q^*(f - f_0 - \alpha/2)\exp(-j2\pi(\alpha - 2f_c)t)\right] \ . \end{aligned} \tag{B.6}$$

The cyclic correlation function can be found by taking the inverse Fourier transform of (B.3) and (B.5). Note that all of the BPSK signals used in this dissertation for algorithm examples were generated using a rectangular keying envelope.

Appendix C – LIST OF ACRONYMS

Name	**Definition**
AlphaCAF	alpha cross ambiguity function
AM	Amplitude modulation
AOA	Angle-of-arrival
AWGN	Additive white Gaussian noise
BPSK	Binary phase shift keyed
CAF	Cross ambiguity function
CCI	Co-channel interference
CDMA	Code division multiple access
CRLB	Cramer Rao lower bound
DF	Direction Finding
DOA	Direction-of-arrival
FDOA	Frequency-difference-of-arrival
FFT	Fast Fourier transform
FM	Frequency modulation
GCC	Generalized cross correlation
GMSK	Gaussian minimum shift keyed
IF	Intermediate frequency
IFFT	Inverse fast Fourier transform
MAI	Multiple access interference

Name	Definition
MCT	Monte Carlo testing
ML	Maximum Likelihood
MSK	Minimum shift keyed
OQPSK	Offset quadrature phase shift keyed
PHAT	The phase transform
PSD	Power spectral density
QPSK	Quadrature phase shift keyed
RF	Radio frequency
RMSE	Root mean squared error
ROTH	The Roth processor
SCD	Spectral correlation density
SCOT	The smoothed coherence transform
SIR	Signal-to-interference ratio
SNOI	Signal-not-of-interest
SNR	Signal-to-noise ratio
SOI	Signal-of-interest
SPECCOA	Spectral coherence alignment method
SPECCOR	Spectral correlation ration method
TDOA	Time-difference-of-arrival
TOA	Time-of-arrival

APPENDIX B

SHARPENING TECHNIQUES FOR ENHANCED
TIME - FREQUENCY ANALYSIS OF CHARACTERIZATION
OF LAND MINES BY RADAR

Masters Candidate: Matthew Fleming
Advisor: S. Lawrence Marple, Jr.

School of Electrical Engineering and Computer Science
Oregon State University
Corvallis, OR

Research Poster

AFOSR Award FA9550-08-1-0412

July 2009

Sharpening Techniques For Enhanced Time-Frequency Analysis Characterization Of Landmines By Radar

School of EECS, Oregon State University, Corvallis, Oregon, 97333, USA

Matthew Fleming
fleminma@engr.oregonstate.edu

S. Lawrence Marple, Jr.
marple@eecs.oregonstate.edu

Background

UWB radar ("impulse" radar) and GPR capture a transient temporal signal response from buried landmines. Classical Fourier-based techniques (e.g. STFT) limit the time-frequency analysis (TFA) resolution of details needed to detect and to characterize (distinguish) features among landmine signatures. Alternatives such as Wigner-Ville (WVF) sharpen the T-F signature, but at the expense of numerous cross-term artifacts that obscure details.

Objective

Without cross-term artifacts, use high-resolution 1-D, frequency-only techniques (e.g. autoregressive (AR), minimum variance (MV)) to sharpen along just the frequency axis of the TFA gram, or special variants of high-resolution 2-D spectral analysis (e.g. AR, MV) to sharpen simultaneously along both time and frequency axis of TFA gram.

Approach

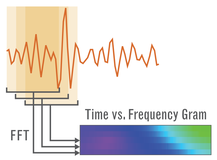

Traditional analysis methods use quasi-stationary windows to produce time-frequency grams line-by-line by using simple 1-D techniques, such as the FFT or WVF.

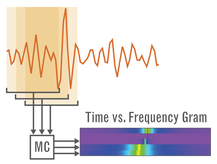

More advanced methods attempt to model signals (e.g. Y-W AR, or mod. cov.), but these are also line-by-line cascades of 1-D techniques.

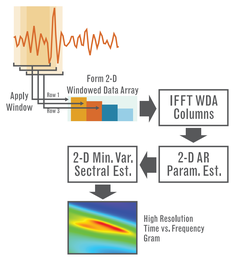

New 2-D minimum variance method takes windowed data and pre-transforms it into an inverse frequency vs. center time 2-D structure. This 2-D dataset is subsequently processed by 2-D versions of the above modeling methods with the end result a time-frequency gram without undesired artifacts (e.g. WVF).

Results

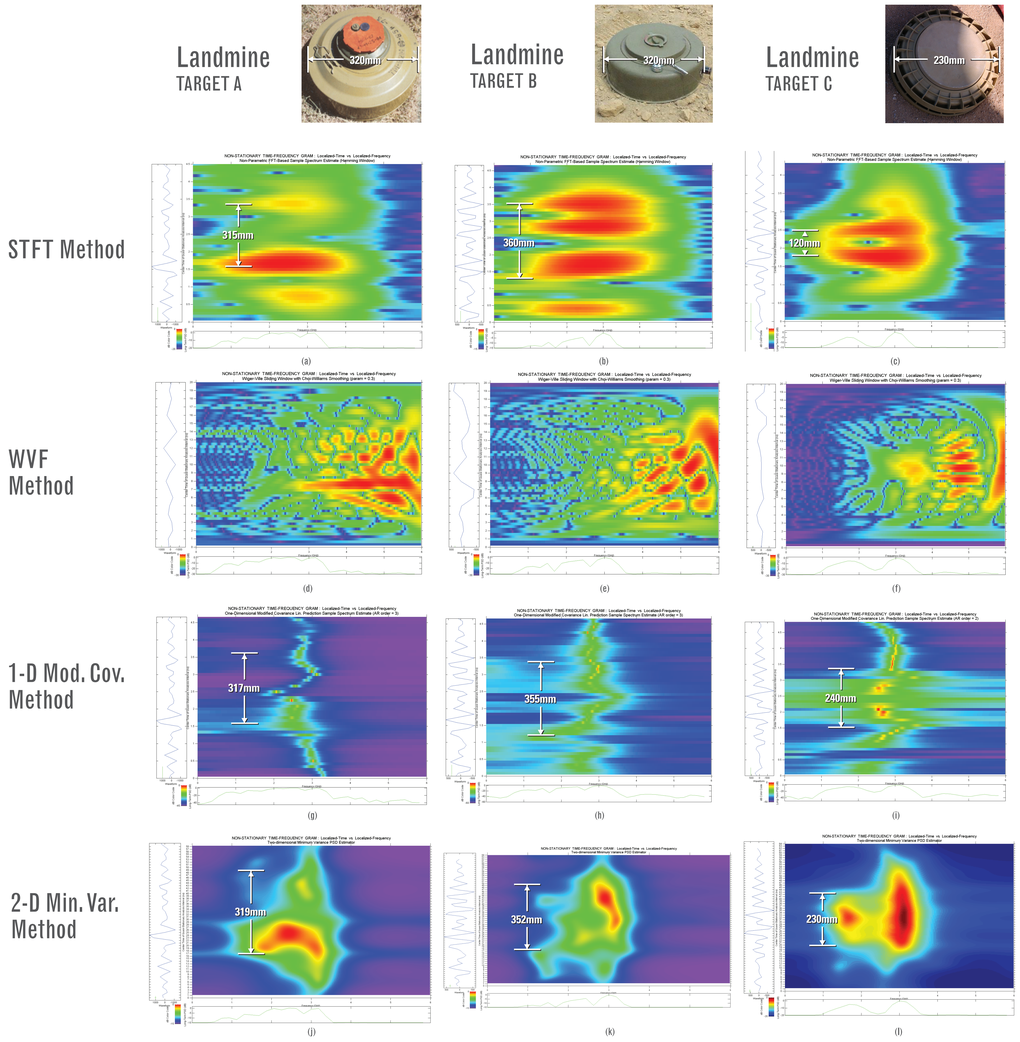

Three different mine targets were used. Target A was a TM62M metal mine, Target B was a TM62P3 plastic mine, and Target C was a VS-2.2 plastic mine. All mines were surface mines. Returns from this type of physical arrangement typically have two impulses returned from the front and rear edges of the mine, which can be used to determine its physical dimension.

The STFT is useful for detecting these peaks, but does not provide additional detail that may be present in the returned signal. This is of limited use and only provides a rough estimate of the object's physical dimensions.

The WVF method provides higher resolution in both time and frequency, but significant artifacts are introduced which obscure potential low energy signals.

Results continued

The 1-D modified covariance method provides substantial detail in frequency, while preserving broadband impulse return information. This is useful for determining resonance (a constant-frequency return) and creeping waves (returns that are sinusoidal in frequency as a function of time). One or both features may be observed in the plots to the left (plots (g)-(i)).

These algorithms build their time-frequency grams by taking windowed data and applying one-dimensional transforms to each windowed set. The new 2-D minimum variance method seeks to pre-transform the data into a two-dimensional structure thereby avoiding the trade-off between high resolution in time-only versus high resolution in frequency-only, obtaining high resolution in both.

Plots (j)-(l) show higher detail in frequency when compared to the STFT method, and higher detail in time when compared to the 1-D modified covariance method. This allows for better feature extraction from the returns from the target, thereby providing more accurate insight into the target's dimension.

Plot parameters: (a) Analysis interval of 10 samples; (b) Analysis interval of 8 samples, AR order 3; (c) Analysis interval of 14 samples, AR order 7x7; (d)-(f) Analysis interval of 4 samples; (g) Analysis interval of 8 samples; (h) Analysis interval of 8 samples, AR order 3; (i) Analysis interval of 16 samples, AR order 8x8; (j) Analysis interval of 12 samples; (k) Analysis interval of 6 samples, AR order 2; (l) Analysis interval of 16 samples, AR order 8x8.

All plots used a step increment between intervals of one sample, and 512 point FFTs where appropriate. The STFT, 1-D Mod. Cov, and 2-D Min. Var. methods used Hamming windows to suppress side lobes.

Conclusions

Traditional methods of time-frequency analysis, such as the STFT, are of limited use in modern signal processing. It is desirable to have higher resolution in both time and frequency for feature extraction and signature analysis, but initial attempts (e.g. WVF) introduce undesirable artifacts that can obscure minute, but important, details. We propose new methods to provide higher frequency resolution, or higher time and frequency resolution simultaneously, all without cross-term artifacts characteristic of the WVF method. These new methods provide not only better information about mine physical dimension, but also provide for more sophisticated analysis to determine other parameters about mine type, construction, and physical state from signature phenomena, such as resonant frequencies and creeping waves, which can allow for the use of 2-D image classifiers to distinguish mines based on TFA shape & features.